# Low-cost and versatile fabrication of silicon-compatible photonic integrated circuits for active devices and sensors

# Low-cost and versatile fabrication of silicon-compatible photonic integrated circuits for active devices and sensors

By Dawson B. Bonneville, B.Eng.

A thesis submitted to the School of Graduate Studies for partial fulfillment of the requirements for Degree Ph.D.

McMaster University

Ph.D. (2022)

Hamilton, Ontario (Department of Engineering Physics)

TITLE: Low-cost and versatile fabrication of silicon-compatible photonic integrated circuits for active devices and sensors

AUTHOR: Dawson B. Bonneville, B.Eng. (McMaster University)

SUPERVISOR: Dr. Jonathan D. B. Bradley

NUMBER OF PAGES: xxi, 179

# Abstract

The variety of photonic materials required to address the needs of the expanding market and application space for photonic integrated circuits (PICs) is driving the need for widely applicable, reliable, versatile and scalable fabrication techniques. Working with materials that are compatible with Silicon (Si) allows for integration into foundry processing and large-scale integration, which is crucial for economic scaling. However, because Si is a poor emitter of light, this poses a challenge for the implementation of specific components such as monolithic optical amplifiers and lasers, which are needed for the next generation of telecommunication devices and sensors. For this reason, a variety of materials are required to address the growing demand for new functionalities in PICs, including on-chip passive components and optically active amplifiers and lasers. These materials include traditional silicon-compatible materials such as silicon nitride ($Si_3N_4$), and less mature materials such as rare-earth doped oxides including aluminium oxide ($Al_2O_3$) and tellurium dioxide ($TeO_2$). To process the different materials and fabricate waveguides for a variety of platforms, circuit architectures and applications, it is advantageous to develop robust, versatile, and economic solutions to prepare for a changing and growing industry. This thesis presents a variety of fabrication techniques and protocols to achieve high optical quality materials and waveguides through thin film deposition and patterning, and demonstrates the realization of an optical amplifier and a protein sensor in an erbium-ytterbium co-doped $Al_2O_3$ ($Al_2O_3$:$Er^{3+}$:$Yb^{3+}$) waveguide and a poly(methyl methacrylate) (PMMA)/$TeO_2$-Si distributed Bragg reflector cavity, respectively. The objectives of this thesis are to demonstrate low-loss silicon nitride films using plasma-enhanced chemical vapour deposition (PECVD), to develop a controllable process for

waveguide device fabrication using UV writing, to demonstrate optical gain in $Er^{3+}$:$Yb^{3+}$:$Al_2O_3$ waveguide amplifiers fabricated with wet-etching, and to demonstrate biological sensing on Si chips which are capable of rare-earth integration. Chapter 1 introduces background literature on photonic integrated circuits and provides an overview and comparison of various film deposition and patterning techniques, including those explored in this work. Chapter 2 includes details on the background and theory of waveguides, provides a guide and process to designing waveguides for different mode properties, materials and devices, and introduces the relevant theory for optical amplifiers and photonic biological sensors. Chapter 3 demonstrates a recipe and process for the deposition of silicon nitride films using PECVD at 140 °C and 1.5 mTorr, which shows partially hydrogenated, and non-stoichiometric $SiO_xN_y$:$H_z$ films with optical propagation losses as low as 1.3, 0.3 and 1.5 ± 0.1 dB/cm at 638, 980 and 1550 nm respectively, without heat treatment. Chapter 4 presents UV laser writing in negative photoresist as a procedure for prototyping waveguides in $Si_3N_4$. Scanning electron microscopy (SEM) was used to analyze feature and gap control, and dry plasma etching was used to realize optical devices such as a directional coupler, Sagnac interferometer, and ring resonator, which demonstrate 50/50 coupling at 1510 nm, 20 dB transmission drop at 1580 nm, and a *Q* factor of ~13,000 at 1576 nm, respectively. Chapter 5 reports on the deposition and patterning of $Al_2O_3$:$Er^{3+}$:$Yb^{3+}$ waveguides using reactive co-sputtering and wet chemical etching, with internal net gain of 4.3 ± 0.9 dB at 1533 nm for a 3.0 cm long waveguide when pumped at 970 nm. Chapter 6 presents a hybrid Si-$TeO_2$ Bragg waveguide sensing platform with plasma functionalized PMMA for biological attachment. Thermal, water and protein

sensing were performed leading to a sensitivity of 0.13 nm/°C, limit of detection of 5.9 $\times 10^{-3}$ RIU, and a 1.6 nm shift after incubation with 2 µg/mL BSA diluted in PBS with subsequent recovery of the sensor for reuse after stripping. Chapter 7 summarizes the thesis and provides pathways towards optimizing current and future work.

## Acknowledgements

I wish to begin by thanking my academic supervisor Dr. Jonathan D. B. Bradley. As an eager undergraduate with sub-par grades, I was granted the opportunity to pursue research in the Bradley group from its start at McMaster. Throughout a total of 6–7 years of supervision I have been offered limitless support, guidance, and wisdom which I feel will serve my career in research greatly for the future. The feeling of intellectual creativity, trust, and balance of work-life during my research with Jon has allowed me to have a fulfilling and enriching start to my career, and for this I am grateful. I also wish to extend a thanks to my committee members Dr. Ray LaPierre and Dr. Andy Knights who provided useful council, critique, and enthusiasm for my results during my doctorate.

To my countless colleagues, lab mates, and collaborators along the way, your teamwork and extended aid made my research educational, exciting, and enjoyable. From my start to finish in the Bradley group, people in particular, Jeremy W. Miller and Henry C. Frankis provided invaluable guidance and assistance which made this work possible. To the Center for Emerging Device Technology (CEDT) staff, Doris V. Stevanovic, and Shahram Tavakoli, your expertise and training, as well as selfless dedication to the labs has enabled the crucial fabrication to take place which is at the core of this thesis. I'd also like to thank Dr. Andy Knights again for supervising an enjoyable 4 years of teaching assistance which allowed me to explore my passion for instructing.

To my close friends at McMaster who lived through undergraduate with me, in particular Michael "go follow your dreams" Kiriakou, I would not have made it to graduate school without you. I'd like to thank my friends and family back in Toronto, as I was lucky to always have a second home that gave me an escape from campus life and a needed break from the academic head space. Especially my *brothers* Dylan W. Bonneville, and

Cameron E. Kirk who facilitated countless couch getaways, concerts and needed late nights.

To my parents who support me no matter what I do, your love and encouragement is appreciated infinitely. I have had the privilege of being able to focus on my studies, during my studies, and for this I am forever grateful. I'd like to acknowledge two sayings I bring from my dad which have served me well throughout my time at McMaster – "the squeaky wheel gets the grease", and ironically, "never let school get in the way of education".

I wish to finally acknowledge my wife Destanee M. Bonneville, who provided me with sanctuary for writing this thesis and completing my studies with unwavering support and love. Lastly, I thank our cat, Dale Cooper Bonneville, for being an insightful late night work partner.

*"Take it easy dude, but take it!"*

# Table of Contents

# List of Figures

# List of Tables

## List of Acronyms

| | |
|---|---|
| AFM | Atomic force microscopy |
| ALD | Atomic layer deposition |
| ASE | Amplified spontaneous emission |
| BARC | Back anti-reflection coating |
| CEDT | Center for emerging device technologies |
| CMOS | Complementary metal-oxide-semiconductor |
| CVD | Chemical vapour deposition |
| DBR | Distributed Bragg resonator |
| DFB | Distributed feedback |
| DI | Deionized |
| DUV | Deep ultraviolet |
| DVD | Digital video disc |
| EBL | Electron beam lithography |
| ECR | Electron cyclotron resonance |
| EDFA | Erbium doped fiber amplifier |
| EDWA | Erbium doped waveguide amplifier |
| EMT | Effective medium theory |
| ERDA | Elastic recoil detection analysis |
| FDTD | Finite difference time domain |
| FEM | Finite element method |
| FSR | Free spectral range |
| FTIR | Fourier transform infrared spectroscopy |
| FWHM | Full width at half maximum |
| HDP | High density plasma |
| HV | High vacuum |
| ICP | Inductively coupled plasma |
| LDW | Laser direct write |
| LER | Line edge roughness |
| LIDAR | Light detection and ranging |
| LPCVD | Low pressure chemical vapour deposition |
| MEMS | Micro electromechanical systems |

| | |
|---|---|
| MFC | Mass flow controller |
| MIR | Mid infrared |
| MP | Multi-piece |
| MPW | Multi-project wafer |
| NIR | Near infrared |
| OSA | Optical spectrum analyzer |
| PECVD | Plasma enhanced chemical vapour deposition |
| PIC | Photonic integrated circuit |
| PM | Polarization maintaining |
| PVD | Physical vapour deposition |
| RBS | Rutherford backscattering |
| RE | Rare earth |
| REDWA | Rare earth doped waveguide amplifier |
| REDWL | Rare earth doped waveguide laser |
| RF | Radiofrequency |
| RIE | Reactive ion etching |
| RIU | Refractive index units |
| RMS | Root mean squared |
| SE | Signal enhancement |
| SEM | Scanning electron microscopy |
| SOA | Semiconductor optical amplifier |
| SOI | Silicon-on-insulator |
| SW | Sidewall |
| SWG | Subwavelength |
| TE | Transverse electric |
| TEC | Thermo-electric cooler |
| TEM | Transmission electron microscopy |
| TM | Transverse magnetic |
| TPA | Two-photon absorption |
| UV | Ultraviolet |
| VASE | Variable angle spectroscopic ellipsometry |
| WDM | Wavelength division multiplexer |
| WG | Waveguide |

# Declaration of Authorship

I, Dawson Bonneville, declare that this thesis, “Low-cost and versatile fabrication of silicon-compatible photonic integrated circuits for active devices and sensors” was written by and presents research work lead by myself.

Contributions made by others to this work are as listed:

Chapter 2

- Henry Frankis aided in the plotting of waveguide modes using Matlab.

Chapter 3

- Caitlyn Smith aided in the deposition and annealing and performed the optical loss measurements for $SiO_xN_yH_z$ films.
- Jeremy Miller performed AFM measurements and aided in RBS and ERD data fitting.

Chapter 4

- Arthur Méndez-Rosales aided in the UV exposure optimization and SEM measurements.
- Henry Frankis developed the plasma etching recipe used for the $Si_3N_4$ waveguides.

Chapter 5

- Henry Frankis and Renjie Wang developed the sputtering recipe for un-doped and doped $Al_2O_3$ films. This included prism coupling measurements performed by both in order to determine the film loss and concentration of $Er^{3+}$ and $Yb^{3+}$ ions.

- Henry Frankis also was responsible for the creation of the optical setup used to characterize the internal gain for doped waveguides.

Chapter 6

- Si waveguides were received from a MPW run as part of the SiEPIC program.
- Henry Frankis developed the $TeO_2$ sputtering recipe, and Khadijeh Miarabbas Kiani performed the depositions of the $TeO_2$ films for the study.
- Mitchell Albert performed the hydrophilicity measurements and aided on protein handling and sensing protocols.
- Ramis Arbi performed PMMA functionalization using $O_2$ plasma.

# Chapter 1

## Introduction

This chapter provides an introduction of fiber optics, and the progression in research and industry towards integrated photonics with thin films. After introducing photonic integrated circuits and their need across various applications, waveguide materials are introduced, followed by a comparison of different film deposition and waveguide patterning techniques. The need for versatile fabrication methods is then discussed with a specific focus on new functionalities required in integrated photonics, such as optical amplifiers and lasers, as well as biological sensors.

### 1.1 Photonic Integrated Circuits

Applying light as a solution to modern problems has become a staple of the information age. The monochromatic, directional, and intense light emission properties of the laser have been applied to a plethora of industries, including healthcare, imaging, manufacturing, telecommunications and many more. Global telecommunication signals rely on fiber optic cables, which stretch across the oceans and transmit laser light from one continent to another using total internal reflection. Since its inception, the field of fiber optics has reshaped the world we live in, allowing light-speed communications with information capacities which have enabled the internet. Alongside the invention of the laser, these advances have together enabled the infrastructure which has defined modern society, including the recent data center boom for streaming services and cloud computing as well as countless advances in the fields of medicine and sensing [1–3]. As technology becomes more compact, and performance continues to scale inversely with the size of devices, the necessity to confine and control laser light on small scales will

become ever more apparent. Building on the transition from free space optics to fiber which is continuing to evolve, the current scaling down in size in photonics research is from fiber to microchip. To do so, layered dielectrics are used for optical confinement, including a wide variety of thin film planar media which can provide comparable or additional functionalities to those fibers provide but on a smaller scale. These photonic circuits allow for optical transmission from fibers to on-chip processing devices without the need for electrical conversion, which currently bottlenecks the available bandwidth in data centers [1,4].

Optical circuity, or a PIC, requires the patterning of optically compatible materials on a planar substrate. Depending on the materials used, this can allow for electrical manipulation of optical signals via carrier modulation for switching [5–10], optical-electrical conversion of signals for on-chip detectors [11–15], and electrical injection for light generation in semiconductor lasers [16–19], among other active functionalities. By routing waveguides on the chip passive devices can also be made which give functionality to the circuit including interferometers [20], resonators for filters [21], or arrayed waveguide gratings for beam steering [22,23], for example. Compared to fibers, PICs can have many functions which are packed onto a single chip instead of in separate components. Much of their advantage comes from the parallel definition of structures to allow for complex circuits, and the ability to include multiple materials and manipulate the light from the surface of the device. Different materials such as Si and $Si_3N_4$ have attracted interest for research over many years as a growing variety of platforms for PICs are considered for various functionalities leading to applications in countless fields. The investigation of these various materials and their processing methods for PICs are active

research areas which require advances to make the devices mass producible. In the aim of achieving a commercial reality for the field, it is advantageous that the photonic materials integration can all be carried out at the scale and volume of traditional silicon micro and nanoelectronics using existing industrial facilities with complementary metal oxide semiconductor (CMOS) pilot lines.

## 1.2 Waveguide Materials and Fabrication Methods

### 1.2.1 Silicon-based Photonic Platforms

To guide and manipulate optical signals in PICs, materials are required which provide transparency in the NIR telecommunication bands or relevant visible optical sensing windows, can be structured into functional devices, and have the capability to be mass produced. Low waveguide propagation losses are also necessary, which depend on high-quality thin film materials and structuring methods that enable smooth surfaces and sidewalls for devices. Except for visible transmission, silicon satisfies all of these requirements when applied to photonics, which conveniently compliments its electronic capabilities [24]. Silicon photonics leverages the fabrication techniques and equipment from the microelectronics industry to enable low loss high refractive index contrast waveguides and compact devices which are capable of electro-optic detection and carrier depletion or injection for high-speed modulation [5]. Silicon also has heritage and proven fabrication methods from an economics perspective has made it the substrate of choice for many photonics applications [25]. Therefore, it is advantageous when other prospective materials can be integrated into existing silicon photonics processes in a compatible manner. Further details on silicon photonics platforms can be found in section 2.2.1.1. More recently, silicon nitride ($Si_3N_4$) has been demonstrated as a waveguide platform which is capable of ultra-low losses (<0.001 dB/cm) [26–29] and has the added

benefit of transmission in the visible domain. Its ability to be readily integrated with Si and the CMOS pilot line has enabled it to become a rapidly advancing waveguide platform [30], and as such it is the subject of section 2.2.1.2. Research and development on these multiple waveguide platforms, in conjunction with many others not mentioned here including silicon carbide [31], germanium [32], polymers [33,34], and lithium niobate [35], is opening many doors in telecommunications [36,37], LIDAR [23,38], biological sensing [39], quantum photonics [40,41], and many other applications and industries. This thesis aims to develop novel silicon-based photonic materials and waveguide structures, which alongside their processing steps can be used to realize passive waveguide devices as well as optically active devices including waveguide amplifiers and biological sensors.

### 1.2.1 Thin Film Deposition

Guiding optical signals in a thin film medium is achieved by careful design of the refractive index profile. Much like optical fibers confine light to a cylindrical glass core surrounded by a lower refractive index glass cladding, integrated photonic waveguides confine light to planar core layers stacked between and patterned within cladding materials to create pathways for light in either crystals, dielectrics, or polymers. To fabricate these materials different deposition methods are available, which have various advantages and disadvantages. Table 1.1 represents a small selection of fabrication techniques which are used to deposit the waveguide materials investigated in this thesis.

**Table 1.1.** Comparison of selected thin film deposition techniques used to fabricate planar optical waveguides. Asterisks indicate techniques used in this thesis.

| Deposition technique [Ref] | Material platforms | Precursor requirements | Deposition temperature (°C) | Advantages | Disadvantages |
|---|---|---|---|---|---|
| PECVD* [42] | Si, $Si_3N_4$, $SiO_2$, $SiO_xN_y:H_z$ | Plasma dissociated gas | < 400 | Low temperature | Hydrogen incorporation |
| LPCVD [43] | | Thermal dissociated gas | > 700 | Stoichiometry control, low loss | High temperature, high stress |
| Reactive sputtering* [44,45] | $Al_2O_3$, $TeO_2$, $Al_2O_3$:RE, $TeO_2$:RE | Solid targets | > 30 | Versatile conditions | Variation in stoichiometry |
| ALD [46,47] | | Reactive volatile compounds | > 300 | Composition control | Slow deposition rate |

In chemical vapour deposition (CVD), the chemical constituents of the films in gas phase are introduced into a vacuum chamber, alongside inert gases with appropriate pressure and applied energy, which causes thin-film growth on a substrate within the chamber. The chemicals react on the surface of the substrate resulting in deposition of a thin film of a composition which is dependent on the reactive species. PECVD utilizes additional energy inside of a plasma to allow for greater dissociation of gas species and increased kinetics during deposition [42] at pressures as low as 1 mTorr. In PECVD significant effort is still required to reduce the hydrogen incorporation in films, which can lead to deleterious effects like increased loss from O-H or Si-H bond absorption. LPCVD in comparison operates at higher temperatures (~800 °C) and relies on heat to supply the reaction kinetics and dissociation [43] which makes it less compatible with thermally sensitive materials such as metals and polymers but provides better stoichiometry control.

Physical vapour deposition (PVD) utilizes plasma and ambient gas to strip atoms of a particular species from a solid material and causes them to be preferentially physiosorbed onto the surface of a substrate. An example of this is reactive magnetron sputtering, which

allows for flexible deposition conditions by using high purity solid targets consisting of a wide variety of elements and compounds and ambient gas to react with the solid species inside the chamber and on the surface of the film. Reactive magnetron sputtering is also attractive due to its ability to deposit a versatile selection of materials with flexible substrate choices [44]. It can be used to deposit amorphous oxides [45] doped with rare earths on substrates over a wide range of temperatures depending on the thin film material and required properties. ALD has fine control over the morphology of the thin film via alternating use of gas phase precursors or reactants which deposits atoms layer by layer to produce uniform high-quality films [46,47]. It requires precursors which exist in reactive volatile forms and has relatively low deposition rates. A detailed study on various deposition methods, as well as the demonstration of a hybrid sputtering-PECVD chamber which shows that multiple techniques can be combined and specifically allows for rare earth doping in silicon-based thin films, is included in [48].

### 1.2.2 Waveguide Patterning

Thin films need to be patterned in order to confine electromagnetic waves into smaller areas in order for them to be guided on the chip and produce increased functionality. To do so, the film can be structured into channels with dimensions on the order of the wavelength of the electromagnetic radiation (~1 μm), which support the field and confine it to set optical pathways on the chip, much like a subway in a tunnel. Structuring a waveguide in a thin film first requires an exposure step, where a pattern is typically transferred into a polymer resist material, much like photography with film. Light from a laser or electrons from a beam impinge on photo and electro-sensitive molecules, which after development and chemical reaction reveals an exposed layer or material. This exposed layer can represent the waveguiding thin film of interest, which with proper

chemical consideration and selectivity to the polymer masking layer can now be etched away in decided areas. This process is referred to as lithography and is the dominant technique for micro and nanofabrication and is used for the patterning of waveguides in thin films. Figure 1.1 demonstrates different fabrication process flows for the realization of waveguides in thin films, which includes a variety of techniques for exposure and etching of structures.

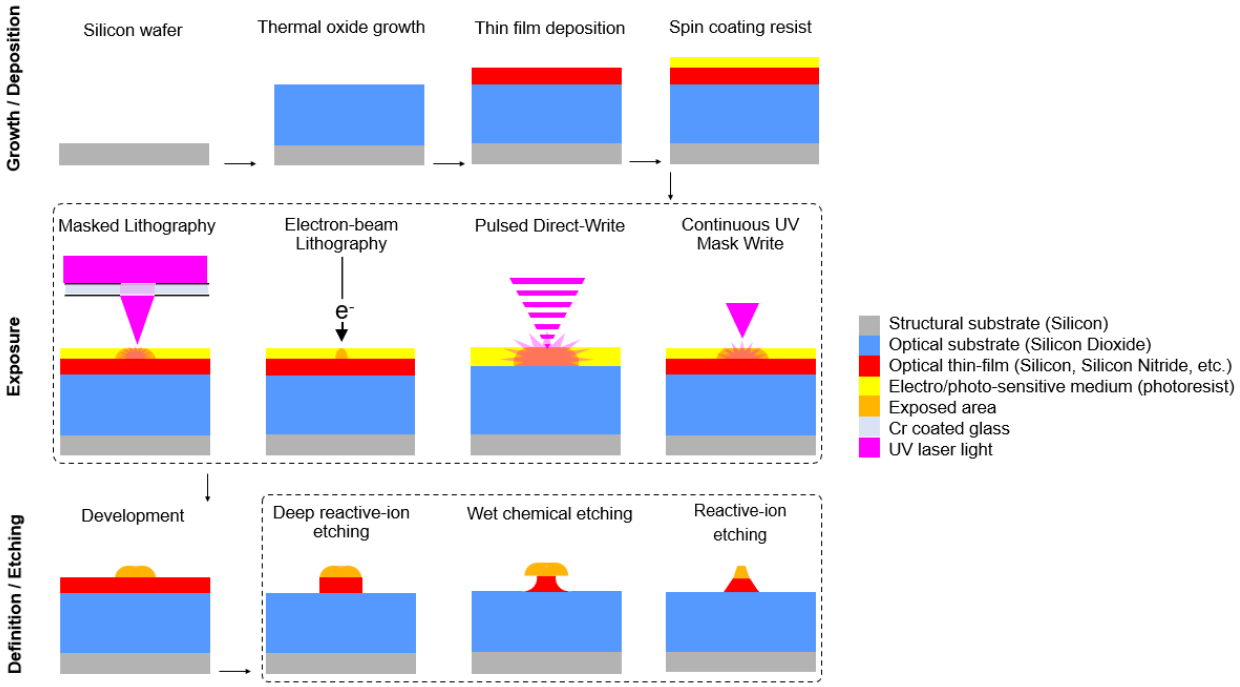


**Figure 1.1.** Fabrication procedures for waveguide patterning with various examples of exposure and etching techniques.

These methods each have their advantages and drawbacks which are contrasted in Table 1.2. For batch exposures of multiple devices on full wafers, flooding light through a mask with shaded areas can be used either to weaken (positive process) or strengthen (negative process) the photoresist. This is referred to as binary photomasking, where chromium layers and patterns are pre-defined on a quartz mask plate in order to transfer

a design to a chip, much like shadow puppets. Contact and immersion lithography are industrial standards which are constantly being improved upon for high volume fabrication of photonic devices but are optimized only for specific materials. Nanoimprint lithography requires the use of a PDMS mold and roller assembly, which is more attractive for large area 2D patterns but can still be used for grating fabrication in polymers. Without the mask, the exposure technique can be controlled by using a focused laser beam and a scanning stage, which with fine motor control can trace out desired images or patterns. Maskless lithography allows for prototyping of designs with rapid turnaround and adaptability of features and exposed pattern details. This is particularly useful when also developing thin film materials as properties such as thickness or index may be varying significantly from design to design, which requires different waveguide widths and device dimensions while prototyping devices. Depending on the material and exposure source, this can take place as either electron beam lithography, pulsed UV writing into materials which can undergo a permanent change in the local speed of light, or refractive index or continuous UV writing in photoresist. E-beam lithography suffers from facility and user fee cost drawbacks, but demonstrates superior resolution compared to any other patterning technique shown. Although direct write modulation is advantageous from a cost perspective, its induced index changes are not enough to allow compact bends and is not versatile from a material selection perspective. UV laser writing is advantageous, as long as the feature size for the application is within the resolution limit of the technique. This method avoids the need for production of a photomask, and the longer write times and facility costs associated with e-beam lithography. Masked techniques on the other hand

have great use for high quality volume production but offer longer turnaround and less versatility for the development of new materials with changing designs.

**Table 1.2.** Comparison of various patterning techniques for waveguide fabrication. Asterisks indicate techniques used in this thesis.

| | **Patterning technique** | **Source** | **Minimum Feature size (μm)** | **Write-time (relative)** | **Cost (relative)** | **Material Requirements** |
|---|---|---|---|---|---|---|
| **Masked** | Contact lithography* | Laser or UV lamp | ~1.0 | Short | $ | Photoresist, photomask |
| | Immersion lithography* | Excimer laser | Mask features × $n_{fluid}$ | | $$ | Photoresist, photomask, water resistance |
| | Nanoimprint lithography | PDMS rolling mold | ~0.02 | | $ | Polymer mask mold |
| **Maskless** | Electron-beam lithography | Electron-beam | ~0.01 | Long | $$$ | Electron absorption resist |
| | UV-laser write lithography* | Continuous-wave laser | ~0.8 | Medium | $$ | UV absorption resist |
| | Direct write index modulation | Pulsed or continuous-wave high energy laser | ~5.0 | Medium | $$ | Phase-change or ion-exchange |

After the thin film has been exposed via any of the mentioned methods (or others), etching can be carried out which selectively removes the material in certain places. This leads to the creation of strip or ridge waveguide structures if the exposed film is entirely etched away or not etched through entirely, respectively. Two broad types of etching are typically used: dry-plasma and wet-chemical etching techniques. Reactive ion etching uses gases which are ionized inside of a plasma chamber and directed onto substrates to physically and chemically etch the material at an atomic scale. Deep-reactive ion etching as shown in Fig. 1.1 refers to a process which utilizes multiple modes (referred to as the Bosch process) involving the fast switching of gases to achieve the deposition of a passivation layer and subsequent anisotropic etching to achieve nearly straight 90° sidewalls. Wet etching uses acids or bases to etch the material and the etchant is typically

heated to an appropriate temperature to increase the etch rate. Wet etching allows for the structuring of thin films without the necessity of a plasma chamber. From a facility perspective this is advantageous as only a wet bench is required, and harmful gases such as chlorine or bromine can require costly safety measures for storage and operation. By using acids such as phosphoric acid ($H_3PO_4$), which is a well know acid used in the food industry, processing costs can be minimal and environmental impacts can be mitigated as well due to its widespread use and known waste treatments [49]. However, as shown in Fig 1.1, wet etching is isotropic and leads to curved sidewalls. Both dry and wet etching methods have led to various demonstrations of waveguides, with plasma etching being adopted more due to its batch fabrication, and large wafer scale use. Depending on the material restrictions and thin-film chemistry, various etching techniques may be preferred over others. For the development of non-traditional waveguide materials, it is imperative to discover new etching recipes which may be used for fast turnaround of devices in a cost-effective manner.

### 1.3 The Need for Low-Cost and Versatile Fabrication Techniques for Developing New Functionalities in PICs

Research in silicon photonics has shifted towards a “fabless” approach, where most of the fabrication is handled by a limited number of foundries worldwide [50,51]. This has allowed for the standardization of materials and components and has generated massive progression in the field by providing photonic designers with a reliable source of waveguides, devices and PICs in Si and recently $Si_3N_4$ as well. However, integrated photonics faces limitations in key areas, which need to be addressed and considered as new applications and industries are demanding more from PICs. To realize commercial PICs for many emerging applications, a key hurdle remains the realization of Si based

monolithic active devices such as optical amplifiers and lasers. This would enable not only various new applications in telecommunications, but also open up new sensing capabilities [52] for the detection of biologically relevant species such as viruses and proteins. To address the constant need for new functionalities, applications and requirements of PICs, research and development on novel material platforms and their fabrication methods is crucial. Cost-effective solutions to thin-film processing and hybrid waveguide designs which can stand alone or build on foundry processes are beneficial to research-scale fabrication, and small-scale prototyping. Versatile fabrication techniques such as low temperature deposition, maskless lithography, wet etching, and spin coating, allow for patterning of waveguides and devices in a variety of material systems with fast turn around for testing and research, rather than waiting months for foundry devices. Also, by receiving fabricated silicon chips from a foundry with no $SiO_2$ top-cladding layer or window openings in the $SiO_2$ cladding in certain regions, back-end deposition of non-standard materials such as rare-earth doped oxides using specialized in-house deposition processes can be performed for the realization of optical amplifiers and lasers.

Passive waveguide circuits serve as a basis for amplifiers, lasers and sensors. Low-loss waveguides and high-quality factor resonators are crucial for developing functionalities such as amplifiers and sensors, as they enable high gain and lasing, as well as selective and sensitive sensors. In materials such as Si and $Si_3N_4$ it is therefore advantageous to have flexible and reliable fabrication techniques in order to realize waveguide platforms capable of enabling new functionalities. These fabrication techniques require features such as controllable features sizes for device fabrication,

smooth sidewalls for low-loss, and compatibility with materials that can allow new functionalities in PICs such as rare-earth oxides and polymer layers.

A key function that is still challenging in Si PICs is optical gain or amplification. As long-haul optical communications signals propagate in a fiber, they experience losses due to a variety of sources, and need to be amplified much like electrical signals which require operational amplifiers. To do so, approximately every 50 km, the signal interacts with an optical amplifier, which boosts the power of the signal by supplying light emitted from rare earth ions. These devices are referred to as erbium doped fiber amplifiers (EDFAs) which are comprised of erbium ions embedded in glass fibers. EDFAs convert optical pump energy into an electronic excitation which leads to the stimulated emission of an additional photon under interaction with a signal photon and optical amplification for the network. In integrated photonics, loss is exacerbated, as radiated optical energy is increased due to scattering from thin-film interfaces and waveguide sidewalls, and material absorption is higher due to substrate absorption and thin-film impurities. Due to the smaller devices, the interaction length between the ions and light is reduced in integrated optical amplifiers as well. This creates a challenge for recreating the gain from the EDFA on a thin film platform in devices referred to as erbium doped waveguide amplifiers (EDWAs). To overcome this, high rare earth concentrations are required, and therefore materials with high rare earth solubility such as $Al_2O_3$ [53–55] and $TeO_2$ [56,57] instead of $SiO_2$ are needed, which requires research and development to optimize rare earth amplifiers for PIC applications. Low optical loss waveguide platforms, which depend on high-quality materials and smooth sidewalls with scalable fabrication, are also necessary for high-performance EDWAs.

For photonic lab on-chip sensors, a variety of materials and functionalization steps are required to coat the surface with biologically reactive species. Microfluidics are used to deliver analytes to optical chips, which react with the materials comprising the waveguide structure. These biological reactions on the surface are ‘read’ by the waveguide, which provides real time rapid assessment. Sensing PICs face challenges in terms of integrating the sensing media with optical materials due to the typically higher losses and the simultaneous need to introduce biological functionality. PMMA can be used for not only a low-loss cladding, but also as an attachment layer for biological sensing. Oxide rich polymers are capable of functionalization by chemical or plasma treatment in order to allow additional surface chemistry for reactions with hydrocarbon rich biological species such as viruses, DNA, antibodies or proteins [58–60]. In this manner, a single spin-on polymer layer may be used for multiple functions, which can be combined with rare-earth doped oxides for optically active laser sensors.

By developing in-house processes based on scalable fabrication techniques, new materials can be realized in PICs which allow for mass-producible optically active devices and sensors for the photonic integrated circuit field. Investigating these materials and fabrication techniques is a central theme to this thesis, which utilizes versatile and low-cost methods to realize photonic devices for optical signal routing, amplification, and sensing applications.

## 1.3 Thesis Overview

### 1.3.1 Thesis Objective

The objective of this thesis is to demonstrate low-cost versatile fabrication techniques for the realization of new passive and active devices and sensors for photonic integrated circuits. The achievement of this objective included the development of a PECVD recipe

to deposit low loss $SiOxN_y:H_z$ thin films, the development of a maskless patterning recipe with UV writing to realize passive $Si_3N_4$ waveguide devices, the reactive sputtering and definition of $Al_2O_3:Er^{3+}:Yb^{3+}$ waveguide amplifiers via wet etching, and the hybridization of Si waveguides with $TeO_2$ and PMMA layers for biological sensors. This thesis provides the means to recreate and build on the techniques demonstrated and points towards ways to optimize and improve them.

### 1.3.2 Statement of Thesis Work

This thesis represents a collection of works with the central theme of low cost, versatile fabrication techniques for passive and active devices and sensors. This is realized through a variety of material platform, waveguide and device demonstrations. The thesis includes three published manuscripts and one in preparation for submission. Where published manuscripts are included in the thesis, a preceding statement on the additions that have been made due to thesis preparation can be found.

Chapter 2 provides a theoretical background on modes in waveguides, and how waveguide platforms are designed with a variety of goals in mind that are relevant to the thesis applications. Material platforms that will be experimentally demonstrated in the thesis are introduced, including silicon, silicon nitride, rare earth doped aluminum oxide, and tellurium dioxide, as well as the theory for the devices fabricated and measured, including Sagnac loops, ring resonators, and Distributed Bragg gratings. Two applications are then presented, optical amplifiers and lab-on-chip sensors, with the relevant theory and background to help understand the results shown in later chapters.

Chapter 3 presents a published manuscript on electron cyclotron resonance (ECR)-PECVD of $SiO_xN_y:H_z$ thin films. The film deposition recipe is presented, alongside details of the system, and characterization of the films with and without post annealing.

Refractive index and thickness, optical loss, surface roughness, stoichiometry and hydrogen content were all measured via ellipsometry, prism coupling, atomic-force microscopy (AFM), Rutherford back-scattering spectrometry (RBS), and elastic recoil detection (ERD), respectively.

Chapter 4 presents a published manuscript on prototyping $Si_3N_4$ waveguides using UV writing in negative photoresist. The exposure procedure and its resolution as well as line-edge roughness are characterized via SEM, before patterning $Si_3N_4$ waveguides via RIE. A ring resonator, directional coupler, and Sagnac loop are fabricated and measured, demonstrating a proof of concept and the prototyping potential of photonic devices.

Chapter 5 presents a published manuscript on optical gain achieved in $Al_2O_3:Er^{3+}:Yb^{3+}$ waveguides fabricated via reactive magnetron co-sputtering and wet etching with masked lithography. Polarization insensitive waveguide losses are experimentally shown, and internal net gain is demonstrated in the C-band.

Chapter 6 presents a manuscript in preparation for submission on hybrid Si-$TeO_2$ waveguide DBRs coated in PMMA for biological sensing. Two DBR designs are compared and coated with various materials, and plasma treated PMMA is shown to increase hydrophilicity. Thermal, water and protein sensing are demonstrated on Si-$TeO_2$/PMMA waveguide DBR devices which represents a pathway towards highly sensitive rare-earth integrated laser-based sensors.

Chapter 7 summarizes the work in the thesis and discusses future pathways for building on the work presented.

### 1.3.3 Summary of Publications & Contributions

The following is a list of publications by the author which are included in the thesis:

- **D. B. Bonneville**, K. Miarabbas Kiani, H. C. Frankis, R. Arbi, M. Munir, M. Albert, K. N. Sask, A. Turak, A. P. Knights, and J. D. B. Bradley, “Hybrid Si-$TeO_2$ waveguide Bragg resonators coated in PMMA for biological sensing,” *Manuscript in preparation.*
- **D. B. Bonneville**, J. W. Miller, C. Smyth, and J. D. B. Bradley, “Low temperature and low pressure silicon nitride deposition by ECR-PECVD for optical waveguides,” Applied Sciences **11**(2110), 2021.
- **D. B. Bonneville**, H. C. Frankis, R. Wang, and J. D. B. Bradley, "Erbium-ytterbium co-doped aluminum oxide waveguide amplifiers fabricated by reactive co-sputtering and wet chemical etching," Optics Express **28**(20), 30130–30140 (2020).
- **D. B. Bonneville**, M. A. Méndez-Rosales, H. C. Frankis, L. Monteiro Gonçalves, R. N. Kleiman, and J. D. B. Bradley, "Flexible and low-cost fabrication of optical waveguides by UV laser resist-mask writing," Optical Materials Express **9**(4), 1728–1737 (2019).

The author has also contributed to the following conference presentations, posters, and proceedings:

- **D. B. Bonneville**, K. Miarabbas Kiani, H. C. Frankis, R. Arbi, M. Munir, M. Albert, K. N. Sask, A. Turak, A. P. Knights, and J. D. B. Bradley, “Hybrid Si-$TeO_2$ waveguide Bragg resonators coated in PMMA for biological sensing,” presented at Photonics North, Virtual Conference, June 1$^{st}$ 2021, paper 255-Ghdb-14.
- **D. B. Bonneville**, J. W. Miller, C. Smyth, and J. D. B. Bradley, “Low temperature silicon oxy-nitride deposition by plasma enhanced chemical vapour deposition,”

presented at Photonics North, Virtual Conference, 26–28 May 2020, paper PM-3-27-3.

- **D. B. Bonneville**, H. C. Frankis, R. Wang, and J. D. B. Bradley, “Reactive co-sputtering and wet etching of Er:Yb co-doped $Al_2O_3$ waveguides with optical gain,” presented at Photonics North, Quebec City, Canada, 21–23 May 2019.
- **D. B. Bonneville**, M. A. Méndez-Rosales, H. C. Frankis, and J. D. B. Bradley, “UV laser resist-mask writing for low-cost prototyping of integrated optical devices,” in Conference on Lasers and Electro-Optics, San Jose, CA, 2019, OSA Technical Digest (online) (Optical Society of America, 2019), paper SF2O.4.
- **D. B. Bonneville**, H. C. Frankis, and J. D. B. Bradley, “Direct-write photolithography for rapid prototyping of silicon nitride waveguides on silicon,” presented at The 14th International Ceramics Congress (CIMTEC), Perugia, Italy, 4–8 June 2018. (Poster)
- J. Miller**, D. B. Bonneville***, N. Vadivelu, Z. Khatami, J. Wojcik, J. D. B. Bradley, and P. Mascher, “Green light emission from terbium-doped Si-based thin films: ECR-PECVD films doped via a circular HV magnetron sputtering source,” Photonics North, Ottawa, Canada, 2017, Proceedings of Photonics North, paper 15.20.

The author has also contributed as a co-author on the following publications which are not relevant to the thesis:

- K. Miarabbas Kiani, **D. B. Bonneville,** A. P. Knights, and J. D. B. Bradley, “High-Q $TeO_2$– Si Hybrid Microring Resonators,” Applied Sciences **12**(3), 1363 (2022).

- K. Miarabbas Kiani, H. C. Frankis, C. M. Naraine, D. B. Bonneville, A. P. Knights, and J. D. B. Bradley, “Lasing in a Hybrid Rare-Earth Silicon Microdisk,” Laser & Photonics Reviews **16**(1), 2100348 (2022).
- H. C. Frankis, **D. B. Bonneville**, and J. D. B. Bradley, “Tellurite glass microcavity resonators integrated on a silicon photonics platform,” Journal of Optical Microsystems **1**(2), 24002 (2021).
- R. Wang, H. C. Frankis, H. M. Mbonde, **D. B. Bonneville**, and J. D. B. Bradley, "Erbium-ytterbium co-doped aluminum oxide thin films: co-sputtering deposition, photoluminescence, luminescent lifetime, energy transfer and quenching fraction," Optical Materials 111 110692, (2020).
- H. C. Frankis, H. M. Mbonde, **D. B. Bonneville**, C. Zhang, R. Mateman, A. Leinse, and J. D. B. Bradley, "Erbium-doped $TeO_2$-coated $Si_3N_4$ waveguide amplifiers with 5 dB net gain," Photonics Research **8**(2), 127–134 (2020).
- H. C. Frankis, K. Miarabbas Kiani, **D. B. Bonneville**, C. Zhang, S. Norris, R. Mateman, A. Leinse, N. D. Bassim, A. P. Knights, and J. D. B. Bradley, "Low-loss $TeO_2$-coated $Si_3N_4$ waveguides for application in photonic integrated circuits," Optics Express **27**(9), 12529-12540 (2019).
- H. C. Frankis, D. Su, **D. B. Bonneville**, and J. D. B. Bradley, “A tellurium oxide microcavity resonator sensor integrated on-chip with a silicon waveguide,” Sensors **18**(11), 4061 (2018).
- A. Hanu, et al., “NEUDOSE: A CubeSat mission for dosimetry of charged particles and neutrons in low-earth orbit.” Radiation Research **187**(1), (2016).

## 1.4 References


1. Q. Cheng, M. Bahadori, M. Glick, S. Rumley, and K. Bergman, “Recent advances in optical technologies for data centers: a review,” Optica, vol. 5, no. 11, p. 1354, 2018.
2. Z. W. Xu, “Cloud-sea computing systems: Towards thousand-fold improvement in performance per watt for the coming zettabyte era,” J. Comput. Sci. Technol., vol. 29, no. 2, pp. 177–181, 2014.
3. R. Y. Shah and Y. K. Agrawal, “Introduction to fiber optics: sensors for biomedical applications,” Indian J. Pharm. Sci., vol. 73, no. 1, pp. 17–22, 2011.
4. Z. Li, I. Shubin, and X. Zhou, “Optical interconnects: recent advances and future challenges,” Opt. Express, vol. 23, no. 3, p. 3717, 2015.
5. R. A. Soref and B. R. Bennett, “Electrooptical effects in silicon,” IEEE J. Quantum Electron., vol. 23, no. 1, pp. 123–129, 1987.
6. E. Timurdogan, Z. Su, R. J. Shiue, M. J. Byrd, C. V. Poulton, K. Jabon, C. DeRose, B. R. Moss, E. S. Hosseini, I. Duzevik, M. Whitson, R. P. Millman, D. A. Atlas, and M. R. Watts, “400G Silicon photonics integrated circuit transceiver chipsets for CPO, OBO, and pluggable modules,” Opt. Fiber Commun. Conf. (OFC), OSA Tech. Dig., 2020.
7. D. J. Thomson, F. Y. Gardes, J. M. Fedeli, S. Zlatanovic, Y. Hu, B. P. Kuo, E. Myslivets, N. Alic, S. Radic, G. Z. Mashanovich, and G. T. Reed, “50-Gb/s silicon optical modulator,” IEEE Photon. Technol. Lett., vol. 24, no. 4, pp. 234–236, 2011.
8. M. He, M. Xu, Y. Ren, J. Jian, Z. Ruan, Y. Xu, S. Gao, S. Sun, X. Wen, L. Zhou, and L. Liu, “High-performance hybrid silicon and lithium niobate Mach–Zehnder modulators for 100 Gbit s-1 and beyond,” Nat. Photonics, vol. 13, no. 5, pp. 359–364, 2019.
9. A. Beling and J. C. Campbell, “InP-Based high-speed photodetectors,” J. Light. Technol., vol. 27, no. 3, pp. 343–355, 2009.
10. W. Yao, M. K. Smit, and M. J. Wale, “Monolithic 300 Gb/s parallel transmitter in InP-based generic photonic integration technology,” IEEE J. Sel. Top. Quantum Electron., vol. 24, no. 1, p. 6100711, 2017.
11. J. D. B. Bradley, P. E. Jessop, and A. P. Knights, “Silicon waveguide-integrated optical power monitor with enhanced sensitivity at 1550 nm,” Appl. Phys. Lett., vol. 86, no. 24, p. 241103, 2005.
12. J. J. Ackert, D. J. Thomson, L. Shen, A. C. Peacock, P. E. Jessop, G. T. Reed, G. Z. Mashanovich, and A. P. Knights, “High-speed detection at two micrometres with monolithic silicon photodiodes,” Nat. Photonics, vol. 9, no. 6, pp. 393–396, 2015.
13. L. Vivien, A. Polzer, D. Marris-Morini, J. Osmond, J. M. Hartmann, P. Crozat, E. Cassan, C. Kopp, H. Zimmermann, and J. M. Fédéli, “Zero-bias 40 Gbit/s germanium waveguide photodetector on silicon,” Opt. Express, vol. 20, no. 2, p. 1096, 2012.
14. S. A. Srinivasan, M. Pantouvaki, S. Gupta, H. T. Chen, P. Verheyen, G. Lepage, G. Roelkens, K. Saraswat, D. Van Thourhout, P. Absil, and J. Van Campenhout, “56 Gb/s germanium waveguide electro-absorption modulator,” J. Light. Technol., vol. 34, no. 2, pp. 419–424, 2015.
15. D. X. Xu, M. Vachon, A. Densmore, R. Ma, S. Janz, A. Delâge, J. Lapointe, P. Cheben, J. H. Schmid, E. Post, and S. Messaoudène, “Real-time cancellation of

temperature induced resonance shifts in SOI wire waveguide ring resonator label-free biosensor arrays," Opt. Express, vol. 18, no. 22, p. 22867, 2010.
16. D. Liang and J. E. Bowers, "Recent progress in lasers on silicon," Nat. Photonics, vol. 4, no. 8, pp. 511–517, 2010.
17. R. E. Camacho-Aguilera, Y. Cai, N. Patel, J. T. Bessette, M. Romagnoli, L. C. Kimerling, and J. Michel, "An electrically pumped Ge-on-Si laser," Opt. InfoBase Conf. Pap., vol. 20, no. 10, pp. 11316–11320, 2012.
18. M. Smit, K. Williams, and J. Van Der Tol, "Past, present, and future of InP-based photonic integration," APL Photonics, vol. 4, no. 5, 2019.
19. A. W. Fang, H. Park, O. Cohen, R. Jones, M. J. Paniccia, and J. E. Bowers, "Electrically pumped hybrid AlGaInAs-silicon evanescent laser," Opt. Express, vol. 14, no. 20, p. 9203, 2006.
20. K. Jinguji, "Mach-zehnder interferometer type optical waveguide coupler with wavelength-flattened coupling ratio," Electron. Lett., vol. 26, no. 17, pp. 1326–1327, 1990.
21. B. E. Little, S. T. Chu, H. A. Haus, J. A. Foresi, and J. P. Laine,, "Microring resonator channel dropping filters," J. Light. Technol., vol. 15, no. 6, pp. 998–1005, 1997.
22. J. Notaros, N. Li, C. V. Poulton, Z. Su, M. J. Byrd, E. S. Magden, E. Timurdogan, C. Baiocco, N. M. Fahrenkopf, and M. R. Watts, "CMOS-Compatible optical phased array powered by a monolithically-integrated erbium laser," J. Light. Technol., vol. 37, no. 24, pp. 5982–5987, 2019.
23. C. V. Poulton, M. J. Byrd, P. Russo, E. Timurdogan, M. Khandaker, D. Vermeulen, and M. R. Watts, "Long-range LiDAR and free-space data communication with high-performance optical phased arrays," IEEE J. Sel. Top. Quantum Electron., vol. 25, no. 5, pp. 1–8, 2019.
24. R. Soref, "The past, present, and future of silicon photonics," IEEE J. Sel. Top. Quantum Electron., vol. 12, no. 6, pp. 1678–1687, 2006.
25. D. Thomson D, A. Zilkie, J. E. Bowers, T. Komljenovic, G. T. Reed, L. Vivien, D. Marris-Morini, E. Cassan, L. Virot, J. M. Fédéli, J. M. Hartmann, J. H. Schmid, D. X. Xu, F. Boeuf, P. O'Brien, G. Z. Mashanovich, and M. Nedeljkovic, "Roadmap on silicon photonics," J. Opt., vol. 18, no. 7, p. 073003, 2016.
26. C. G. H. Roeloffzen, M. Hoekman, E. J. Klein, L. S. Wevers, R. B. Timens, D. Marchenko, D. Geskus, R. Dekker, A. Alippi, R. Grootjans, A. van Rees, R. M. Oldenbeuving, J. P. Epping, R. G. Heideman, K. Wörhoff, A. Leinse, D. Geuzebroek, E. Schreuder, P. W. L. van Dijk, I. Visscher, C. Taddei, Y. Fan, C. Taballione, and Y. Liu, D. Marpaung, L. Zhuang, M. Benelajla and K. Boller, "Low-loss si3n4 triplex optical waveguides: Technology and applications overview," IEEE J. Sel. Top. Quantum Electron., vol. 24, no. 4, 2018.
27. D. J. Blumenthal, R. Heideman, D. Geuzebroek, A. Leinse, and C. Roeloffzen,, "Silicon nitride in silicon photonics," Proc. IEEE., vol. 106, no. 12, 2018.
28. J. F. Bauters, M. J. Heck, D. D. John, J. S. Barton, C. M. Bruinink, A. Leinse, R. G. Heideman, D. J. Blumenthal, and J. E. Bowers, "Planar waveguides with less than 0.1 dB/m propagation loss fabricated with wafer bonding," Opt. Express, vol. 19, no. 24, pp. 24090–101, 2011.

29. J. F. Bauters, M. J. R. Heck, D. John, D. Dai, M.-C. Tien, J. S. Barton, A. Leinse, R. G. Heideman, D. J. Blumenthal, and J. E. Bowers, “Ultra-low-loss high-aspect-ratio Si3N4 waveguides,” Opt. Express, vol. 19, no. 4, pp. 3163–3174, 2011.
30. W. D. Sacher, J. C. Mikkelsen, Y. Huang, J. C. Mak, Z. Yong, X. Luo, Y. Li, P. Dumais, J. Jiang, D. Goodwill, E. Bernier, P. G. Q. Lo, and J. K. S. Poon, “Monolithically integrated multilayer silicon nitride-on-silicon waveguide platforms for 3-D photonic circuits and devices,” Proc. IEEE, vol. 106, no. 12, pp. 2232–2245, 2018.
31. P. Xing, D. Ma, K. J. Ooi, J. W. Choi, A. M. Agarwal, and D. Tan, “CMOS-compatible PECVD silicon carbide platform for linear and nonlinear optics,” ACS Photonics, vol. 6, no. 5, pp. 1162–1167, 2019.
32. T. Li, M. Nedeljkovic, N.Hattasan, W.Cao, Z.Qu, C. G. Littlejohns, J.S.Penades, L. Mastronardi, V. Mittal, D. Benedikovic, D.J. Thomson, F. Y. Gardes, H.Wu, Z. Zhou, and G. Z. Mashanovich, “Ge-on-Si modulators operating at mid-infrared wavelengths up to 8 μm,” Photonics Res., vol. 7, no. 8, p. 828, 2019.
33. H. Ma, A. K.-Y. Jen, L. R. Dalton, “Polymer-based optical waveguides: materials, processing, and devices,” Adv. Mater., vol. 14, no. 19, pp. 1339–1365, 2002.
34. K. Tamaki, H. Takase, Y. Eriyama, and T. Ukachi, “Recent progress on polymer waveguide materials,” J. Photopolym. Sci. Tehchnol., vol. 16, no. 5. pp. 639–648, 2003.
35. W. Sohler, H. Hu, R. Ricken, V. Quiring, C. Vannahme, H. Herrmann, D. Büchter, S. Reza, W. Grundkötter, S. Orlov, and H. Suche, “Integrated optical devices in lithium niobate,” Opt. Photonics News, vol. 19, no. 1, pp. 24–31, 2008.
36. C. R. Doerr, “Silicon photonic integration in telecommunications,” Front. Phys., vol. 3, no. 37, pp. 1–16, 2015.
37. R. Sabella, “Silicon photonics for 5G and future networks,” IEEE J. Sel. Top. Quantum Electron., vol. 26, no. 2, pp. 1–11, 2019.
38. J. K. Doylend and S. Gupta, “An overview of silicon photonics for LIDAR,” Int. Soc. Opt. Photonics, p. 112850.
39. A. F. Gavela, D. G. García, J. C. Ramirez, and L. M. Lechuga, “Last advances in silicon-based optical biosensors,” Sensors (Switzerland), vol. 16, no. 3, pp. 1–15, 2016.
40. A. Politi, J. C. Matthews, M. G. Thompson, and J. L. O'Brien, “Integrated quantum photonics,” IEEE J. Sel. Top. Quantum Electron., vol. 15, no. 6, pp. 1673–1684, 2009.
41. J. C. Adcock, J. Bao, Y. Chi, X. Chen, D. Bacco, Q. Gong, L. K. Oxenløwe, J. Wang, and Y. Ding, “Advances in silicon quantum photonics,” IEEE J. Sel. Top. Quantum Electron., vol. 27, no. 2, pp. 1–24, 2020.
42. A. Menéndez, P. Sánchez, and D. Gómez, “Chapter 2 deposition of thin films : PECVD process,” Bentham Sci. pp. 29–57, 2013.
43. C. Y. and J. Pham, “Characteristic study of silicon nitride films deposited by LPCVD and PECVD,” Silicon, vol. 10, no. 6, pp. 2561–2567, 2018.
44. P. J. Kelly and R. D. Arnell, “Magnetron sputtering: A review of recent developments and applications,” Vacuum, vol. 56, no. 3, pp. 159–172, 2000.

45. M. Demirtas, C. Odaci, N. K. Perkgoz, C. Sevik, and F. Ay, “Low loss atomic layer deposited $Al_2O_3$ waveguides for applications in on-chip optical amplifiers,” IEEE J. Sel. Top. Quantum Electron., vol. 24, no. 4, 2018.
46. R. W. Johnson, A. Hultqvist, and S. F. Bent, “A brief review of atomic layer deposition: From fundamentals to applications,” Mater. Today, vol. 17, no. 5, pp. 236–246, 2014.
47. J. Rönn, W. Zhang, A. Autere, X. Leroux, L. Pakarinen, C. Alonso-Ramos, A. Säynätjoki, H. Lipsanen, L. Vivien, E. Cassan, and Z. Sun, “Ultra-high on-chip optical gain in erbium-based hybrid slot waveguides,” Nat. Commun., vol. 10, no. 1, pp. 1–9, 2019.
48. J. Miller, “A novel approach to thin film deposition and rare-earth incorporation for silicon integrated photonics,” McMaster University, 2020.
49. S. Belboom, C. Szöcs, and A. Léonard, “Environmental impacts of phosphoric acid production using di-hemihydrate process: A Belgian case study,” J. Clean. Prod., vol. 108, pp. 978–986, 2015.
50. M. Hochberg and T. Baehr-Jones, “Towards fabless silicon photonics,” Nat. Photonics, vol. 4, no. 8, pp. 492–494, 2010.
51. M. Hochberg, N. C. Harris, R. Ding, Y. Zhang, A. Novack, Z. Xuan, and T. Baehr-Jones, “Silicon photonics: the next fabless semiconductor industry,” IEEE Solid-State Circuits Mag., vol. 5, no. 1, pp. 48–58, 2013.
52. R. Chandrasekar, Z. J. Lapin, A. S. Nichols, R. M. Braun, and A. W. Fountain, “Photonic integrated circuits for department of defense-relevant chemical and biological sensing applications: state-of-the-art and future outlooks,” Opt. Eng., vol. 58, no. 02, p. 1, 2019.
53. K. Worhoff, J. D. Bradley, F. Ay, D. Geskus, T. P. Blauwendraat, and M. Pollnau, “Reliable low-cost fabrication of low-loss $Al_2O_3$:$Er^{3+}$ waveguides with 5.4-dB optical gain,” IEEE J. Quantum Electron., vol. 25, no. 5, pp. 454–461, 2009.
54. S. A. Vázquez-Córdova, M. Dijkstra, E. H. Bernhardi, F. Ay, K. Wörhoff, J. L. Herek, S. M. García-Blanco, and M. Pollnau, “Erbium-doped spiral amplifiers with 20 dB of net gain on silicon,” Opt. Express, vol. 22, no. 21, p. 25993, 2014.
55. J. D. B. Bradley, L. Agazzi, D. Geskus, F. Ay, K. Wörhoff, and M. Pollnau, “Gain bandwidth of 80 nm and 2 dB/cm peak gain in $Al_2O_3$:$Er^{3+}$ optical amplifiers on silicon,” JOSA B, vol. 27, no. 2, pp. 187–196, 2010.
56. K. Vu and S. Madden, “Tellurium dioxide erbium doped planar rib waveguide amplifiers with net gain and 2.8dB / cm internal gain,” Opt. Express, vol. 18, no. 18, pp. 19192–19200, 2010.
57. K. Vu, S. Farahani, and S. Madden, “980nm pumped erbium doped tellurium oxide planar rib waveguide laser and amplifier with gain in S, C and L band,” Opt. Express, vol. 23, no. 2, p. 747, 2015.
58. S. Sathish, N. Ishizu, and A. Q. Shen, “Air plasma-enhanced covalent functionalization of poly(methyl methacrylate): high-throughput protein immobilization for miniaturized bioassays,” ACS Appl. Mater. Interfaces, vol. 11, no. 49, pp. 46350–46360, 2019.
59. D. Kohler, G. Schindler, L. Hahn, J. Milvich, A. Hofmann, K. Länge, W. Freude and C. Koos, “Biophotonic sensors with integrated Si 3 N 4 -organic hybrid ( SiNOH ) lasers for point-of-care diagnostics,” Light Sci. Appl., vol. 10, no. 64, 2021.

60. R. Landgraf, M. K. Kaiser, J. Posseckardt, B. Adolphi, and W. J. Fischer, “Functionalization of polymer sensor surfaces by oxygen plasma treatment,” Procedia Chem., vol. 1, no. 1, pp. 1015–1018, 2009.

# Chapter 2

## Background and Theory

This chapter includes an overview on integrated optical waveguides along with their fundamental principles and design methodologies as well as an introduction into the relevant waveguide materials, devices, and applications for this thesis. The design methodologies are presented followed by an introduction and review on Si compatible material platforms as well as those compatible with rare-earth dopants. Three passive devices, the Sagnac loop, ring resonator, and Bragg grating are introduced in terms of their working physical theory. Two active devices, optical amplifiers and photonic lab on-chip sensors are introduced with background and theory which serve to give context for understanding results in the thesis.

### 2.1 Optical Waveguides

#### 2.1.1 Integrated Optical Waveguides

Confining light in glass fibers allows for routing of signals from rack-to-rack in data centers, the creation of controlled optical pathways for sensing, rare-earth-based optical amplification and many more applications. Replicating this behaviour in thin films, patterned such that optical fields are confined to the dimensions typical with a small micro-chip, allows for supporting the very same signals that optical fibers do, but on a platform capable of small scale electrical, chemical, and photonic manipulation. These patterned thin films, which manipulate and direct optical fields on-chip, are referred to as strip, channel or ridge waveguides. Generally speaking, a waveguide is anything that confines a wave, such as a hollow conductive metal pipe for microwave propagation, or even a horn for acoustic waves. Exploring the confinement and guiding of optical waves on a

microchip has been an active area of scientific research for decades [1] as it opens up a new paradigm of applications for not only communications but other fields including healthcare and environmental monitoring [2].

These confined fields have distinct characteristics which are governed by the electric field solutions to Maxwell's equations [3], and are affected by the material properties and geometry of the waveguide. These solutions are referred to as modes and are considered to either be guided (transmitted), or radiation (lost) solutions for the waveguide devices at particular electromagnetic wavelengths. Finite element method (FEM) solvers are popularly used to calculate the eigenmode solutions for the electromagnetic field distribution in a waveguide and are used to design photonic devices in a variety of waveguide material systems and structures. These solvers take into account the characteristics of the physical media such as its refractive index, dispersion, geometry, and other features, and on a defined mesh and boundary conditions, solve the electric and magnetic field properties that would be confined for a given wavelength in the structure. These 2D properties of such modes are the focus of the simulation work in this thesis. Other solvers such as 3D finite-difference time-domain (FDTD) are also widely used in photonics but are out of the scope of the theory presented here. The designs in this thesis are governed by the effective index and calculations using the power percentage in various material components of the waveguide design, which can be determined with 2D methods. Figure 2.1 presents cross sections of typical Si and $Si_3N_4$ waveguides with the solved electric fields profiles of the fundamental transverse electric modes in a) and b) respectively. These modes constitute the shape of the field as it propagates through the structure and can therefore be subsequently used to visualize the

way optical signals confine themselves to the waveguide. Figure 2.1 demonstrates single-mode operation, where the waveguide width is below a certain cut-off, which only allows for the excitement of a single intensity maximum. In most cases this is desirable as higher order modes tend to have higher overlap with sidewalls and interfere with one another leading to increased scattering loss and unpredictable waveguide behaviour.

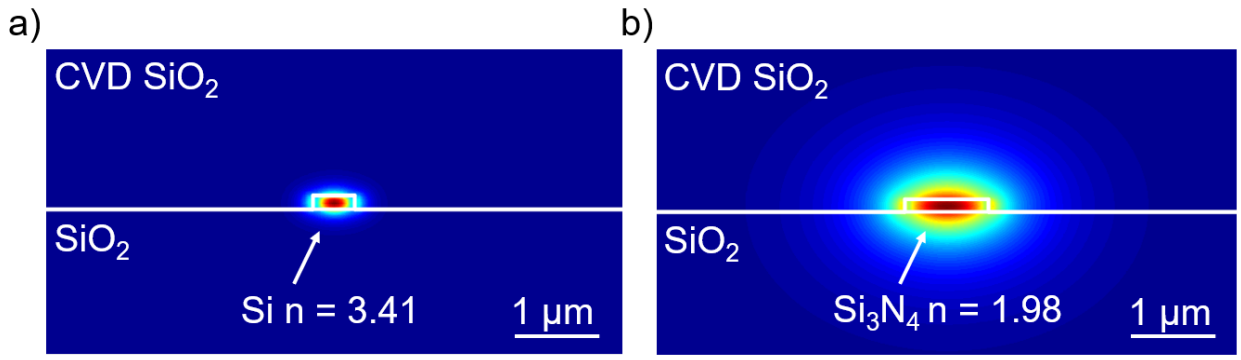


**Figure 2.1.** Calculated mode profiles for fundamental transverse electric modes at 1550 nm of a) an Si and b) an $Si_3N_4$ waveguide with widths of 0.5 and 1.0 µm and heights of 0.22 and 0.2 µm, respectively.

Figure 2.1 represents two different waveguide materials, silicon and silicon nitride, with largely varying refractive indices and consequentially different confinement parameters relative to the waveguide core. The power density of the optical field is demonstrated to be shared amongst the surrounding materials of the main waveguide core material, which will be discussed as an advantage for certain applications (e.g., sensors) in the forthcoming chapters. Optical fields that exist away from the waveguide core, such as those at the surface of the device are known as evanescent waves, which are waves that have an exponentially decreasing power with distance. These fields are ‘accessible’ to the surrounding environment and world, and capable of coupling with gases or liquids on the top surface, or interaction with particles or optically active elements embedded in

surrounding dielectric media. Additionally, evanescent fields can be accessed by other adjacent waveguides, leading to the coupling of fields between adjacent structures, transfer of power, and subsequent sharing or generation of new modes. This is the basis for many waveguide devices where the gap or distance between coupled waveguides, rings, disks, interference circuits, loops or grating devices and many others can be tuned and designed to achieve various application specifications. These coupled devices form the basis for much of the functionality of PICs, where patterned waveguide devices are responsible for the transmission, manipulation and distribution of signals and information.

### 2.1.2 Waveguide Design

To anticipate the behaviour and aid in the design of such optical components various methodologies are used which involve varying features such as the waveguide film height, width, and structure type, as well as the core and surrounding cladding materials while tracking the effective index, modal area, material overlap as well as other calculated parameters. Changes to these features of the waveguide and top cladding are key to parameters that govern device performance and can be used to tailor behaviour of the modes. Factors such as single-mode operation, preferential material overlap, polarization sensitive or insensitive capabilities, fiber-mode overlap, signal/pump overlap, and low-loss bends are just some of the properties that can be tuned in this manner. To summarize the parameters of interest for this thesis, Table 2.1 has been constructed which demonstrates the waveguide properties of importance, parameters of interest, and the impact on waveguide operation and performance. Each parameter is not mutually exclusive in their effect on the waveguide properties, and in many cases changes to one design parameter can lead to variations in other properties. In the following paragraphs

each waveguide property and its associated design considerations and device performance impacts are briefly discussed.

**Table 2.1.** Waveguide properties and design parameters of interest

| **Waveguide property** | **Parameters of interest for waveguide design** | **Performance impact relevant for this work** |
|---|---|---|
| Single-mode cut-off | $n_{eff,r}$ vs. WG width + height | Mode shape, loss, minimizing higher-order mode crosstalk |
| Modal area & material overlap | WG & cladding width + height | Loss, functionality, hybridization |
| Polarization | WG structure & width/height aspect ratio | Polarization insensitive amplifiers, increased film or surface overlap |
| Fiber-waveguide mode overlap | Fiber mode area/WG mode area | Fiber-chip coupling losses |
| Signal-pump mode overlap | Signal mode area/pump mode area | Pumping efficiency |
| Minimum bend radius | $n_{eff,r}$ & $n_{eff,i}$ vs radius<br>[Q estimation] | Device size, ring FSR |

Single-mode cut-off is perhaps the most important factor when it comes to deciding waveguide height and width. Therefore, it guides subsequent decisions and calculations such as the determining the minimum bending radius and optical field overlap with various materials and between the signal and pump or fiber modes. To determine the single-mode cutoff of a waveguide design, the material cross section is generated using software such as Synopsys RSoft FemSIM mode solver, and after selecting the wavelength, mesh details, and other constraints perhaps set by fabrication such as the minimum width or layer thicknesses as decided by foundry, the waveguide core width is varied from a minimum to maximum typically within the range of ~0.2–5.0 μm depending on the refractive index. The effective index, which represents a weighted average of the refractive index of the different waveguide materials ‘seen’ or occupied by the confined field, has a unique value for each mode and waveguide width. The electric field solution

with the highest effective index is generally referred to as the fundamental mode and is the most prominently confined mode which will be guided and transmitted through the waveguide. Other modes, with lower, and typically very close effective indices to one another, are referred to as higher order guided or radiation and slab modes. These modes are not preferentially excited or guided in the waveguide, and unless a lower order mode exists with an effective index considerably higher than the slab modes, the waveguide is referred to as single mode. In the case where fields with multiple intensity lobes satisfy Maxwell's equations such that higher-order modes are allowed to operate with a refractive index higher than that of the slab mode, multi-mode operation takes place. This multi-mode operation is usually undesirable unless designing for spatial multiplexing schemes which are garnering interest for telecommunications, and for the purposes of this thesis are considered lossy and counterproductive to the design of optically active devices and sensors. When a higher order mode effective index becomes greater than the slab mode's effective index, the single-mode cutoff width is discovered as multiple intensity lobes will begin to propagate. In design, this is an important merit for deciding features to constitute a photonic integrated circuit layout. Layer thickness, which depending on the fabrication process may either be fixed or available for variation such as in the case of a shallow etch step used for a rib design [4], also ends up deciding the geometry of the waveguide core.

After discerning the single-mode cutoff width, typically two-dimensional integration of the optical intensity is carried out for each part of the waveguide structure, which reveals the percentage of power propagating in each medium that constitutes the waveguide cross section. This, in conjunction with calculating the modal area using equation (1)

shown below, are useful for tailoring designs such as hybrid rare-earth integrated amplifiers which require a significant amount of the optical power to not be in the main waveguide, but the surrounding hybridizing gain medium.

$$Effective\ Mode\ Area = \frac{\int (|\mathrm{E}|^2 dA)^2}{\int |\mathrm{E}|^4\, dA}. \quad (1)$$

Similarly, a strategy for sensor devices is to increase the optical overlap with the top layer and the analyte of interest, which likewise allows for more sensitive devices. Coupling of various waveguide devices is also calculated based in part on optical power overlap, allowing design of devices such as couplers, rings and gratings.

Guided optical modes for waveguides as described by electrodynamics typically exist as two possible primarily transverse-polarized field solutions, electric or magnetic. Traditionally, quasi-transverse electric (TE) modes dominate in the application space due to their higher $n_{eff}$ and increased confinement in comparison to quasi-transverse magnetic (TM) modes. In some cases, especially for sensor devices in which overlap with the top layer is preferential [5], there are designs where TM modes, instead of TE modes (or designs which allow both) are desirable. To achieve either mode, the aspect ratio of the waveguide can be changed to give preferential geometry for the TE or TM case or similar properties to both, for example by altering the design of a strip waveguide or selecting a specific ridge waveguide structure which can readily support both in the single mode regime. These features can be predicted using the effective index from mode solutions, and by altering the thickness and width of the waveguide. As an example relevant to this work, simulation of an $Al_2O_3$ ridge waveguide's modal properties are shown in Fig. 2.2. The figure shows a) the cross section of the design, b) mode profiles for TE and TM solutions at 1550 nm, the c) effective index and d) modal overlap along with e) modal

area and f) fiber overlap. The single mode cut-off width is labelled clearly for an $Al_2O_3$ waveguide, as well as the dimensions which allow for TE and TM mode operation as a dashed line in c).

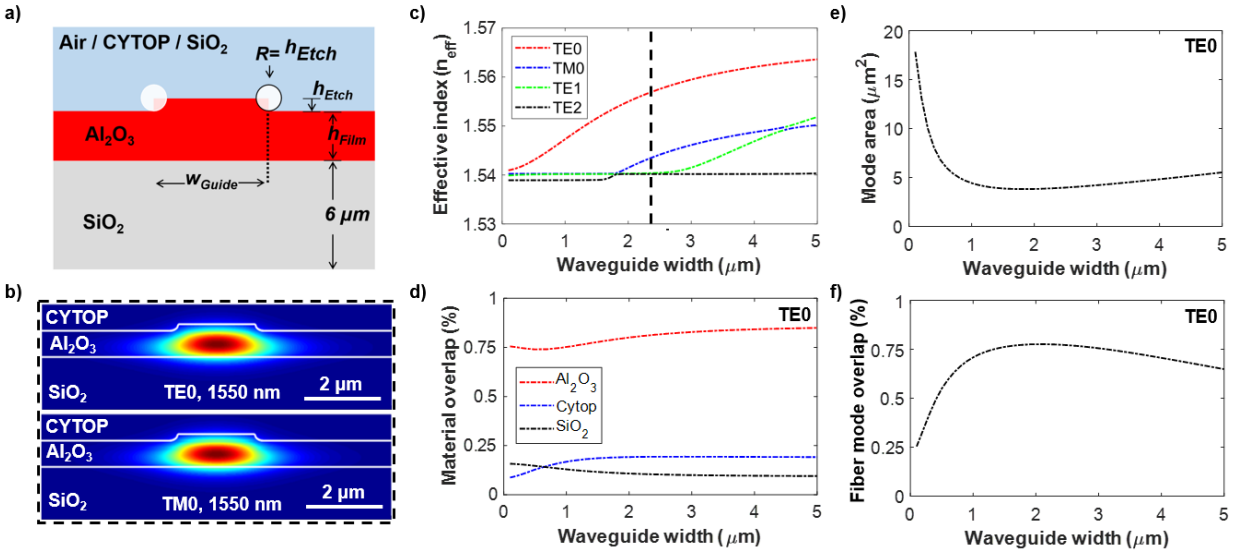


**Figure 2.2.** a) Design cross section, b) mode profiles for TE and TM solutions at 1550 nm c) effective index, d) modal overlap, e) modal area and f) fiber overlap for 2.5 μm diameter gaussian mode.

The overlap between the optical field of different modes can be used to estimate key features such as fiber-chip coupling losses, and signal/pump overlap for efficient active devices. Integrals of the electric fields, and the calculated modal areas and material power overlaps, are used to estimate the fiber-edge coupling and signal/pump overlaps. The fiber-chip coupling efficiency is typically optimized by expanding the mode of the on-chip waveguide in order to make it more closely match the mode supported by the input/output fiber. This is done traditionally by inverse tapering the waveguide to a narrower width, causing it to expand to the desired size and shape. Pump/signal overlap is an important parameter to take into consideration for the design of active components where the pump

and signal wavelength are far apart on the spectrum. For example, for erbium-doped waveguide amplifiers and the case of pumping at ~980 nm with a ~1530 nm signal, the pump-signal overlap can be significantly lower compared to 1480 nm pumping. Figure 2.2 e) demonstrates the overlap percentage between the waveguide mode a gaussian mode representing one launched from a tapered fiber, simulated in RSoft FemSIM using a 2.5 μm diameter. In the case of optical amplifiers for example, it is crucial to minimize fiber-chip coupling loss to achieve external gain, and for the $Al_2O_3$ ridge waveguides studied in this thesis this can be challenging due to the asymmetric waveguide mode compared to the symmetric fiber mode.

Bending waveguides is crucial for packing functionality onto a photonic chip, and the minimum bend radius is a key parameter for devices such as the ring resonator, or spirals. The minimum bend radius is typically set by the maximum allowable radiation loss due to the bent waveguide. Much like inertial forces when turning around a corner in a vehicle, the optical mode wants to propagate straight, and when perturbed by a bend in the waveguide, the outer portion of the mode has a chance to radiate out into the surrounding materials, as it may satisfy imaginary solutions of the effective index, referring to radiated lost energy. This can be avoided with gradual adiabatic transitions into the bends, but more importantly by not making the bends too sharp and having large enough bending radii which allows smooth propagation of the optical modes around the photonic chip, as demonstrated in the inset of Figure 2.3. To determine the minimum bend radius in RSoft FemSIM, a radius is selected which tells the mode solver to treat the calculation as if it were currently in a bent cross section of a waveguide. This bend causes an expansion of the mode, and increased values in the imaginary effective index, which typically

constitutes the boundary condition interaction. Here, the quality factor of the bend is determined using the following equation which considers the real and imaginary parts of the effective index:

$$Q_{bending} = \frac{n_{eff,r}}{4\pi n_{eff,i}}. \quad (2)$$

By plotting $Q_{bending}$ vs. radius, a rule-of-thumb can be used which decides to accept designs and bends with a quality factor of at least $10^6$ (a loss of < $1.0 \times 10^{-3}$ dB/cm). It can be anticipated that any designs which satisfy this requirement will be as compact as possible and provide low-loss bends. Figure 2.3 demonstrates an example of the bend loss calculated for the $Al_2O_3$ design demonstrated in Figure 2.2, which allows for the decision of a safe minimum bending radius of > 1.6 mm. Included here as insets are also the logarithm of the bending quality factor, and the propagation loss calculated in the bend using,

$$Loss_{bending} = -20 \times \log_{10} e^{\frac{-2\pi \times n_{eff,i}}{\lambda}}. \quad (3)$$

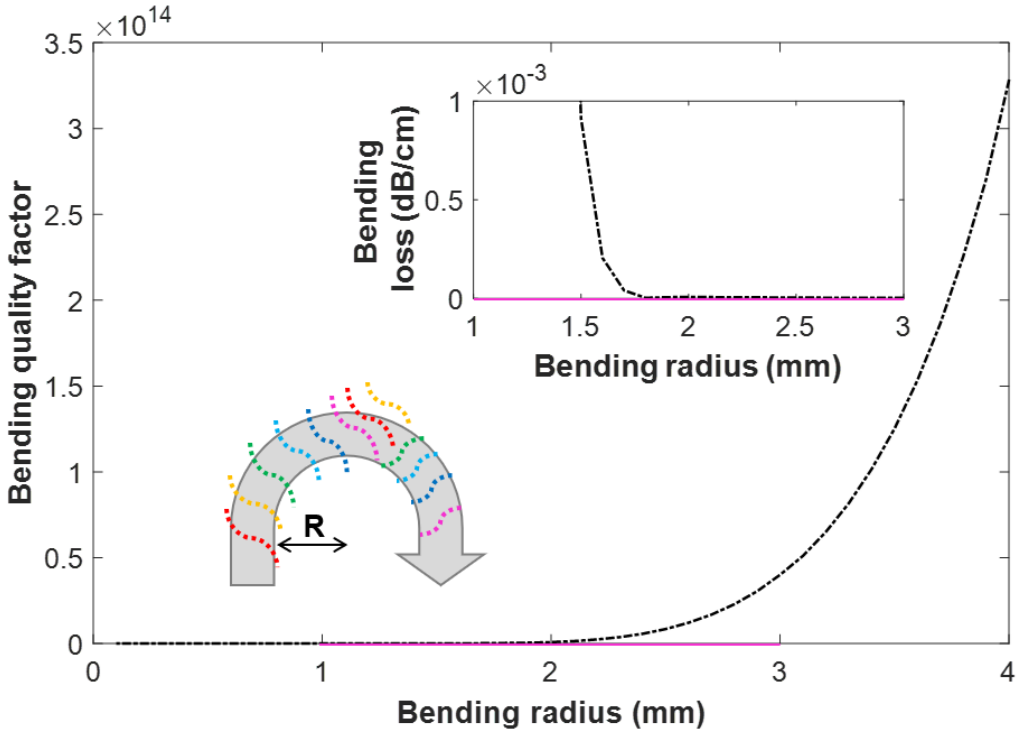


**Figure 2.3.** Bending quality factor with inset bending loss for the fundamental TE mode at 1550 nm calculated for the $Al_2O_3$ ridge waveguide with 1.0, 0.25, and 2.2 μm thickness, etch depth and waveguide width, respectively, and a diagram representing light lost at the bend of a waveguide.

All of the mentioned waveguide parameters and properties need to be considered and accounted for when developing a waveguide platform and designing PICs. In many instances factors that are application specific will constrain the design, such as requiring TM polarization or a particular pump wavelength which also needs to be single mode. The first decision made is always the material platform, which has unique core and cladding refractive indices and modal properties that will need to be designed for using the above methods each time, for each application. The next section will introduce the integrated optical materials of interest for this thesis, including silicon, silicon nitride and two rare-earth hosts that are Si compatible.

## 2.2 Waveguide Materials

### 2.2.1 Silicon Compatible Waveguide Materials

#### 2.2.1.1 Silicon

Crystalline silicon has enabled the information age by providing a platform for microelectronics and integrated circuits which has become a staple of modern society. The atomic abundance of silicon on earth is second to oxygen, and both elements have their most prevalent source from the earth's solid crust, in the form of $SiO_2$ or silica of varying purity and species. This has enabled and encouraged vast resources to be poured into the fabrication of pure silicon crystal boules (cylinders), which after slicing, and polishing can be used as a semiconductor platform for a wide variety of applications such as photovoltaics, and microelectronics, which have shaped the modern world we live in today allowing inventions such as the computer and the smart phone. The industry refers to the platform as complimentary-metal-oxide-semiconductor (CMOS) which describes the integration between materials such as: metal for electrical connections and control of dopants for transistor gates, and other devices, oxide materials such as $SiO_2$ for electrical insulation and protective or spacing layers, and semiconductors namely Si which can act as a host for dopants and charge carriers allowing manipulation of electrical capabilities and more recently, optical properties. This platform, with years of funding and development from industry due to the success of silicon microelectronics, is now being applied to address the capacity issues facing the information age as a waveguide material for photonic integrated circuit technology [6,7]. Using the plasma dispersion effect, Si waveguides can be electrically contacted in order to modulate signals providing high-speed, low-cost and low energy switches for telecommunications, as well as a variety of other devices [8,9].

Silicon has a transmission window which is restricted from 1.1 to approximately 10 μm without additional material losses, and a relatively high refractive index of ~3.4 making it an excellent material for NIR photonic applications for telecommunications in the O and S–L-bands as well as for MIR applications [10]. A high index contrast with surrounding media such as $SiO_2$ (n = 1.45) allows for the creation of compact devices and small bending radii for waveguide structures etched into the surface of Si films. The wavelengths of choice for communications around 1.3 and 1.55 μm align well with the transmission window of Si, as well. The mentioned reasons have supported Si as becoming the well accepted cornerstone material for PICs, resulting in an active field referred to as silicon photonics [11,12]. The substrate of choice for silicon photonics is referred to as silicon-on-insulator (SOI), which consists of a wafer diced silicon handle layer for physical substrate, and a thermally grown $SiO_2$ layer for optical substrate. This demonstrates the combination of the electrical capabilities from the CMOS world and the photonic developments of Si as an optical material which can support waveguide modes and allow propagation and manipulation of signals on-chip [13].

The mode shown in Fig. 2.1 a) for a Si waveguide shows high confinement in the core and a small modal area which enables tight bends for compact devices such as ring resonators. Implementing functionalities such as electrical contacts for detectors, manipulation of optical signals for modulation or sweeping of doped carriers is what excites industry about Si as a PIC platform. It however has limitations in regard to transmission in the visible regime, and inability to emit light via doping of optically active materials. Another slight drawback of the SOI platform, especially when it comes to considerations for rare-earth integration and operation with a laser, is the optical loss

(typically ~1–3 dB/cm at 1550 nm) caused by high refractive index contrast at the core-cladding interface and thus increased scattering losses [14,15]. Its inability to operate in the visible and short near-infrared spectra also limits its use in many applications of interest. For example, certain rare-earth elements are pumped at wavelengths < 1.1 µm, including for example $Yb^{3+}$ with ~975 nm pumping. In addition, visible wavelength devices are of interest for applications including biological sensing and environmental monitoring. Therefore, other materials should also be considered for waveguide platforms which can operate as rare-earth integrated active devices and sensors.

In this thesis, SOI waveguides were fabricated using the AMF MPW run as part of the SiEPIC workshop. Foundry processes are available through an increasing amount of sources each year, as SOI waveguides become a more worthwhile economic venture for the dedicated run-time they require.

#### 2.2.1.2 Silicon Nitride

Amorphous $Si_3N_4$ has been used extensively as a gate dielectric material inside of transistors, a coating allowing for anti-reflective surfaces or lenses, a mask layer aiding in the fabrication of printed circuit boards, and a variety of other optical and electrical applications [16]. More recently, it has demonstrated its capabilities as a waveguide material offering advantages over Si when it comes to availability for visible transmission and decreased propagation losses [17]. It however suffers from larger device footprints compared to Si and does not offer optoelectronic functionality, which limits its applications. Its availability for foundry fabrication is not as prevalent as Si, but its compatibility when it comes to CMOS fabrication is beginning to be accepted by leading foundries such as LIONIX who have demonstrated a variety of waveguide platforms with the material [18] capable of mass production.

The refractive index of stoichiometric $Si_3N_4$ is ~2.0, or ~1.7–2.1 when varied in between nitride and silicon rich films of $Si_xN_y$ compositions [19]. Also, silicon oxynitride films have been investigated as a candidate waveguide platform with tunable refractive indices available from ~1.46–2.0 [20]. The relatively lower refractive index of $Si_3N_4$ when compared to Si leads to wider single mode waveguides. This allows for relaxed fabrication tolerances and waveguide widths > ~1 μm when operating at telecommunication wavelengths around 1550 nm. This enables a versatility in fabrication methods to be used for $Si_3N_4$ waveguides, e.g., including lower resolution methods such as contact UV lithography. The decreased index contrast of $Si_3N_4$ with surrounding cladding materials such as $SiO_2$ also leads to a lower imparted scattering loss due to sidewall roughness, which manifests itself in the lower propagation losses demonstrated on the $Si_3N_4$ platform [21], even down to < 1 dB/m [22].The mode profile as well as effective index, and modal overlap and area can be calculated in a similar manner to the $Al_2O_3$ platform shown in Fig. 2.2 of 2.1.2 but for a strip $Si_3N_4$ waveguide to discern the single mode width. The effective indices are shown in Fig. 2.4 for a 200 nm thick $Si_3N_4$ strip waveguide at 1550 nm, with a TE single mode cut-off of approximately 1.2 μm with a $SiO_2$ surrounding, similar to the mode shown in Fig. 2.1 b) in 2.1.1. The platform has relaxed fabrication tolerances well within the limits of masked UV lithography, and even optical direct write technology.

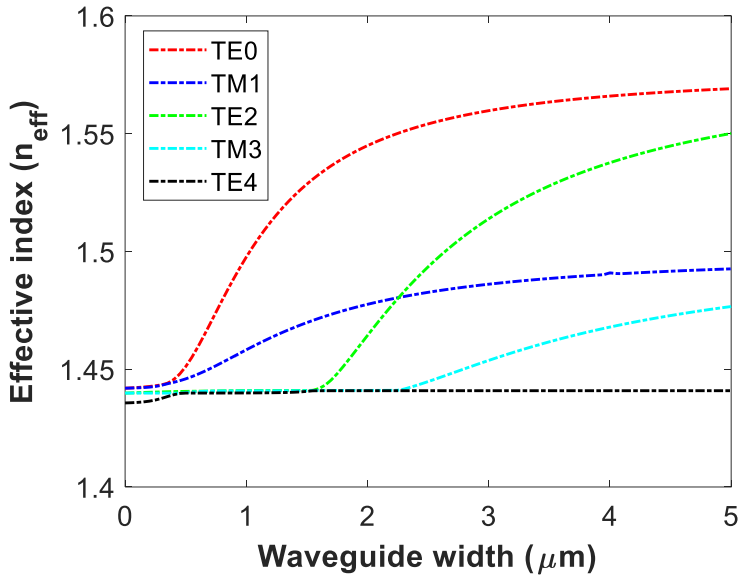


**Figure 2.4.** Effective indices for a 200 nm thick $Si_3N_4$ strip waveguide at 1550 nm with $SiO_2$ cladding.

The deposition of $Si_3N_4$ has been realized via LPCVD, HD-PECVD and ECR-PECVD which each offers their own advantages in terms of stoichiometry, hydrogen incorporation, stress, and fabrication versatility when it comes to temperature, pressure and combination with different materials. Optical loss due to hydrogen incorporation, especially for the telecommunication wavelengths around 1.5 µm from optical absorption of Si-H and N-H bonds is a prime concern [23]. This is the case for the ECR-PECVD $Si_xN_y$ films investigated in this thesis, which however remain an attractive technique due to the lower deposition pressures and temperatures as additional energy from the plasma aids in ionization of gas species and film deposition [24]. In contrast, LPCVD dominates currently as the large-scale foundry deposition technique of $Si_3N_4$ due to its lower hydrogen incorporation and lower material absorption and scattering losses [25].

The low optical losses offered by $Si_3N_4$ make it an attractive material for the development of PIC devices, such as passive interferometers, resonators for filter, arrays

for LIDAR, or non-linear optical processes [26,27]. On-chip active devices such as lasers or optical amplifiers also are possible with the low losses provided by $Si_3N_4$ waveguides when combined or coupled to rare-earth compatible materials [28–30]. The lower index compared to Si also allows for an increased evanescent mode interaction making it easier to design waveguide structures with higher overlap in upper claddings which have been hybridized for gain or sensing. $Si_3N_4$ be integrated on the SOI platform alongside Si [31], or it can also be a standalone platform and fill the gaps and address application spaces Si cannot.

In this thesis a film recipe for ECR-PECVD $SiO_xN_y:H_z$ is developed for optical waveguides, and silicon valley microelectronics (SVM) 200 nm thick $Si_3N_4$ was used for prototyping waveguides with UV mask writing and reactive-ion etching. LIONIX is an emerging leader for foundry scale production of $Si_3N_4$, which has been utilized in closely related works to realize low-loss platforms and optical amplifiers when hybridized with back-end deposited $TeO_2$ [32,33].

### 2.2.2 Rare-Earth Hosts

#### 2.2.2.1 Aluminium Oxide

Amorphous $Al_2O_3$ demonstrates optical capabilities required for waveguides like low-optical loss, and compatibility with standard processing techniques like lithography. It also has a broad transmission spectrum across the visible and O–L telecommunication bands making it an encouraging candidate for applications in the integrated photonics domain. More important in context for this thesis, are its capabilities to host rare-earth elements and act as a waveguide platform capable of optical amplification [34–36] and lasing with elements such as Er and Yb [37,38]. The elemental abundance of Al and relatively low

cost of pure targets for fabrication methods such as thin film sputtering are also beneficial from an economics perspective.

The refractive index of $Al_2O_3$ is ~1.6 which is relatively lower than other waveguide materials mentioned in this thesis. This causes typical $Al_2O_3$ waveguides have widths around or above 2 μm for single mode operation as shown in Fig 2.2 c). Fabricating of $Al_2O_3$ waveguides has been carried out several ways, mainly being dominated by thin film deposition, by reactive sputtering, or atomic layer deposition (ALD) [39] techniques, and contact lithography and ion-beam or reactive ion etching for patterning [40]. Although it can produce pure, high quality and smooth $Al_2O_3$ films, ALD has a slow deposition rate and isn't as accessible to the CMOS pilot line as sputtering. Additionally, the in-situ doping of $Al_2O_3$ can be carried out while sputtering using purity controlled solid targets, allowing for the incorporation of rare-earth ions such as $Er^{3+}$ or $Yb^{3+}$ during deposition [41] without metalorganic precursors [42,43]. Etching $Al_2O_3$ waveguides can be performed via dry methods such as RIE using gases such as chlorine, or wet chemical methods such as acid immersion with acids like $H_3PO_4$ [44]. Aluminum is also a familiar material to the CMOS pilot line, which allows convenient supply for foundries willing to adopt $Al_2O_3$ technology. For these reasons, $Al_2O_3$ has been chosen as a topic of study for the realization of on-chip optical amplifiers and lasers for the PIC infrastructure, as the field is in need of an on-chip gain medium which is compatible with mass production and provides stable, efficient and powerful amplification and emission on a Si chip.

#### 2.2.2.2 Tellurium Dioxide

Tellurium dioxide is a more exotic and less widely used optical material in comparison to the other oxides such as $SiO_2$ and $Al_2O_3$. Used primarily for its rewritable characteristics in compact discs (CDs) and digital video discs (DVDs), it also possesses a relatively high

refractive index for an oxide glass material (2.0) which has peaked interest in its research towards becoming a waveguide platform [45]. It also has a high solubility for lanthanides and is therefore a viable host for rare-earth elements [46]. The material is more sensitive to variations in terms of phases changes and breaking down due to its lower chemical and thermal stability is in comparison to $Al_2O_3$. This chemical instability causes it to struggle with traditional patterning methods and lithography techniques using clean-room chemicals such as developer. For this reason, its realization as a waveguide platform has been limited, but still has been demonstrated using $H_2$ plasma etching techniques and a bottom anti-reflection coating (BARC) for protection to realize waveguides with losses as low as 0.1 dB/cm at 1550 nm [45]. Alternatively, back-end deposition lends itself as a useful technique for sputtering $TeO_2$ onto waveguide platforms, which avoids the necessity to pattern the $TeO_2$ layer. Hybridizing the structure in this manner also allows for the overlap of the optical mode to be shared between a predefined structure and a post deposited film, similar to having optical overlap in part of the top cladding. Using magnetron reactive sputtering hybridizing waveguides with this technique has provided low-loss waveguide platforms for two waveguide core materials. $Si_3N_4$ waveguides received from foundry have been hybridized with $TeO_2$:$Er^{3+}$ to show low-loss waveguides and [33] optical amplifiers. Si disk resonators coated in $TeO_2$:$Tm^{3+}$ have demonstrated lasing at ~1.9 μm when coated on foundry received waveguides [47]. Both of these waveguide platforms are accessible from foundry and can be hybridized using back-end deposition which changes their optical mode properties and can be designed for in a similar manner to those shown in Fig. 2.2.

Waveguide properties for a Si and $Si_3N_4$ strip structure coated with $TeO_2$ are shown in Fig. 2.5 including the design cross section in a), the mode profiles in b)–c), effective indices in d)–e), and material overlap with inset modal area for fundamental TE operation in e)–f). Here a hybridized waveguide structure is shown with the capabilities of both materials available for exploitation, including rare-earth solubility and non-linear characteristics of the $TeO_2$ and low-loss patternable CMOS compatible Si and $Si_3N_4$ technology.

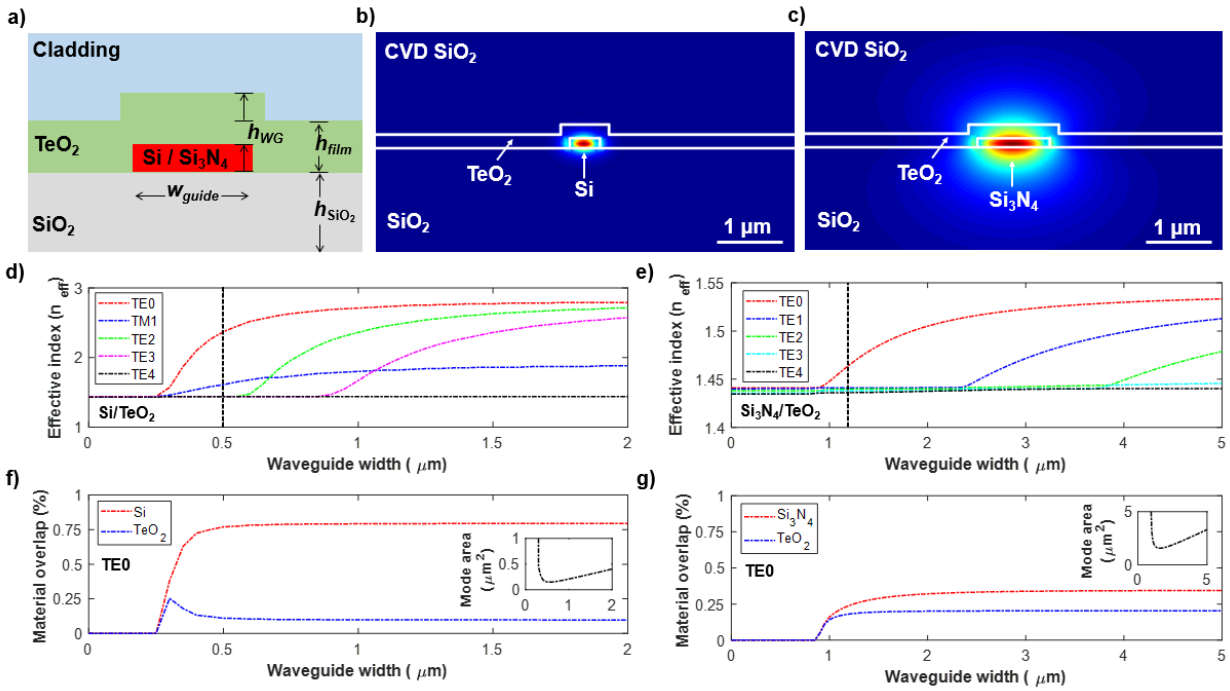


**Figure 2.5.** a) Design cross section and b) Si and c) $Si_3N_4$ waveguide fundamental TE mode profiles at 1550 nm with 300 nm $TeO_2$ coating and waveguide thicknesses of 0.22 and 0.2 μm and widths of 0.5 and 1.2 μm respectively. Optical parameters from the designs including d)–e) effective indices and f)–g) material overlap with inset modal areas.

As shown, the fabrication constraints, such as single-mode width and feature requirements become limited by the waveguide dimensions, not the deposited $TeO_2$

layer. Film heights of 300 nm were used for calculations shown in Fig. 2.5, however optimization on fine tuning of the layer thickness to 'pull' more mode into the top layer can be done. This also includes changes to the $Si_3N_4$ layer, such as using a 100 nm waveguide thickness. Back-end deposition is a reliable method for hybridizing rare-earth doped $TeO_2$ on waveguide platforms, which can be doped in-situ during deposition using magnetron sputtering. The film deposition process can be performed without substrate heating as well, which is an advantage when dealing with thermally sensitive materials.

Table 2.2 is included to summarize the waveguide material platforms discussed, including their most notable features for design, operation, fabrication and application advantages. It should be noted entries in the table are relevant to those used in this thesis and can have values and techniques ranging from those presented here.

**Table 2.2.** Waveguide material platform summary

| **Waveguide material** | **Film fabrication technique** | **Waveguide patterning technique** | **Refractive index** | **Minimum wavelength (μm)** | **Single mode loss at 1.55 μm (dB/cm)** | **Single mode width (μm)** | **Capabilities and application advantages** |
|---|---|---|---|---|---|---|---|
| Silicon [7–10,14,15] | SmartCut | DUV lithography | 3.47 | 1.1 | 2.0 | ~0.5 | Optoelectronic integration, compact bends |
| Silicon nitride [21,22] | CVD | Contact lithography | 2.00 | 0.3 | 0.001 | ~1.5 | Visible transmission, very low-loss |
| Aluminium oxide [34–36] | PVD | Contact lithography | 1.61 | 0.3 | 0.2 | ~2.2 | Rare-earth doping, readily patternable |
| Tellurium dioxide [45,46,48] | PVD | Back-end deposited, no patterning | 2.08 | 0.3 | 0.1 | N/A | Rare-earth doping, high nonlinearity |

## 2.3 Passive Devices

### 2.3.1 Sagnac Loop Interferometers

First implemented in interferometry experiments intended to measure the drag caused by the earth moving through the aether by Georges Sagnac in 1913 [49], the Sagnac effect describes the phenomena observed when light is split, and its counter propagating beams travel down the same path but in opposite directions and interfere with each other after exiting [50]. This leads to interference fringes due to an inherent phase difference in the two counterpropagating optical fields after traversing the path. Referred to as 'common-arm interferometers' discovered as an arrangement of the Michelson interferometer by Michelson himself in 1886, these are now employed in applications such as optical gyroscopes which can measure fine changes in angular rotation [51] and lasers by providing loop mirrors [52]. In the domain of PIC technology and waveguide structures, they can be understood as a directional coupler with a 50/50 splitting ratio which sends two optical modes down the same path formed in a continuous loop. This loop leads the waveguide modes back to the directional coupler, which causes interference and a phase delay, referred to as the Sagnac effect. A diagram of a Sagnac loop employed in a waveguide structure is shown in Fig. 2.6 as well as the direction of optical paths indicated by arrows.

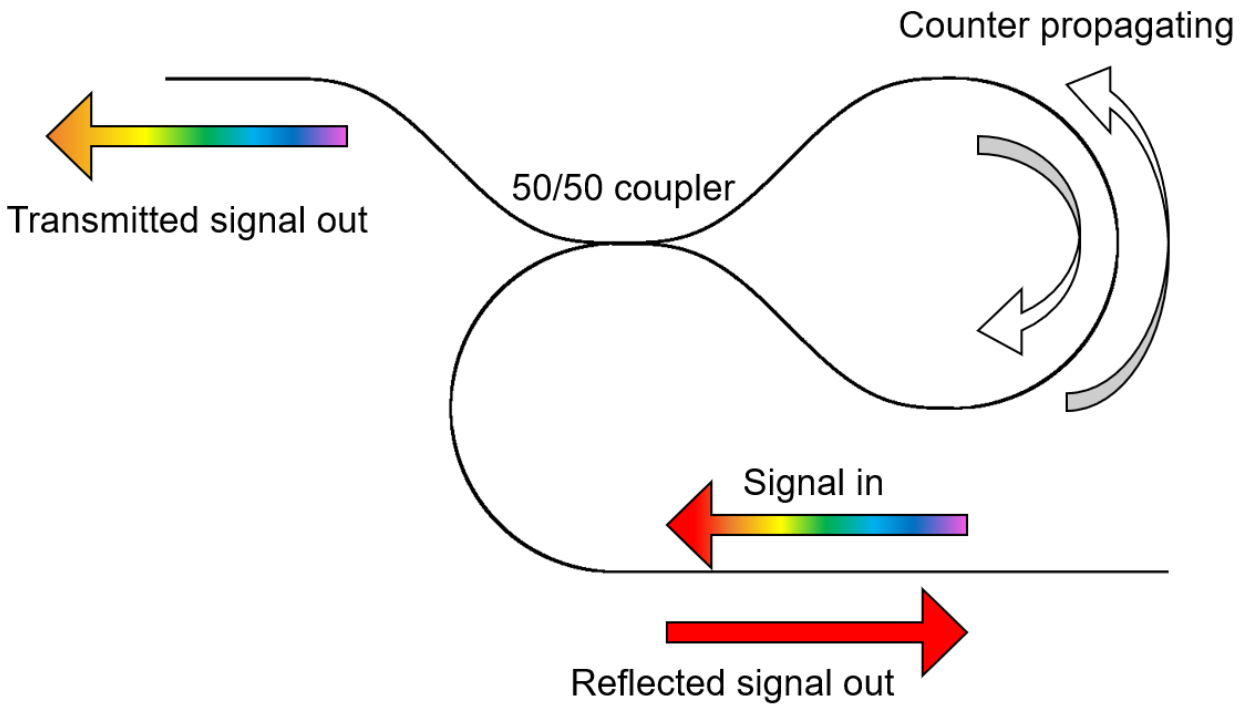


**Figure 2.6.** Diagram of a Sagnac loop interferometer with labelled signals and their optical paths, as well as 50/50 coupler comprised of adjacent waveguides spaced by a coupling gap.

Designing a waveguide Sagnac loop requires two important components, a loop and a 50/50 coupler. The loop simply can constitute a semi-circle as shown in Fig. 2.6 with an appropriate bending radius and waveguide dimensions for single mode operation determined by the material platform. Two waveguides adjacent to one another share what is referred to as a 'supermode' and their analysis can be used to demonstrate the phase difference between the two optical paths. Figure 2.7 below demonstrates the contour field intensity plots for a $Si_3N_4$ directional coupler clad with $SiO_2$. Two modes are shown, the first of which is a shared supermode, and the second represents the two counterpropagating modes by plotting the phase of the solution. As shown, the respective modes in either waveguide are purely out-of-phase leading to deconstructive interference,

and if split evenly in the coupler, complete cancelling and reflection of the incoming optical field is achieved.

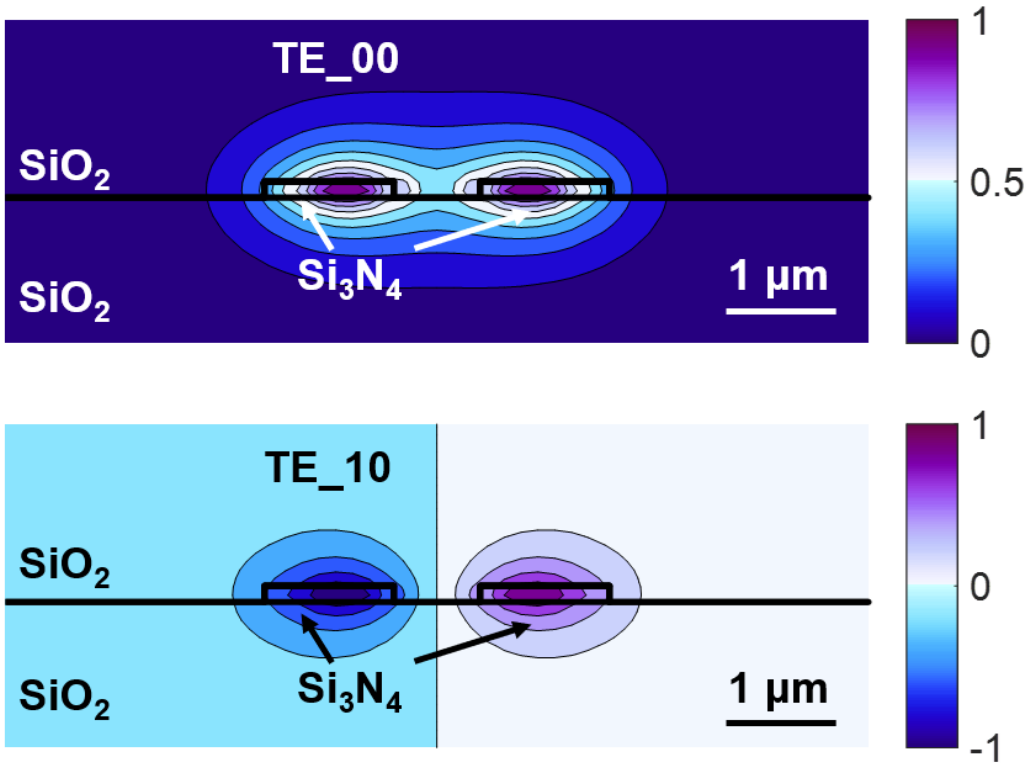


**Figure 2.7.** Supermode analysis for $Si_3N_4$ waveguides with a height, width, and gap of 0.2, 1.2, and 0.8 μm respectively, showing fundamental TE mode intensity and phase at 1550 nm.

After solving the modal properties for a particular gap, the effective indices can be used to determine the coupling length ($L$) required for the optical power to transfer from one guide to another using the following equations:

$$L_x = \frac{\lambda}{2\Delta n_{eff}}, \tag{4}$$

$$\kappa = sin\left(\frac{\pi L}{2L_x}\right). \tag{5}$$

This 'cross-over length' ($L_x$) can be used to determine the 50/50 splitting length as well by setting the square of the coupling constant to 0.5 ($\kappa^2$= 0.5), which aids in designing the

directional coupler used for the Sagnac loop. Details on the mathematical formulation and simulation of directional couplers can be found in [53]. By including Sagnac loops with safe bending radii and a variation in coupling lengths around the 50/50 splitting ratio in a prototyping demonstration, pathways towards optimizing the design to behave as a mirror for a laser resonator can be found. This is demonstrated using UV mask writing in Chapter 4 on the $Si_3N_4$ platform.

### 2.3.2 Ring Resonators

A waveguide in which the optical path repeats its travel around a continuous circuit is referred to as a ring resonator. The build-up of light via total internal reflection and constructive interference leads to the storage of an optical field which resonates inside the loop, ring, disk or other structure. This structure is coupled to a waveguide, called the bus waveguide which transfers power to the resonator through close proximity. Features such as the dimensions of the ring and distance from the coupling waveguide determine the wavelengths that are allowed to resonate, the power and phase of optical energy that can transfer over, and the modal properties of the ring waveguide itself. By controlling these parameters, rings can be used as resonator cavities for lasers, wavelength filters, modulators, and many other different devices.

Designing a ring resonator requires an understanding of the waveguide platform's bending capabilities, as well as the approximate gap required to allow coupling between two adjacent waveguides. When deciding features for a fabrication run it is imperative to include variations close to your desired design due to manufacturing tolerances and changes in features and dimensions across wafer location and process runs. This is particularly important for the design of ring resonators. Features such as the coupling gap are recommended for most variations, as it is common to experimentally confirm the

regimes for under, over, and critically coupled rings, which is determined by the ring loss and coupling condition between the bus and ring waveguide. Details on the mathematical formulation for the transmission can be found in [53]. For the purposes of this thesis discussion will be focused on the different ring design strategies relevant for the development of optically active devices and sensors.

The intrinsic quality factor of a ring is inversely proportional to the optical loss of the resonator, which is useful for determining the waveguide propagation losses when developing different material platforms. To ensure the resonance can be used for accurate conversion to waveguide loss ($\alpha_{WG}$) using:

$$\alpha_{WG} = \frac{2\pi n_{group} \times 4.34}{\lambda Q_{intrinsic}}, \tag{6}$$

and:

$$n_{group} = n_{eff} + \lambda \frac{dn_{eff}}{d\lambda}, \tag{7}$$

the $Q_{intrinsic}$ which is dependent on waveguide propagation losses needs to be used, not the $Q_{external}$ which is dependent on bus and ring coupling losses. The simple quality factor formula which is dependent on the wavelength, and width of the resonance using:

$$Q_{FWHM} = \frac{\lambda}{\Delta\lambda}, \tag{8}$$

can be more accurately cast into:

$$Q_{intrinsic} = \frac{2\pi n_g log_{10}(e)}{\lambda_0 \alpha_{WG}}, \tag{9}$$

and,

$$Q_{external} = \frac{2\pi c}{\lambda_0 \kappa}, \tag{10}$$

which together yield the loaded quality factor:

$$\frac{1}{Q_{loaded}} = \frac{1}{Q_{intrinsic}} + \frac{1}{Q_{external}}. \quad (11)$$

Experimentally, the transmitted optical power vs. wavelength of a ring resonator can be measured and peak fitting algorithms in MATLAB can be used in order to calculate the quality factors [53]. Depending on the gap of the ring, the coupling condition is referred to as either overcoupled ($Q_{external} < Q_{intrinsic}$), undercoupled ($Q_{external} > Q_{intrinsic}$), or critically coupled ($Q_{external} \approx Q_{intrinsic}$) which needs to be carefully considered when assigning the intrinsic and external quality factors for waveguide loss and coupling strength estimation, respectively. Measuring the resonance at different wavelengths, and for different coupling gaps reveals this by comparing the extinction ratio (ER) in each measurement. Deep resonances are indicative of critical coupling, whereas undercoupled rings will demonstrate higher $Q_{loaded}$ and overcoupled rings will demonstrate lower $Q_{loaded}$. It is recommended to measure a variety of ring gaps, but to focus on those with undercoupled conditions and high $Q_{internal}$ to receive an accurate waveguide loss estimation. Figure 2.8 demonstrates experimental results obtained from $Al_2O_3$ ring resonators with a film height of 1.0 μm, 0.25 μm etch depth and 2.0 μm waveguide width and gaps of 2.0 and 2.5 μm, which represents near critically- and under-coupled resonances, respectively.

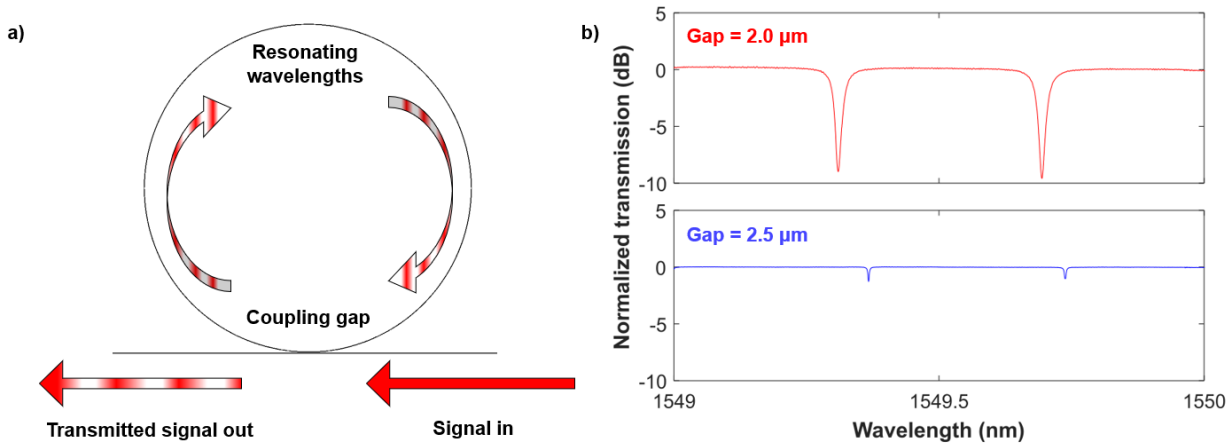


**Figure 2.8.** a) Diagram of a ring resonator with indicated optical path lengths, and b) measured transmission of critically and undercoupled ring resonators with 2.0 and 2.5 μm gaps showing deep shallow extinction ratios, respectively.

### 2.3.3 Distributed Bragg Reflectors

Interaction between an optical medium that has periodic perturbations on the scale of incoming radiation that leads to spectrally selective interference, is an example of diffraction. This interference in a waveguide can cause reflection, and when multiple are coupled together a resonance is created, which can lead to wavelength dependent mirrors and laser cavities [54,55]. These perturbations can be defined physically in the sidewalls of waveguides as grooves or width modifications [56], pieces adjacent to the waveguide [57,58], or as index modifications in the waveguide or top cladding layer [59]. Diffraction gratings are also used to couple light to the chip, using a unique ‘fan’ shape with periodic structuring to preferentially diffract light in or out of the waveguide. Optical modes preferentially reflect and based on the periodicity of the refractive index changes in the optical path length, interfere with each other at particular wavelengths. This in affect

makes an optical stop band in which certain frequencies or wavelengths are not allowed to propagate due to interference inside the grating.

To form a resonator out of the grating, the center of the grating (longitudinally along the propagation direction) can be modified with a single repeated grating unit leading to a phase change and a particular kind of distributed feedback cavity (DFB) [60]. Alternatively, placing two gratings sequentially in the same optical path length separated by a waveguide in the middle, is known as a distributed Bragg reflector cavity (DBR) [54]. The frequency, or period of the perturbations in each grating governs the wavelength of operation, as also decided by the effective index of the mode which can be calculated using effective medium theory (EMT) [4]. The central wavelength is governed by:

$$\lambda = 2\Lambda n_{eff}, \tag{12}$$

which determines the periodicity (Λ) of the grating index modulations. By designing properties such as the grating piece width and gap, the effective index change can reveal key parameters such as the length of a grating required to achieve a set percentage reflection. This is governed by a coupling constant ($\kappa$) and a subsequent calculation on the percentage of reflectivity ($R$) for a given length ($L$):

$$\kappa = \frac{2\Delta n_{eff}}{\lambda}, \tag{13}$$

$$R = tanh^2(\kappa L). \tag{14}$$

When designing DBR cavities for lasers, it is desirable to have strong reflection (99.9 %) on each end, with slightly lower percentages to out-couple the laser power (80.0–90.0 %) on one end. When designing DBR cavities for sensors, it is desirable to have a large amount of optical overlap with the surface of the devices in order to increase sensitivity. In the context of this thesis, this represents a balance which needs to be maintained in

order to realize integrated laser-based sensors. To demonstrate the working design of a waveguide DBR structure, an Si sidewall grating spectrum with air cladding is shown in Fig. 2.9, with insets of the intra-band resonances and a diagram of the cavity structure showing the different sections and directions of signal propagation. The lengths and periods were determined by calculating ~99% reflectivity at 1550 nm, and the sidewall corrugation size was selected to produce a $\Delta n_{\text{eff}}$ large enough to ensure moderately sized devices. The fabrication was carried out using SiEPIC's IME MPW fabrication run. The study of these devices and their hybridization with $TeO_2$ and PMMA for biological sensing are the subjects of Chapter 6.

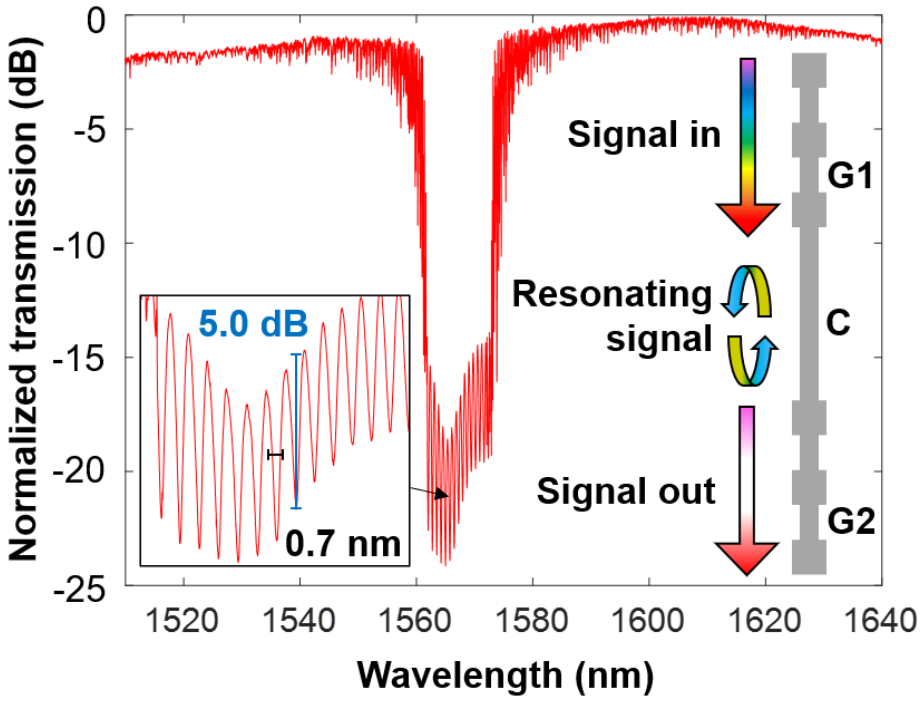


**Figure 2.9.** Measured transmission spectrum for a 500 x 220 nm Si strip air cladded waveguide, with sidewall grating corrugations with a width and period of 60 and 326 nm respectively, and gratings and cavity lengths of 0.5 and 1.2 mm, respectively. Insets: close-up view of resonances at 1565 nm and a diagram showing the DBR cavity structure, with labelled grating 1 (G1) typically being stronger than grating 2 (G2) for the cavity (C) to obtain directional output.

## 2.4 Active Devices

### 2.4.1 Erbium-Ytterbium Co-Doped Integrated Optical Amplifiers

Similar to how electrical signals need to be amplified for specific applications, optical signals benefit greatly from increased powers provided by on-chip elements. In an optical amplifier, an optical signal passes through and is amplified via stimulated emission in a gain medium. A gain medium is also one of the key elements of a laser. However, unlike a laser there is no feedback provided by an optical cavity leading to a lasing mode in an amplifier. This leads to a device in which an optical mode gains more power as it propagates as long as it is being supplied with sufficient pumping energy in order to

overcome signal losses. The Erbium-doped fiber amplifier (EDFA) invented in 1987 is an example of a commercial rare-earth optical amplifier which, supports the telecommunication network our world relies on today [61]. Optical amplifiers can be realized in a variety of materials which can convert atomic excitation to optical energy, which are referred to as gain media. For the case of semiconductor optical amplifiers (SOAs) optical amplification involves the recombination of electrons and holes [62,63], Raman amplification the scattering between an incoming photon and material lattice phonons [64–66], and in doped or bulk systems the excitation of an atomic energy state and coherent decay with surrounding optical radiation [67,68], all of which have experimentally demonstrated gain and lasing. These stimulated emission processes have been explored on various materials in the photonic integrated circuits, each with limitations when it comes to being realized on the SOI platform [69,70]. Rare-earth doped optical amplifiers have been shown to provide high power, with efficient and stable outputs and can be fabricated on a large scale via dopants in thin-films. They however require optical pumping and materials other than Si to host them which is a roadblock in their realization as an industry standard for optical amplifiers in integrated photonics. Integrating these rare-earth ions in a host which is compatible with the SOI platform as a thin-film is a challenge addressed by this thesis, and builds on other works which utilize oxide based materials which are structured into, or are coatings hybridized on waveguides.

When embedded in a matrix, the rare earth ions degeneracy is lifted, and Stark splitting leads to energy states available for electronic activity. In rare-earth ions generally, this electronic activity in the 4f shell is shielded from the surrounding matrix by the large 5s

shell, which gives each rare-earth ion a unique wavelength of operation regardless of the host material. Rare-earth elements such as erbium and ytterbium can be incorporated into fabrication processes such as magnetron sputtering for in-situ doping of amorphous oxides while they are being deposited. This process allows for deposition on foundry made waveguides as well which can be useful for research scale fabrication of optical amplifiers for the photonic integrated industry. To host the ions, materials like $Al_2O_3$:$Er^{3+}$:$Yb^{3+}$ can be fabricated via reactive sputtering which can utilize pure rare earth targets to dope the amorphous glass in-situ. Singly doped systems allow for straight forward pumping schemes with simpler energy transfer between the photons and rare-earth ions. Co-doping can be useful when transfer between two similar energy levels can complement each other in a pumping scheme, leading to energy transfer from one ion to another, and increase in a desired emission. In the case of $Er^{3+}$-$Yb^{3+}$ co-doped systems, the increased absorption cross section of pump wavelengths for $Yb^{3+}$ is hypothesized to lead to more 980 nm light being absorbed and converted into 1530 nm signal light in $Er^{3+}$ after resonantly coupling with excited $Yb^{3+}$ ions [71]. It has been demonstrated in $Al_2O_3$ waveguides, that doping with $Er^{3+}$ and $Yb^{3+}$ ions have been shown to provide optical amplification and net gain, which has been limited to on-chip [72]. However, implementing these amplifiers on $Al_2O_3$ which is also coupled to an SOI waveguide remains a research challenge and has been demonstrated with signal enhancement [73], and in $Si_3N_4$ which has been limited to on-chip gain [28] via multi-layer integration.

Optical amplifiers rely on stimulated emission, which occurs when an excited atomic state decays coherently, producing an in-phase photon with nearby propagating optical radiation. The Einstein coefficients were suggested in 1916 to aid in describing the

probability of absorption and emission of photons by an atom or molecule and introduces parameters such as absorption and emission cross sections [74,75]. These terms are useful in describing the fundamental optical processes at play in optical amplifiers such as absorption, and spontaneous and stimulated emission. The mathematical derivation is included in [76] which utilizes dipole treatment to describe the reaction to incoming optical radiation by an atomic system. These three fundamental optical processes are shown using the $Al_2O_3:Er^{3+}:Yb^{3+}$ matrix with 980 and 1550 nm pumping and signal wavelengths respectively in Fig. 2.10. A simple bulk layer is demonstrated, showing a small subset of possible interactions between optical radiation and the rare earth ions, including resonant transfer of power between excited ions demonstrated as a black arrow.

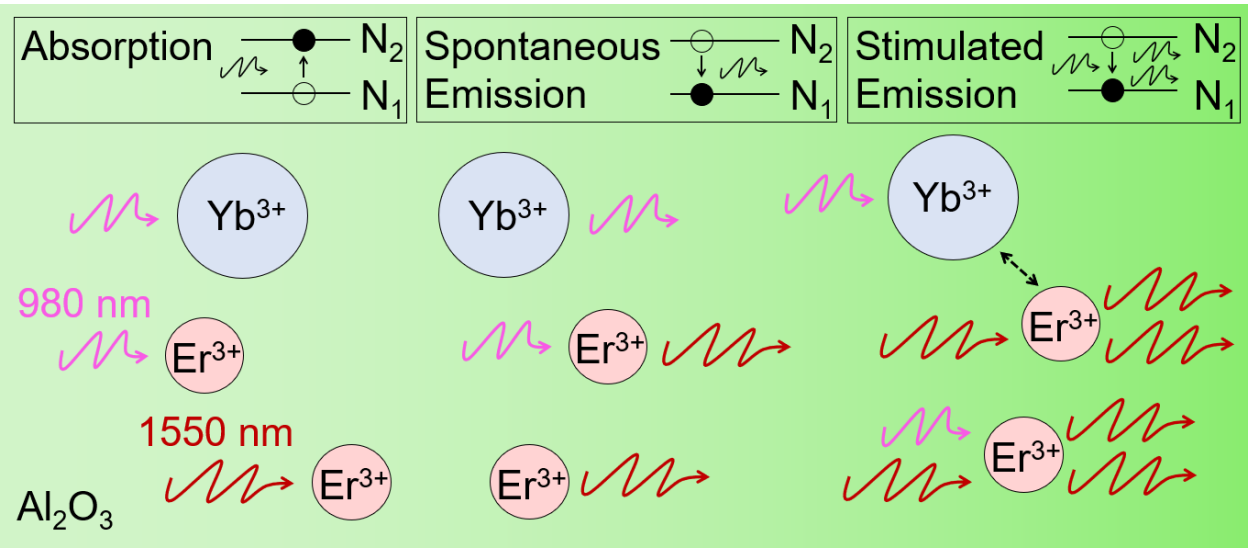


**Figure 2.10.** Fundamental optical processes depicted inside of bulk $Al_2O_3:Er^{3+}:Yb^{3+}$ with 980 and 1550 nm pump and signal photons, respectively. Resonant energy transfer between ions depicted as black dashed arrow.

When considering the change of population of electrons in discrete atomic energy states, mathematical generalization can be made for their pathways they can take to relax after being excited by an external energy source. These equations are referred to as rate

equations, which describe the various energy levels' populations in terms of one another ($N_x$), incoming flux of signal or pump photons ($\Phi_s$, $\Phi_p$), lifetimes in these various states ($\tau_x$), emission and absorption cross sections ($\sigma_{xy}$), energy transfer upconversion ($W_{xy}$) and $Yb^{3+}$-$Er^{3+}$ energy transfer ($C_{xy}$) [71,77]. These energetic pathways and rate equations are shown in Fig. 2.11, which are by no means an exhaustive example of the possible pathways for energy transfer in the given system. The example is given in context of the co-doping of $Er^{3+}$-$Yb^{3+}$ ions in $Al_2O_3$ which is a major focus of this thesis, and the optical amplification material demonstrated in Chapter 5.

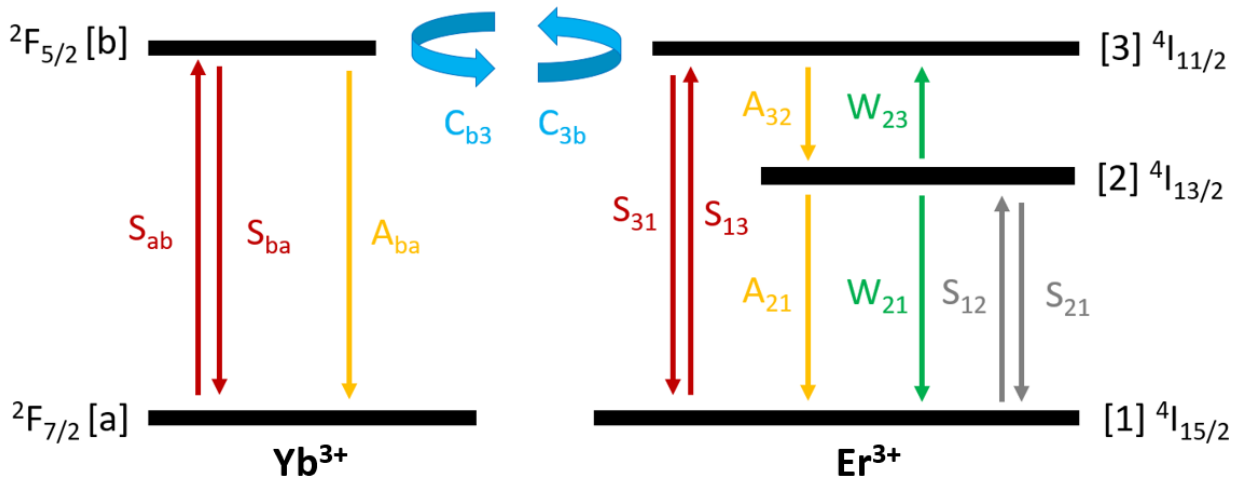


**Figure. 2.11.** Diagram of $Yb^{3+}$ and $Er^{3+}$ energy levels included in basic amplifier rate equation model with associated excitation and decay paths for various transitions available with $A_{ij}$, $S_{ij}$, $W_{ij}$, and $C_{ij}$ denoting spontaneous, stimulated, energy transfer upconversion, and $Yb^{3+}$-$Er^{3+}$ energy transfer coefficient respectively.

$$
\begin{aligned}
(1)\ \frac{dN_1}{dt} &= -N_1\cdot\sigma_{12}\cdot\Phi_s - N_1\cdot\sigma_{13}\cdot\Phi_p + N_2\cdot\sigma_{21}\cdot\Phi_s + N_3\cdot\sigma_{31}\cdot\Phi_p + N_{2^2}\cdot W_{11} + \frac{N_2}{\tau_{21}} \\
(2)\ \frac{dN_2}{dt} &= N_1\cdot\sigma_{12}\cdot\Phi_s - N_2\cdot\sigma_{21}\cdot\Phi_s - 2\cdot N_{2^2}\cdot W_{22} - \frac{N_2}{\tau_{21}} + \frac{N_3}{\tau_{32}} \\
(3)\ \frac{dN_3}{dt} &= N_1\cdot\sigma_{13}\cdot\Phi_p - N_3\cdot\sigma_{31}\cdot\Phi_p + N_{2^2}\cdot W_{11} - \frac{N_3}{\tau_{32}} + N_b\cdot C_{b3} - N_3\cdot C_{3b} \\
(4)\ \frac{dN_a}{dt} &= -N_a\cdot\sigma_{ab}\cdot\Phi_p + N_b\cdot\sigma_{ba}\cdot\Phi_p + \frac{N_b}{\tau_{ba}} \\
(5)\ \frac{dN_b}{dt} &= N_a\cdot\sigma_{ab}\cdot\Phi_p - N_b\cdot\sigma_{ba}\cdot\Phi_p - \frac{N_b}{\tau_{ba}} - N_b\cdot C_{b3} + N_3\cdot C_{3b}
\end{aligned}
\tag{2}
$$

Rate equation solvers using eigenmode solutions of optical modes in the waveguide can be used to estimate the gain achieved by a particular design given its material spectroscopic details. This process is carried out in [53] which details the steps necessary for calculating the gain based on rate equations similar to those shown above, but for a singly-doped $TeO_2$:$Er^{3+}$-coated $Si_3N_4$ hybrid waveguide. Once the population dynamics are solved for a time varying system shown above, gain is calculated based on the spatial propagation of a waveguide mode as it undergoes signal enhancement from pumping, and propagation losses. This is shown for a general 2 level system below, where population inversion ($N_2 > N_1$) achieved via pumping causes carriers to be promoted to higher energy levels, and in the case of the $^4I_{13/2}$ Er orbital, allows for stimulated emission at ~1550 nm to the $^4I_{15/2}$ orbital,

$$\frac{d\Phi}{dz} = (\sigma_{em}N_2 - \sigma_{abs}N_1)\Phi. \tag{3}$$

Converting the flux of photons to power after the simulation has evolved in the time and spatial domain, allows quantification of the power with and without pumping referred to as signal enhancement. This can be mathematically carried out with knowledge of the propagation losses, resulting in an either net increase or decrease in the photon flux. If the signal enhancement (SE) overcomes the losses (L) imparted by the rare-earths (RE)

and waveguide (WG), internal net gain (G) can be achieved. In measurement, this can be calculated using equations shown below, which needs to consider the additional power imparted by ASE to calculate the SE and gain respectively,

$$SE\ (\lambda, P) = 10log_{10}\left(\frac{P_{pumped}(\lambda, P) - P_{ASE}(P)}{P_{unpumped}(\lambda)}\right), \quad (4)$$

$$G\ (\lambda, P) = SE(\lambda, P) - L_{RE}(\lambda) - L_{WG}. \quad (5)$$

Subtraction of power imparted by ASE is carried out with the pump power on and signal laser off, or using lock-in amplification. Pumping is achieved using laser diodes while the signal of interest co-propagates through the waveguide. For the above example, a 974 nm laser diode would be coupled into the waveguide after being combined with the ~1550 nm signal using a wavelength division multiplexer off or on-chip. While scanning the signal wavelength, the pumping wavelength and power is kept constant. The pump power supplies the energetic excitation to the ions and enables the release of coherent optical radiation when population inversion is achieved. When the fiber-chip coupling, and system fiber losses are also overcome, net external gain can be achieved, which represents the ultimate goal of any optical amplifier useful in practice in a fiber-optic system. Efforts are required in the optimization of fiber-chip coupling as it currently is a limitation for market ready integrated rare-earth amplifiers and packaged devices, which was considered, but not optimized for in this thesis.

### 2.4.2 Lab-On-Chip Sensors

Known as ‘lab-on-chip’ sensors, micro devices which interact with analytes via electrical or photonic changes can be used to replace bulky laboratory equipment only accessible in controlled facilities. As demonstrated in the previous sections, the modal spread from the waveguide core to the surrounding materials offers unique advantages when it comes

to adding functionalities to PICs. Waveguide sensors operate by using this accessible modal field, as analytes of interest interact with the PICs surface. The sensing analyte can take the form of an attached molecule on the surface or a liquid as it flows on the top of the sample via microfluidic integration. Waveguide sensors are typically realized as refractive index sensors, which operate on the principles of evanescent coupling between the waveguide core and an analyte of interest [78], or Raman spectrometers, which rely on the vibrational properties of the analyte and optical absorption [79,80]. Raman sensing, dominated by $Si_3N_4$ due to its lower two-photon absorption (TPA), has been shown to be useful for fingerprinting biological species on chip [81]. Refractive index sensing is more straightforward and has been widely demonstrated in Si [5,82]. Changes to the refractive index of the top medium, and therefore the effective index of the mode are read by a shift in the transmission spectrum, which allows refractive index sensing to monitor chemical criteria such as concentration or species in real-time [78]. The shift in spectrum depends on the waveguide structure and device that the analyte coats, which can take the form of a ring or disk resonator [83], interferometer [84], Bragg grating [85], or many other structures all with traceable and predictable resonances. The wavelength shift can be calculated using:

$$\Delta\lambda = \Delta n_{eff} \frac{\lambda_0}{n_g}, \tag{6}$$

which is proportional to the change in effective index when the analyte of interest perturbs the waveguide mode. This shift dictates the sensitivity of the sensor which is an important figure of merit when quantifying a sensors' behaviour and is typically measured with water. This water on the surface of the waveguide changes the refractive index profile surrounding the waveguide mode giving a bulk sensitivity ($S_{bulk}$):

$$S_{bulk} = \frac{\Delta\lambda}{(n_{air} - n_{water})}. \quad (20)$$

For particle detection, the sensitivity can be expressed using the thickness of the particles adlayer, or by other means with varying concentrations measurements using:

$$S_{surface} = \frac{\Delta\lambda}{t_{adlayer}}. \quad (7)$$

This sensitivity can be increased by optimizing the change in effective index by raising the optical overlap between the waveguide mode and the sensing medium. Factors like increased overlap with the sensing analyte is a straightforward way to increase the sensitivity of refractive index-based sensing, which can be achieved via adjusting the waveguide structure such as using a thinner film [86] or a thinner strip waveguide [80,87,88].

A figure of merit which is more useful for comparing different waveguide sensor devices is the limit of detection (LoD) which gives the minimum change in RIU required to shift the resonator by one bandwidth. This is also commonly normalized by wavelength, which gives the intrinsic limit of detection (iLoD):

$$LoD = \frac{1}{QS} \quad (8)$$

$$iLoD = \frac{\lambda}{QS}. \quad (9)$$

The mathematical formulation for sensors and their optimization and trade-offs for various device structures on the SOI platform are outlined in [5] and [89]. It can be seen that the iLoD depends on the quality factor, which is device dependent, and benefits from low-loss waveguides and sharp resonance spectra. It is also evident from the equation for iLoD that a tradeoff exists when considering high overlap with the sensing analyte in hopes to increase sensitivity. A highly sensitive device typically has high analyte overlap,

which reduces the quality factor by increasing loss due to lossy liquids like water or blood which add optical absorption. Another strategy to decrease the iLoD rather than increasing sensitivity, is to increase the quality factor of the resonator in the sensor. To do so, the ultra-narrow emission linewidths provided by lasers can be used, which utilizes their high-quality factor spectral properties to trace fine changes in central wavelength, intensity, or other emission characteristics [90]. Different modalities other than refractive index sensing can also be explored with stimulated emission on a chip, such as secondary emitting sources from fluorescence [90], or scattering which leads to frequency shifts in the emission [91]. On-chip laser emission has been shown to lead to monitoring of microparticles [91], single virus detection [92], water sensing [93] for biological sensing and environmental monitoring, and protein detection in urine [38] in rare earth doped $Al_2O_3$ and $SiO_2$ resonators.

The development of optically active laser sensors on the CMOS PIC platform requires significant research in materials capable of stimulated emission and which can be integrated on Si, such as $Al_2O_3$ or $TeO_2$. Furthermore, it requires materials capable of biological interfacing between the analytes and the waveguides. For biological sensing, chemical processes such as physisorption and chemisorption take place, which dictate how particles or molecules like proteins interact with the surface of the device. For chemisorption, which includes the bonding and immobilization of particles on the surface, additional surface chemistry is required for proteins or viruses to preferentially react with the surface of the sensor as it is either submerged in a liquid or one flows over top of it via PDMS microfluidic integration [94]. Preparing a surface for attachment or interaction with species in this manner is referred to as functionalization. Surfaces can be coated in

reactive functional oxide rich groups capable of reactions with hydrocarbon rich biological substances either via chemical or plasma processes. Polymers are commonly used as coating materials, in particular PMMA, which demonstrates low optical loss, and a rich supply of oxide groups which can be activated with plasma treatment [95]. Integrating these active materials and polymers into the SOI platform in a hybrid manner for the realization of optically active sensors is the focus of Chapter 6. An isometric design view of the type of hybrid waveguide lab-on-chip sensor studied in this thesis is shown in Fig. 2.12, with labelled materials, overlaid optical mode and illustrated analyte particles. The propagation direction for the mode is shown, with oscillations extending into the top and bottom layers to illustrate the shared overlap. The waveguide design and mode shown below is for a Si/$TeO_2$ Bragg grating resonator coated in PMMA with similar characteristics from Fig. 2.9. Here it can be observed that from a design perspective there are many materials and properties which can be optimized depending on the required sensor performance and application.

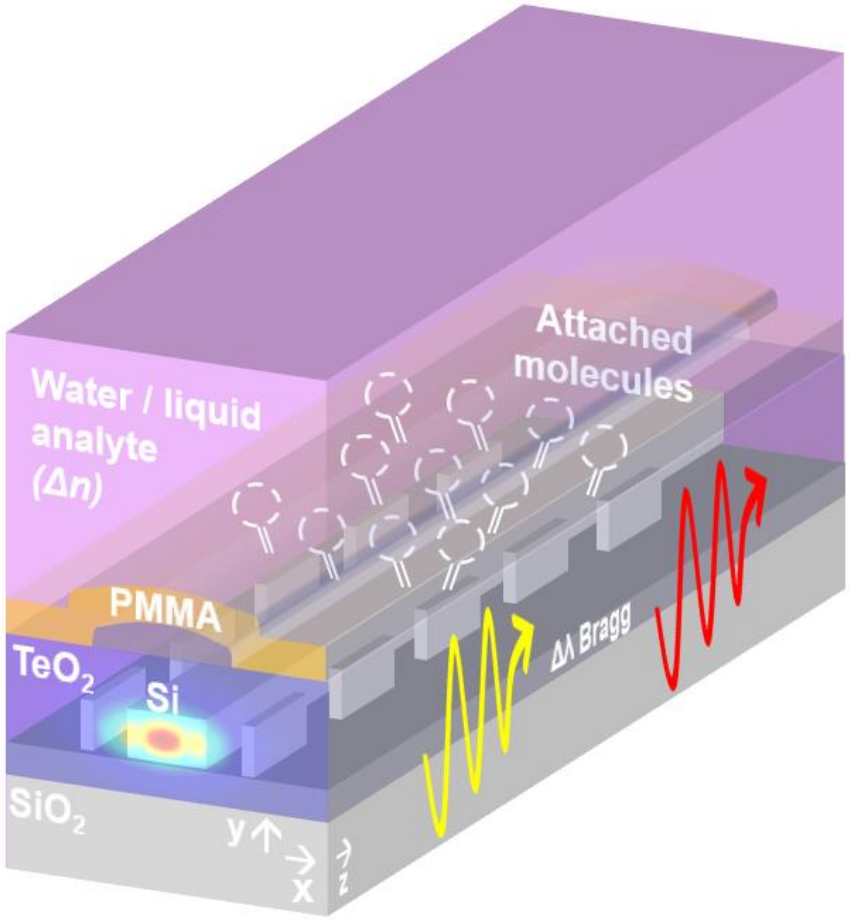


**Figure 2.12.** An isometric view of a Si/$TeO_2$ DBR waveguide sensor coated in PMMA with labelled materials and overlapped fundamental TE mode with illustrated attached molecules and optical propagation direction and Bragg shifted frequency indicated by coloured arrows for integrated biological sensing.

## 2.5 Conclusions

In conclusion, a variety of aspects of waveguides including the core and cladding materials and their optical properties, fabrication-limited dimensions, single-mode cutoff width, material and modal overlap, polarization, fiber and pump mode overlap, and minimum bending radius need to be considered for each waveguide platform when designing photonic devices. Si, $Si_3N_4$, $Al_2O_3$, and hybrid $TeO_2$ each pose their own unique advantages, limitations, and considerations for the realization of waveguide and PIC

platforms. Devices such as the Sagnac loop, ring resonator and the Bragg grating can provide cavities for lasers or sensing and support a wide array of additional device functionalities. For applications such as optical amplifiers and photonic lab-on-chip based sensing, co-doped $Al_2O_3:Er^{3+}:Yb^{3+}$ and hybrid PMMA coated $Si/Si_3N_4:TeO_2$ provide waveguide platforms respectively capable of both.

## 2.6 References


1. S. E. Miller, “Integrated optics: An introduction,” Bell Syst. Tech. J., vol. 48, no. 7, pp. 2059–2069, 1969.
2. Fernández Gavela, D. Grajales García, J. C. Ramirez, and L. M. Lechuga, “Last advances in silicon-based optical biosensors,” Sensors, vol. 16, no. 3, p. 285, 2016.
3. D. Griffiths, “Introduction to Electrodynamics (4th ed.).,” Cambridge Univ. Press., 2017.
4. L. Chrostowski and M. Hochberg, "Silicon Photonics Design," in: Cambridge Univ. Press, pp. 92–961, 2018.
5. S. Schmidt, J. Flueckiger, W. Wu, S.M. Grist, S. Talebi Fard, V. Donzella, P. Khumwan, E.R. Thompson, Q. Wang, P. Kulik, X. Wang, A. Sherwali, J. Kirk, K.C. Cheung, L. Chrostowski, D. Ratner., “Improving the performance of silicon photonic rings, disks, and Bragg gratings for use in label-free biosensing,” Biosensing Nanomedicine VII no. 916660M-1, 2014. 6. C. R. Doerr, “Silicon photonic integration in telecommunications,” Front. Phys., vol. 3, pp. 1–16, 2015.
7. M. Bruel, “Silicon on insulator material technology,” Electron. Lett., vol. 31, no. 14, pp. 1201–1202, 1995.
8. D. J. Thomson, F. Y. Gardes, J. M. Fedeli, S. Zlatanovic, Y. Hu, B. P. Kuo, E. Myslivets, N. Alic, S. Radic, G. Z. Mashanovich, and G. T. Reed, “50-Gb/s silicon optical modulator,” IEEE Photon. Technol. Lett., vol. 24, no. 4, pp. 234–236, 2011.
9. J. D. B. Bradley, P. E. Jessop, and A. P. Knights, “Silicon waveguide-integrated optical power monitor with enhanced sensitivity at 1550 nm,” Appl. Phys. Lett., vol. 86, no. 24, p. 241103, 2005.
10. D. E. Hagan and A. P. Knights, “Mechanisms for optical loss in SOI waveguides for mid-infrared wavelengths around 2 μm,” J. Opt., vol. 19, no. 2, p. 025801, 2016.
11. D. Thomson D, A. Zilkie, J. E. Bowers, T. Komljenovic, G. T. Reed, L. Vivien, D. Marris-Morini, E. Cassan, L. Virot, J. M. Fédéli, J. M. Hartmann, J. H. Schmid, D. X. Xu, F. Boeuf, P. O’Brien, G. Z. Mashanovich, and M. Nedeljkovic, “Roadmap on silicon photonics,” J. Opt., vol. 18, no. 7, p. 073003, 2016.
12. R. Soref, “The past, present, and future of silicon photonics,” IEEE J. Sel. Top. Quantum Electron., vol. 12, no. 6, pp. 1678–1687, 2006.
13. P. Dumon, W. Bogaerts, V. Wiaux, J. Wouters, S. Beckx, J. Van Campenhout, D. Taillaert, B. Luyssaert, P. Bienstman, D. Van Thourhout, and R. Baets, “Low-loss SOI photonic wires and ring resonators fabricated with deep UV lithography,” IEEE Photon. Technol. Lett., vol. 16, no. 5, pp. 1328–1330, 2004.
14. A. P. K. Graham T. Reed, Silicon-On-Insulator (SOI) Photonics. 2004.
15. Y. A. Vlasov and S. J. McNab, “Losses in single-mode silicon-on-insulator strip waveguides and bends,” Opt. Express, vol. 12, no. 8, p. 1622, 2004.
16. Y. Kuo, “Plasma enhanced chemical vapor deposited silicon nitride as a gate dielectric film for amorphous silicon thin film transistors—a critical review,” Vacuum, vol. 51, no. 4, pp. 741–745, 1998.
17. J. F. Bauters, M. J. R. Heck, D. John, D. Dai, M. Tien, J.S. Barton, A. Leinse, R. G. Heideman, D. J. Blumenthal, J. E. Bowers, “Si3N4 waveguides,” Proc. of IEEE, vol. 19, no. 4, pp. 3163–3174, 2011.
18. D. J. Blumenthal, R. Heideman, D. Geuzebroek, A. Leinse, and C. Roeloffzen, “Silicon nitride in silicon photonics,” vol. 106, no. 12, 2018.

19. R. M. De Ridder, K. Warhoff, A. Driessen, P. V. Lambeck, and H. Albers, “Silicon oxynitride planar waveguiding structures for application in optical communication,” IEEE J. Sel. Top. Quantum Electron. vol. 4, no. 6, pp. 930–937, 1998.
20. K. Worhoff, R. M. de Ridder, P. V. Lambeck, and A. Driessen, “Silicon oxynitride in integrated optics,” in IEEE Lasers and Electro-Optics Society, vol. 2, pp. 370–371, 1999.
21. J. F. Bauters, M. J. R. Heck, D. John, D. Dai, M.-C. Tien, J. S. Barton, A. Leinse, R. G. Heideman, D. J. Blumenthal, and J. E. Bowers, “Ultra-low-loss high-aspect-ratio Si3N4 waveguides,” Opt. Express, vol. 19, no. 4, pp. 3163–3174, 2011.
22. J. F. Bauters, M. J. R. Heck, D. D. John, J. S. Barton, C. M. Bruinink, A. Leinse, R. G. Heideman, D. J. Blumenthal, and J. E. Bowers, “Planar waveguides with less than 0.1 dB/m propagation loss fabricated with wafer bonding,” Opt. Express, vol. 19, no. 24, pp. 24090–101, 2011.
23. S. C. Mao, S. H. Tao, Y. L. Xu, X. W. Sun, M. B. Yu, G. Q. Lo, and D. L. Kwong, “Low propagation loss SiN optical waveguide prepared by optimal low-hydrogen module,” Opt. Express, vol. 16, no. 25, pp. 20809–20816, 2008.
24. A. Gorin, A. Jaouad, E. Grondin, V. Aimez, and P. Charette, “Fabrication of silicon nitride waveguides for visible-light using PECVD: a study of the effect of plasma frequency on optical properties,” Opt. Express, vol. 16, no. 18, p. 13509, 2008.
25. J. Yota, J. Hander, A. A. Saleh, “A comparative study on inductively-coupled plasma high-density plasma, plasma-enhanced, and low pressure chemical vapor deposition silicon nitride films,” J. Vac. Sci. Technol. A, vol. 18, pp. 372–376, 2000.
26. D. J. Moss, R. Morandotti, A. L. Gaeta, and M. Lipson, “New CMOS-compatible platforms based on silicon nitride and Hydex for nonlinear optics,” Nat. Photonics, vol. 7, no. 8, pp. 597–607, 2013.
27. A. L. Gaeta, M. Lipson, and T. J. Kippenberg, “Photonic-chip-based frequency combs,” Nat. Photonics, vol. 13, no. 3, pp. 158–169, 2019.
28. J. Mu, M. Dijkstra, J. Korterik, H. Offerhaus, and S. M. García-Blanco, “ High-gain waveguide amplifiers in Si3N4 technology via double-layer monolithic integration,” Photonics Res., vol. 8, no. 10, p. 1634, 2020.
29. J. D. B. Bradley, E. S. Hosseini, Z. Su, T. N. Adam, G. Leake, D. Coolbaugh, M. R. Watts, “Monolithic erbium- and ytterbium-doped microring lasers on silicon chips,” Opt. Express, vol. 22, no. 10, pp. 2394–2396, 2014.
30. E. S. Magden, N. Li, Purnawirman, J. D. B. Bradley, N. Singh, A. Ruocco, G. S. Petrich, G. Leake, D. D. Coolbaugh, E. P. Ippen, M. R. Watts, and L. A. Kolodziejski, “Monolithically-integrated distributed feedback laser compatible with CMOS processing,” Opt. Express, vol. 25, no. 15, pp. 18058–18065, 2017.
31. W. D. Sacher, J. C. Mikkelsen, Y. Huang, J. C. Mak, Z. Yong, X. Luo, Y. Li, P. Dumais, J. Jiang, D. Goodwill, E. Bernier, P. G. Q. Lo, and J. K. S. Poon, “Monolithically integrated multilayer silicon nitride-on-silicon waveguide platforms for 3-D photonic circuits and devices,” Proc. IEEE, vol. 106, no. 12, pp. 2232–2245, 2018.
32. K. Miarabbas Kiani, H. C. Frankis, H. M. Mbonde, R. Mateman, A. Leinse, A. P. Knights, and J. D. B. Bradley, “Thulium-doped tellurium oxide waveguide amplifier with 7.6 dB net gain on a silicon nitride chip,” Opt. Lett, vol. 44, pp. 5788–5791, 2019.

33. H. C. Frankis, K. Miarabbas Kiani, D. B. Bonneville, C. Zhang, S. Norris, R. Mateman, A. Leinse, N. D. Bassim, A. P. Knights, and J. D. B. Bradley, " Low-loss TeO 2 -coated Si3N4 waveguides for application in photonic integrated circuits," Opt. Express, vol. 27, no. 9, p. 12529, 2019.
34. S. A. Vázquez-Córdova, M. Dijkstra, E. H. Bernhardi, F. Ay, K. Wörhoff, J. L. Herek, S. M. García-Blanco, and M. Pollnau, "Erbium-doped spiral amplifiers with 20 dB of net gain on silicon," Opt. Express, vol. 22, no. 21, p. 25993, 2014.
35. K. Worhoff, J. D. Bradley, F. Ay, D. Geskus, T. P. Blauwendraat, and M. Pollnau, "Reliable Low-Cost Fabrication of Low-Loss Al2O3:Er3+ Waveguides With 5.4-dB Optical Gain," IEEE J. Quantum Electron., vol. 25, no. 5, pp. 454–461, 2009.
36. J. D. B. Bradley, L. Agazzi, D. Geskus, F. Ay, K. Wörhoff, and M. Pollnau, "Gain bandwidth of 80 nm and 2 dB/cm peak gain in Al2O3:Er3+ optical amplifiers on silicon," JOSA B, vol. 27, no. 2, pp. 187–196, 2010.
37. J. D. B. Bradley and M. Pollnau, "Erbium-doped integrated waveguide amplifiers and lasers," Laser Photonics Rev., vol. 5, no. 3, pp. 368–403, 2011.
38. M. Goede, L. Chang, J. Mu, M. Dijkstra, R. Obregón, E. Martínez, L.Padilla, F. Mitjans, and S. M. Garcia-Blanco "Al2O3:Yb3+ integrated microdisk laser label-free biosensor," Opt. Lett., vol. 44, no. 24, pp. 5937–5940, 2019.
39. M. Demirtas, C. Odaci, N. K. Perkgoz, C. Sevik, and F. Ay, "Low Loss Atomic Layer Deposited Al2O3 Waveguides for Applications in On-Chip Optical Amplifiers," IEEE J. Sel. Top. Quantum Electron., vol. 24, no. 4, 2018.
40. J. D. B. Bradley, F. Ay, K. Worhoff and M. Pollnau, "Fabrication of low-loss channel waveguides in Al2O3 and Y2O3 layers by inductively coupled plasma reactive ion etching," Appl. Phys. B, vol. 89, pp. 311–318, 2007.
41. R. Wang, H. C. Frankis, H. M. Mbonde, D. B. Bonneville, and J. D. B. Bradley, "Erbium-ytterbium co-doped aluminum oxide thin films: co-sputtering deposition, photoluminescence, luminescent lifetime, energy transfer and quenching fraction," Opt. Mater. (Amst)., vol. 111, p. 110692, 2021.
42. K. Solehmainen, O. G. Oy, and M. Kapulainen, "Erbium-doped waveguides fabricated with atomic layer deposition method," IEEE Photon. Tech. Lett., vol. 16, no. 1, pp. 33–36, 2004.
43. M. Demirtas, C. Odaci, N. K. Perkgoz, and C. Sevik, "Low loss atomic layer deposited Al2O3 waveguides for applications in on-chip optical amplifiers," IEEE J. Sel. Top. Quantum Elec., vol.24, no. 4, 2018.
44. B. Zhou and W. F. Ramirez, "Kinetics and modeling of wet etching of aluminum oxide by warm phosphoric acid," J. Electrochem. Soc., Vol., vol. 143, no. 2, pp. 619–623, 1996.
45. S. J. Madden and K. T. Vu, "Very low loss reactively ion etched Tellurium Dioxide planar rib waveguides for linear and non-linear optics," Opt. Express, vol. 17, no. 20, pp. 369–373, 2009.
46. K. Vu and S. J. Madden, "Tellurium dioxide Erbium doped planar rib waveguide amplifiers with net gain and 2.8dB / cm internal gain," Opt. Express, vol. 18, no. 18, pp. 19192–19200, 2010.
47. K. M. Kiani, H. C. Frankis, C. M. Naraine, D. B. Bonneville, A. P. Knights, and J. D. B. Bradley, "Lasing in a hybrid rare-earth silicon microdisk," *Laser Photonics Rev.*, vol. 16, no. 1, 2022.

48. K. Vu, S. Farahani, and S. Madden, “980nm pumped erbium doped tellurium oxide planar rib waveguide laser and amplifier with gain in S, C and L band,” Opt. Express, vol. 23, no. 2, p. 747, 2015.
49. O. Darrigol, “Georges Sagnac: A life for optics,” Comptes Rendus Phys., vol. 15, no. 10, pp. 789–840, 2014.
50. G. Pascoli, “The Sagnac effect and its interpretation by Paul Langevin,” Comptes Rendus Phys., vol. 18, no. 9–10, pp. 563–569, 2017.
51. R. Anderson, ““Sagnac”’ effect: A century of Earth-rotated interferometers,” Am. J. Phys., vol. 62, p. 975, 1994.
52. Y. Zhang, S. Yang, H. Guan, A.E.-J. Lim, G.-Q. Lo, P. Magill, T. Baehr-Jones, M. Hochberg, “Sagnac loop mirror and micro-ring based laser cavity for silicon-on-insulator,” Opt. Express, vol. 22, no. 15, p. 17872, 2014.
53. H. C. Frankis, “Low-loss TeO2 devices on Si and Si3N4 photonic circuits,” McMaster University, 2021.
54. E. H. Bernhardi, "Bragg-grating-based rare-earth-ion-doped channel waveguide lasers and their applications," University of Twente, 2012.
55. M. Belt and D. J. Blumenthal, “Erbium-doped waveguide DBR and DFB laser arrays integrated within an ultra-low-loss Si3N4 platform,” Opt. Express, vol. 22, no. 9, pp. 10655–10660, 2014.
56. X. Wang, W. Shi, H. Yun, S. Grist, N. A. F. Jaeger, and L. Chrostowski, “Narrow-band waveguide Bragg gratings on SOI wafers with CMOS-compatible fabrication process,” Opt. Express, vol. 20, no. 14, pp. 3013–3015, 2012.
57. S. Zamek, D.T.H. Tan, M. Khajavikhan, M. Ayache, M.P. Nezhad, Y. Fainman, “Compact chip-scale filter based on curved waveguide Bragg gratings,” Opt. Lett., vol. 35 no. 20, 2010.
58. A. D. Simard, Y. Painchaud, and S. Larochelle, “Integrated Bragg gratings in curved waveguides,” IEEE Photon, Conf. vol. 978, no. 1, pp. 4–6, 2010.
59. T. E. Murphy, “Design, fabrication and measurement of integrated Bragg grating optical filters by,” MIT, 2001.
60. M. Pollnau and J. D. B. Bradley, “Optically pumped rare-earth-doped $Al_2O_3$ distributed-feedback lasers on silicon,” Opt. Express, vol. 26, no. 18, pp. 24164–26004, 2018.
61. R. J. Mears, L. Reekie, I. M. Jauncey, and D. N. Payne, “Low-noise erbium-doped fibre amplifier operating at 1.54 μm,” Electron. Lett., vol. 23, no. 19, pp. 1026–1028, 1987.
62. A. W. Fang, H. Park, O. Cohen, R. Jones, M. J. Paniccia, and J. E. Bowers, “Electrically pumped hybrid AlGaInAs-silicon evanescent laser,” Opt. Express, vol. 14, no. 20, pp. 9203–9210, 2006.
63. Y. Fan, J. P. Epping, R. M. Oldenbeuving, C. G. H. Roeloffzen, M. Hoekman, R. Dekker, R. G. Heideman, P. J. M. van der Slot, and K. J. Boller, “Optically integrated InP-Si3N4 hybrid laser,” IEEE Photon. J., vol. 8, no. 6, pp. 1505111, 2016.
64. H. Rong, R. Jones, A. Liu, O. Cohen, D. Hak, A. Fang, and M. Paniccia, “A continuous-wave Raman silicon laser,” Nature, vol. 433, no. 7072, pp. 725–728, 2005.

65. A. G. Griffith, R. K. Lau, J. Cardenas, Y. Okawachi, A. Mohanty, R. Fain, Y. H. Lee, M. Yu, C. T. Phare, C. B. Poitras, A. L. Gaeta, and M. Lipson, “Silicon-chip mid-infrared frequency comb generation,” Nat. Commun., vol. 6, no. 1, pp. 1–5, 2015.
66. N. Singh, M. Raval, A. Ruocco, and M. R. Watts, “Broadband 200-nm second-harmonic generation in silicon in the telecom band,” Light Sci. Appl., vol. 9, no. 1, pp. 1–7, 2020.
67. T. Kitagawa, K. Hattori, K. Shuto, M. Yasu, M. Kobayashi, and M. Horiguchi, “Amplification in erbium-doped silica-based planar lightwave circuits,” Electron. Lett., vol. 28, no. 19, pp. 1818–1819, 1992.
68. T. Kitagawa, K. Hattori, M. Shimizu, Y. Ohmori, and M. Kobayashi, “Guided-wave laser based on erbium-doped silica planar lightwave circuit,” Electron. Lett., vol. 27, no. 4, pp. 334–335, 1991.
69. D. Liang and J. E. Bowers, “Recent progress in lasers on silicon,” Nat. Photonics, vol. 4, no. 8, pp. 511–517, 2010.
70. Z. Fang, Q. Y. Chen, and C. Z. Zhao, “A review of recent progress in lasers on silicon,” Opt. Laser Technol., vol. 46, pp. 103–110, 2013.
71. C. Strohhöfer and A. Polman “Relationship between gain and $Yb^{3+}$ concentration in $Er^{3+}$–$Yb^{3+}$ doped waveguide amplifiers,” vol. 90, no. 9, pp. 4314–4320, 2001.
72. Q. Song, J. Gao, X. Wang, H. Chen, X. Zheng, T. Wang, C. Li, and C. Song, “Fabrication of $Yb^{3+}$:$Er^{3+}$ co-doped $Al_2O_3$ ridge waveguides by the dry etching,” OE. Lett., vol. 46, no.3286, pp. 4–6, 2007.
73. L. Agazzi, J. D. B. Bradley, M. Dijkstra, F. Ay, G. Roelkens, R. Baets, K. Wörhoff, M. Pollnau, “Monolithic integration of erbium-doped amplifiers with silicon-on-insulator waveguides,” Opt. Express, vol. 18, no. 26, p. 27703, 2010.
74. A. Yariv and P. Yeh, "Optical electronics in modern communications," Oxford University, 2006.
75. D. E. McCumber, “Einstein relations connecting broadband emission and absorption spectra,” Phys. Rev, vol. 136, no. 4A, p. A954, 1964.
76. R. C. Hilborn, “Einstein coefficients, cross sections, f values, dipole moments, and all that,” Am. J. Phys., vol. 50, pp. 982–986, 1982.
77. Y. Wang and M. Kong, “Cooperative upconversion effects on the characteristics of $Er^{3+}$ doped and $Er^{3+}$/ $Yb^{3+}$ co-doped waveguide amplifiers,” Opt. - Int. J. Light Electron Opt., vol. 126, no. 9–10, pp. 923–926, 2015.
78. S. T. Fard, S. M. Grist, V. Donzella, S. A. Schmidt, J. Flueckiger, X. Wang, W. Shi, A. Millspaugh, M. Webb, D. M. Ratner, K. C. Cheung, and L. Chrostowski, “Label-free silicon photonic biosensors for use in clinical diagnostics,” Silicon Photonics VIII, vol. 8629, p. 862909, 2013.
79. A. Dhakal, F. Peyskens, S. Clemmen, and A. Raza, “Single mode waveguide platform for spontaneous and surface - enhanced on - chip Raman spectroscopy,” Interface Focus, vol 6, pp. 1–21, 2016.
80. S. Clemmen, A. Raza, A. Dhakal, F. Peyskens, A. Subramanian, P. Van Dorpe, P. Wuytens, H. Zhao, E. Ryckeboer, S. Severi, N. Le Thomas, R. Baets, “Spectroscopic sensing with silicon nitride photonic integrated circuits,” Integr. Opt. Devices, Mater. Technol. XXI, vol. 10106, p. 101060T, 2017.
81. E. Ryckeboer, X. Nie, A.Z. Subramanian, D. Martens, P. Bienstman, S. Clemmen, S. Severi, R. Jansen, G. Roelkens, R. Baets “CMOS-compatible silicon nitride

spectrometers for lab-on-a-chip spectral sensing," Silicon Photonics Photonic Integr. Circuits V, vol. 9891, p. 98911K, 2016.
82. L. Chrostowski, S. Grist, J. Flueckiger, W. Shi, X. Wang, E. Ouellet, H. Yun, M. Webb, B. Nie, Z. Liang, K.C. Cheung, S.A. Schmidt, D.M. Ratner, N. A. F. Jaeger "Silicon photonic resonator sensors and devices," Laser Reson. Microresonators, Beam Control XIV, vol. 8236, p. 823620, 2012.
83. M. de Goede, M. Dijkstra, R. Obregón, J. Ramón-Azcón, E. Martínez, L. Padilla, F. Mitjans, S.M. Garcia-Blanco " $Al_2O_3$ microring resonators for the detection of a cancer biomarker in undiluted urine ," Opt. Express, vol. 27, no. 13, p. 18508, 2019.
84. X. Tu, J. Song, T.-Y. Liow, M. K. Park, J.Q. Yiying, J. S. Kee, M. Yu, and G.-Q. Lo, "Thermal independent Silicon-Nitride slot waveguide biosensor with high sensitivity," Opt. Express, vol. 20, no. 3, p. 2640, 2012.
85. S. TalebiFard, S. Schmidt, W. Shi, W. Wu, N. A. F. Jaeger, E. Kwok, D. M. Ratner, and L. Chrostowski, "Optimized sensitivity of Silicon-on-Insulator (SOI) strip waveguide resonator sensor," Biomed. Opt. Express, vol. 8, no. 2, p. 500, 2017.
86. I. Goykhman, B. Desiatov, and U. Levy, "Ultrathin silicon nitride microring resonator for biophotonic applications at 970 nm wavelength," Appl. Phys. Lett., vol. 97, no. 8, pp. 30–32, 2010.
87. C.A. Barrios, B. Sánchez, K.B. Gylfason, A. Griol, H. Sohlström, M. Holgado, and R. Casquel, "Demonstration of slot-waveguide structures on silicon nitride / silicon oxide platform," Opt. Express, vol. 15, no. 11, p. 6846, 2007.
88. C. A. Barrios, "Optical slot-waveguide based biochemical sensors," Sensors (Switzerland), vol. 9, no. 6, pp. 4751–4765, 2009.
89. J. Hu, X. Sun, A. Agarwal, and L. C. Kimerling, "Design guidelines for optical resonator biochemical sensors," J. Opt. Soc. Am. B, vol. 26, no. 5, pp. 1032–1041, 2009.
90. T. Reynolds, N. Riesen, A. Meldrum, X. Fan, J.M.M. Hall, T.M. Monro, and A. François "Fluorescent and lasing whispering gallery mode microresonators for sensing applications," Laser Photonics Rev., vol. 11, no. 2, pp. 1–20, 2017.
91. E.H. Bernhardi, K.O. van der Werf, A.J.F. Hollink, K. Wörhoff, R.M. de Ridder, V. Subramaniam, and M. Pollnau, "Intra-laser-cavity microparticle sensing with a dual-wavelength distributed-feedback laser," Laser Photonics Rev., vol. 7, no. 4, pp. 589–598, 2013.
92. L. He, Ş. K. Özdemir, J. Zhu, W. Kim, and L. Yang, "Detecting single viruses and nanoparticles using whispering gallery microlasers," Nat. Nanotechnol., vol. 6, no. 7, pp. 428–432, 2011.
93. E. P. Ostby and K. J. Vahala, "Yb-doped glass microcavity laser operation in water," Opt. Lett., vol. 34, no. 8, p. 1153, 2009.
94. R. Landgraf, M. K. Kaiser, J. Posseckardt, B. Adolphi, and W. J. Fischer, "Functionalization of polymer sensor surfaces by oxygen plasma treatment," Procedia Chem., vol. 1, no. 1, pp. 1015–1018, 2009.
95. S. Sathish, N. Ishizu, and A. Q. Shen, "Air plasma-enhanced covalent functionalization of poly(methyl methacrylate): high-throughput protein immobilization for miniaturized bioassays," ACS Appl. Mater. Interfaces, vol. 11, no. 49, pp. 46350–46360, 2019.

# Chapter 3

## Silicon Nitride Thin-Film Deposition by ECR-PECVD for Optical Waveguides

Reprinted in part with open access permissions from: Bonneville, D.B.; Miller, J.W.; Smyth, C.; Mascher, P.; Bradley, J.D.B. Low-Temperature and Low-Pressure Silicon Nitride Deposition by ECR-PECVD for Optical Waveguides. *Appl. Sci.* **2021**, *11*, 2110. https://doi.org/10.3390/app11052110

This chapter includes the findings presented in a published manuscript on the deposition of $Si_3N_4$ thin films using an electron cyclotron resonance plasma enhanced chemical vapour deposition (ECR-PECVD) chamber. Using a low temperature and low pressure process, the films were deposited and then characterized using variable angle spectroscopic ellipsometry, prism coupling, atomic force microscopy, Rutherford backscattering spectrometry and elastic recoil detection. This revealed information about the fabrication parameters' effect on film properties such as refractive index, thickness, optical loss, surface roughness, stoichiometry and hydrogen content. High temperature annealing was shown to lead to almost 100% hydrogen release, a refractive index increase, a thickness decrease, and mechanical failure in the majority of the films deposited on oxidized silicon substrates, except one sample which demonstrated a slight reduction in optical loss. It is concluded that for non-stoichiometric $SiO_xN_y:H_z$ films, low optical loss can be achieved in the visible and near infrared without annealing. Subtleties regarding the deposition conditions, thin film properties, and various conclusions which can help guide future work on thin films fabricated using ECR-PECVD are highlighted in

the following chapter. Sections included in the following chapter which were not published in the manuscript include Figure 3.1, which is a re-print from a newly referenced thesis, and a paragraph after Table 3.1 which discusses the selection of gas flow rates. These alterations were made to better illustrate the deposition system and give reasoning for arriving at a relatively higher Silane flow rate. Sub-sections were also added to better organize the fabrication section. This chapter demonstrates a versatile thin film fabrication technique with a thermal budget and deposition conditions that make it useful for a variety of substrates, which is a centralized theme to the thesis.

**Abstract:** We report on low temperature, low pressure deposition conditions of 140 °C and 1.5 mTorr**,** respectively, to achieve high optical quality silicon nitride thin films. We deposit the silicon nitride films using an electron cyclotron resonance plasma-enhanced chemical vapour deposition (ECR-PECVD) chamber with Ar diluted $SiH_4$, and $N_2$ gas. Variable-angle spectroscopic ellipsometry was used to determine the thickness and refractive index of the silicon nitride films, which ranged from 300 to 650 nm and 1.8 to 2.1 at 638 nm, respectively. We used Rutherford backscattering spectrometry to determine the chemical composition of the films, including oxygen contamination, and elastic recoil detection to characterize the removal of hydrogen after annealing. The as-deposited films are found to have variable relative silicon and nitrogen composition with significant oxygen content and hydrogen incorporation of 10–20 and 17–21 %, respectively. Atomic force microscopy measurements showed a decrease in root mean square roughness after annealing for a variety of films. Prism coupling measurements show losses as low as 1.3, 0.3 and 1.5 ± 0.1 dB/cm at 638, 980 and 1550 nm respectively

without the need for post-process annealing. Based on this study, we find that the as-deposited ECR-PECVD $SiO_xN_y:H_z$ films have suitable thickness, refractive index, and optical loss for their use in visible and near-infrared integrated photonic devices.

## 3.1 Introduction

As thin film silicon nitride ($Si_3N_4$) becomes a standard material in integrated photonics, the need for a broad range of deposition recipes for different applications becomes apparent. $Si_3N_4$ has many demonstrations as a low loss waveguide material [1–6] for diverse applications due to its transparency in the visible and near-infrared (NIR), such as biological sensing and particle manipulation, environmental monitoring, optical interconnects, and anti-reflective (AR) coatings [7–12]. Due to the need for $Si_3N_4$ integration with metal components or organic materials for many of these uses, it is advantageous to have flexible fabrication techniques that operate at lower deposition temperatures and pressures.

There is an extensive background of published literature on the formation of amorphous silicon nitride films through chemical vapour deposition (CVD) processes. Low pressure CVD (LPCVD) is commonly used to achieve low loss stoichiometric $Si_3N_4$ [13], features high deposition temperatures around 650 to 900 °C, and has been incorporated in silicon photonics platforms [9,14,15]. However, these high deposition temperatures might pose fabrication constraints with silicon photonic chips with dopants and metal layers, or other substrates which are sensitive to higher temperatures. Most metals used in tunable heaters and optoelectronic devices can be damaged at temperatures exceeding ~400 °C, which makes post-metalized chips incompatible with LPCVD chambers. Plasma enhanced CVD (PECVD) is also extensively used in the fabrication of silicon nitride thin films. PECVD systems operate below 450 °C, owing to

the plasma operating as an auxiliary energy source, and are more suited to post-fabrication processing. Low loss silicon nitride waveguides have been fabricated using PECVD [16]. One main disadvantage of PECVD techniques is the relatively high concentration of incorporated hydrogen in the samples resulting in low density structures and producing low refractive index films. These highly hydrogenated films also exhibit more significant optical losses in the C-band due to Si-H and N-H bonds [2]. It is possible to remove the hydrogen from the films either through annealing or utilizing precursor gases that do not contain hydrogen, such as switching from $NH_3$ to $N_2$ [17]. Other varieties of CVD techniques can help mitigate the high concentrations of hydrogen. These include inductively coupled plasma (ICP-PECVD) [19,20], high-density plasma (HDP-CVD) [13], and electron cyclotron resonance (ECR-PECVD) [20–24]. These techniques allow for high power densities, resulting in greater dissociation of the precursor gases and lower hydrogen incorporation into the films. Low pressures of 1–2 mTorr are realized in ECR-PECVD by using a strong magnet to confine and stabilize the plasma during deposition, whereas inductively coupled plasma (ICP) techniques, typically operate at pressures > 10 mTorr [13]. Interestingly, in the case of ICP-PECVD and ECR-PECVD, the reaction chamber is separate from the plasma chamber allowing for high-quality films to be produced at low temperatures and pressures without the risk of surface damage from high energy bombardment. Limiting surface damage is of particular interest in waveguide fabrication as scattering at the material interface is a significant source of optical loss.

Optical waveguide fabrication through ECR-PECVD has been explored [16,25,26] in various systems demonstrating it as a viable candidate for the fabrication of visible and NIR waveguides. Variation in film stoichiometry by changing the nitrogen/silane ($N_2/SiH_4$)

gas ratio during ECR-PECVD fabrication has been investigated, with optical losses of <1.0 and 1.5 dB/cm at 1310 and 1550 nm for N-rich and nearly stoichiometric films respectively [2]. However, films in [2] were deposited at 350 °C and a minimum chamber pressure of 650 mTorr, which is two orders of magnitude higher than the deposition pressures shown here. By measuring optical loss at visible and NIR telecom wavelengths, and characterizing film stoichiometry as well as unwanted contaminants like oxygen, we demonstrate a non-stoichiometric film capable of suitable device performance, fabricated at relatively low deposition pressures and temperatures compared to existing literature.

We report on hydrogenated silicon nitride films deposited using a low temperature and low pressure ECR-PECVD system. The stoichiometry of the films as well as the impacts of annealing on the hydrogen content are studied through Rutherford backscattering spectrometry (RBS) and elastic recoil detection analysis (ERDA), respectively. Low pressure recipes ranging from 1.1–2.4 mTorr with deposition temperatures of 140 °C show pre-annealing optical losses in the visible to NIR range suitable for integrated optical devices. We demonstrate that the associated optical losses of hydrogenated non-stoichiometric PECVD silicon nitride ($SiO_xN_y:H_z$), as reported in the literature [13] are reasonable for specific applications requiring low temperature deposition conditions and access to thicker films up to 650 nm. We characterized the thin film optical loss across a broad wavelength range including visible and telecommunication bands from 638 to 1640 nm using prism coupling and observe low surface roughness measured through atomic force microscopy (AFM). Low losses are achieved without post-fabrication annealing treatment, which is typically required to reduce significantly higher losses in the telecommunication bands due to hydrogen bonds [27–30]. These characteristics

demonstrate ECR-PECVD to be a highly promising method for planar waveguide fabrication.

## 3.2 Fabrication

### 3.2.1 System Specifications

We deposited silicon nitride thin films on various substrates using an ECR-PECVD system. The system is divided into three parts allowing for separate load-lock, main chamber and ECR plasma generation sections. The remotely generated ECR plasma allows for high fractional ion density at low process pressure limiting the damage to the film during growth. A forward microwave power of 500 W is applied through a quartz window near an 875 G electromagnet with $N_2$, $O_2$ and Ar inlets for ECR plasma generation during deposition. In the ECR plasma generation section of the chamber, the strong electromagnet is used to minimize ionized plasma species sidewall reactions and confine electron motion to field lines concentrated towards the sample surface inside the main chamber. Due to the relatively small main chamber size of roughly 10 cm radius, deposition pressures in the 1–2 mTorr range are possible using ECR assisted confinement. A more detailed description of the system and the orientation of the gas shower heads, ECR plasma section, and sample holder can be found in Figure 22 and Figure 27 in [31]. These features are aimed at lowering the incorporation of interstitial hydrogen, an unwanted contamination which leads to strong absorption in the S and C telecommunication wavelength windows [2]. The system's low deposition pressure with operating conditions shown here of 1–2 mTorr, also ensures a low concentration of Si-H bonds to form during deposition while using $SiH_4$ precursors, limiting interstitial hydrogen incorporation during deposition, as is a common drawback in PECVD systems. Another expected source of hydrogen is invasive $H_2O$ in the form of water vapour likely entering

the chamber through the ~5-m long gas transit lines, and potentially residual from the sample transfer process. Additionally, oxygen creep into the chamber during sample transfer reacting with hydrogen from the silane precursor is another expected source. This also explains the presence of oxygen in the films which has been quantified with RBS. The deposition system uses dedicated turbopumps for both the main chamber and the separate load-lock chamber keeping the main chamber isolated during venting for transfer. The system is also equipped with in-situ sputtering [32] and metal organic delivery lines which provide in-situ incorporation of rare-earths for the development of solid-state lighting devices. Additionally, it has been used for the formation of silicon nanoclusters embedded in $Si_xN_y$ [33]. A schematic diagram of the ECR-PECVD system is shown in Fig. 3.1, demonstrating the rough interconnection between sub-systems and their orientation, reprinted from [34]. Further details on the system specifications and upgrades such as integrated magnetron sputtering can be found in [34].

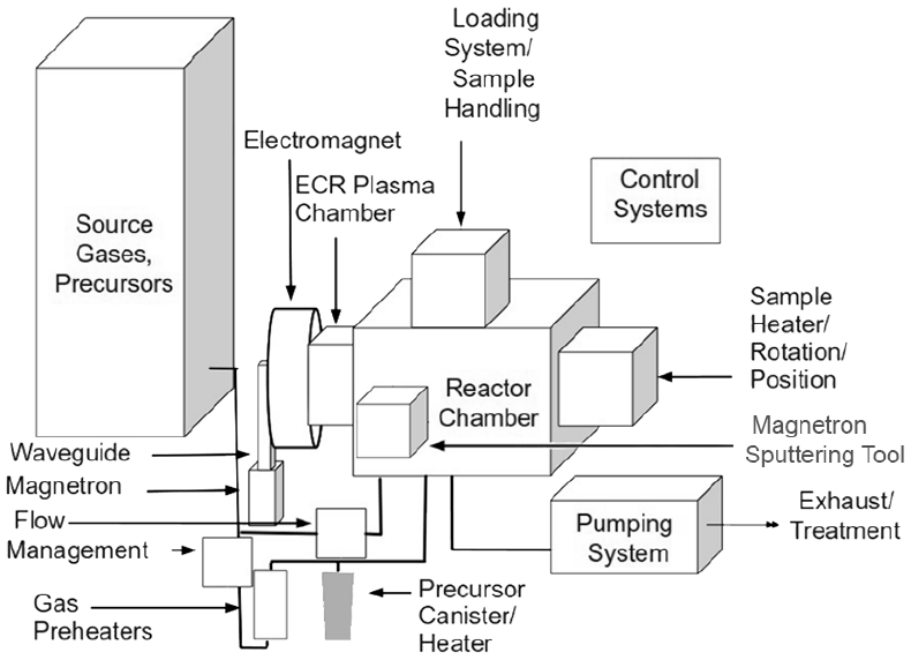


**Figure 3.1.** Schematic drawing of major sub-systems in the ECR-PECVD system including integrated magnetron sputtering tool. Figure re-printed from [34].

### 3.2.2 $SiO_xN_y:H_z$ Film Deposition via ECR-PECVD

We deposited $SiO_xN_y:H_z$ films on different substrate materials mounted to a stainless-steel stage with tungsten clips to secure the samples. The sample stage sits inside the main chamber, mounted on a motor-controlled arm for rotation, holding the sample face normal to the precursor gas showerhead, and ECR generated plasma. A heating element in contact with the back of the sample stage allows for evenly distributed heating, which provides additional surface energy for the reaction. As mentioned, the strong ECR plasma acts as an auxiliary power source for the reaction, allowing the lower deposition temperatures when compared to ICP depositions. Sample stage rotation was maintained at a constant 0.5 Hz during all of the depositions and the substrates were heated to 140 °C. The partial pressure from each introduced gas species was allowed to vary throughout the deposition whilst maintaining a constant gas flow rate. This resulted in the partial

pressure from each gas being on average 5% higher by the end of the deposition. The partial pressures imparted by each of the gases at the start of depositions are shown in Table 3.1, with an assumed associated error of ±0.01. Across the film recipes $SiH_4$/Ar flow was held constant while the $N_2$/Ar flow was varied. This was due to the higher range of gas flow choices associated with higher flow rates from the mass flow controller (MFC) with $N_2$/Ar gas flow. Any change of the silane flow would result in a drastic stoichiometry variation even across 0.1 sccm of gas flow change. With an expected uncertainty and occasional variation of ~0.1 sccm of flow from any of the MFC units, a safer smaller stoichiometry change is available by changing $N_2$/Ar flow across the ranges shown in Table 3.1. Silane and nitrogen dilution were 30/70 % and 10/90 % with Argon, respectively. The sample stage is 3 inches in diameter and was used to fix multiple substrates to the stage at once One round of thick (~300–450 nm) films were deposited on 2x2 $cm^2$ silicon pieces and on 6 µm of thermally grown $SiO_2$ on 5x3 $cm^2$ silicon pieces ($SiO_2$-Si) cleaved from a fully oxidized wafer, for ellipsometry and thin film optical loss measurements, respectively. The deposition time for the first round was 3.5 hours, and 1 hour for the second round of depositions, producing thinner films (~100 nm) for RBS and ERDA measurements on 2x2 $cm^2$ pieces of vitreous carbon and silicon, respectively. After preliminary studies on optical loss and recipe optimization had been performed, a final thicker (650 nm) film was deposited on silicon and a 5x3 $cm^2$ cleaved piece of an $SiO_2$-Si wafer to increase modal confinement in the $SiO_xN_y$:$H_z$ layer when performing optical loss measurements. The deposition parameters used for the different film recipes are summarized in Table 3.1, including pre-deposition pressures, and pressures during depositions imparted by each partial gas flow.

**Table 3.1.** $SiO_xN_y:H_z$ thin film deposition parameters

| Deposition Parameters | Film 1 | Film 2 | Film 3 | Film 4 | Film 5 | Film 6 |
|---|---|---|---|---|---|---|
| $N_2$/Ar (10/90%) flow rate (sccm) | 10.0 | 12.5 | 15.0 | 17.5 | 20.0 | 15.0 |
| $SiH_4$/Ar (30/70%) flow rate (sccm) | 5.0 | 5.0 | 5.0 | 5.0 | 5.0 | 5.0 |
| $N_2$/Ar partial pressure – round 1(mTorr) | 1.15 | 1.40 | 1.64 | 1.83 | 2.10 | 1.63 |
| $N_2$/Ar partial pressure – round 2 (mTorr) | 1.18 | 1.43 | 1.62 | 1.87 | 2.09 | N/A |
| $SiH_4$/Ar partial pressure – round 1 (mTorr) | 1.60 | 1.79 | 2.01 | 2.24 | 2.45 | 2.02 |
| $SiH_4$/Ar partial pressure – round 2 (mTorr) | 1.62 | 1.81 | 1.98 | 2.24 | 2.49 | N/A |
| Pre-deposition pressure – round 1 (Torr) | $9.5 \times 10^{-8}$ | $8.0 \times 10^{-8}$ | $4.8 \times 10^{-8}$ | $5.6 \times 10^{-8}$ | $1.6 \times 10^{-7}$ | $7.5 \times 10^{-7}$ |
| Pre-deposition pressure – round 2 (Torr) | $2.2 \times 10^{-8}$ | $1.1 \times 10^{-7}$ | $7.5 \times 10^{-8}$ | $7.0 \times 10^{-8}$ | $8.5 \times 10^{-8}$ | N/A |
| Deposition time for round 1 (min) | 210 | 210 | 210 | 210 | 210 | 380 |
| Deposition time for round 2 (min) | 90 | 90 | 90 | 90 | 90 | N/A |
| Temperature (°C) | 140 | 140 | 140 | 140 | 140 | 140 |

An initial round of depositions was performed with a $SiH_4$ flow of 2.5 sccm, and $N_2$/Ar flows from 5–20 sccm. It was discovered that in this range of deposition conditions unstable reflected power spikes occurred, expected to be caused by the lower-pressure conditions in the range of 1.0–1.5 mTorr. To perform depositions with lower $SiH_4$ flow rates, it is recommended to use increased Ar flows to compensate the partial pressure decrease.

### 3.2.3 Annealing

To investigate the presence and removal of hydrogen in the films, annealing under ambient $N_2$ flow was carried out in a quartz tube furnace. We selected 1000 °C for 1 hour for hydrogen removal based on multiple findings [29,30]. Characteristics reported for

hydrogen release include lower optical losses, decreased thicknesses, and increased indices of refraction due to film densification. The films were annealed with an open exhaust and $N_2$ flow rate of 500 sccm in a 3-inch x 2-meter-long furnace. Films were inserted into the furnace at maximum temperature on a quartz wafer boat and pulled out of the furnace but left in the tube and allowed to cool adjacent of the heating zones during a 4 hour ramp down.

## 3.3 Characterization

### 3.3.1 Refractive Index & Thickness

We used a combination of variable-angle spectroscopic ellipsometry (VASE) and prism coupling to determine the refractive index and thickness of the $SiO_xN_y:H_z$ films on the silicon and thermally-oxidized silicon pieces, respectively. The results of the refractive index and thickness measurements are displayed in Fig. 3.2. The anticipated relationship was observed between the $N_2$/Ar flow rate and refractive index, with films having a higher refractive index at decreased $N_2$/Ar:$SiH_4$/Ar flow rate ratios due to increasing silicon content. An expected trend is observed in the deposition rate which increases from 1.43 to 2.11 nm/min for Film 1 and Film 5, respectively. This is correlated to the increase in $N_2$/Ar flow rate providing a higher concentration of $N_2$ in the chamber and increased pressures during film growth. The films show the expected behaviour of decreased thickness after annealing, which can be attributed to hydrogen removal and film densification. Additionally, increased refractive index is observed after annealing, which is consistent with film densification as has been seen in [28].

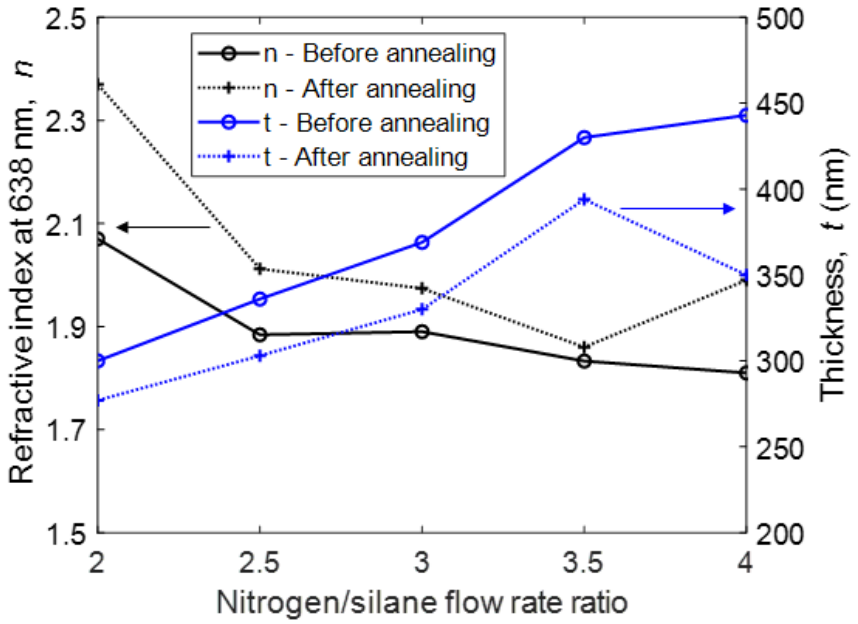


**Figure 3.2.** Refractive index and thickness of films deposited for 3.5 hours at 140 °C with varying $N_2$/Ar:$SiH_4$/Ar flow rate ratios before and after annealing at 1000 °C for 1 hour in ambient nitrogen (500 sccm). Connecting lines are to help guide the eye.

The films were grown from 300–450 nm thick to ensure a planar waveguide mode was supported at 1550 nm**,** without the need for a top-cladding layer. This allowed for the refractive index, thickness and loss to be measured using prism coupling at longer wavelengths, including 1550 and 1640 nm. However, at these thicknesses, we observed the annealed films lifting off the edges of 80% of the samples which were deposited on large $SiO_2$-Si substrates, which is due to the known tensile stress in $Si_xN_y$ films. We measured film refractive indices in the range of 1.81–2.07 before annealing across the $N_2$/Ar:$SiH_4$/Ar flow ratios shown in Fig. 3.2. Film 5 with the highest $N_2$/Ar flow showed a drastic thickness decrease of ~100 nm after annealing, while Film 1 with the lowest $N_2$/Ar flow showed a drastic increase of index of ~0.33. This is anticipated to be a cause of Film 1 and Film 5 being respectively overly silicon and nitrogen rich and therefore in different

dominant regimes for Si-H and N-H bonding. Film 5 moreover is likely in a regime beyond the stoichiometric film ratio [2] causing a difference in bond reorganization in comparison to the other films after annealing.

### 3.3.2 Optical Loss

In order to study the $SiO_xN_y:H_z$ films as candidates for optical waveguides, a significant merit is a low optical loss. To quantify this, we used prism coupling to excite the transverse-electric (TE) polarized fundamental planar modes in the film and measure their decay as they propagate through the $SiO_xN_y:H_z$ layer with a scanning fiber normal to the surface and coupled to a photodetector. This was carried out before annealing at four different wavelengths including 638, 847, 1310, and 1550 nm, as shown in Fig. 3.3.

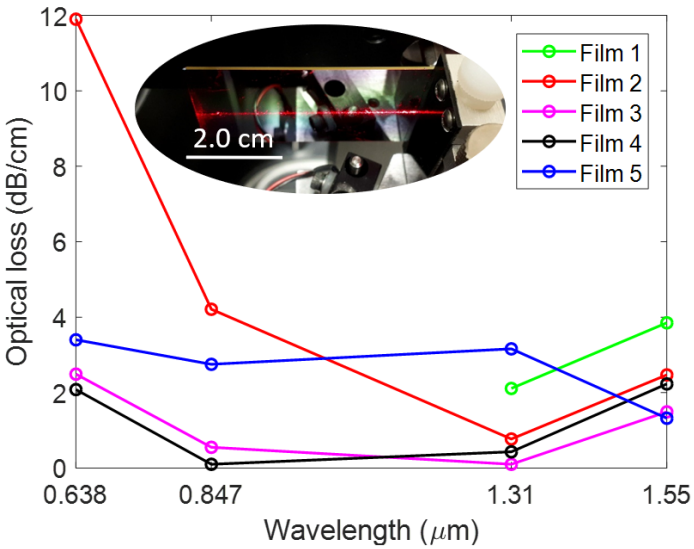


**Figure 3.3.** Optical loss determined via prism coupling at various wavelengths in the visible to infrared for each $SiO_xN_y:H_z$ film. The films were deposited on 6-μm thermally grown $SiO_2$ layers on Si substrates. Connecting lines are to help guide the eye. Inset: red light streak from Film 3 visible during 638 nm loss measurement.

The loss for Film 1 at 638 and 847 nm was too high to be measured on the system. This is anticipated because of the higher Si content in Film 1 as a result of a decreased

$N_2$/Ar:$SiH_4$/Ar flow rate ratio. A similar trend is observed in Film 2, which exhibits high visible loss but promising losses in the 1310–1550 nm range. Films 3 and 4 demonstrate relatively low losses at all wavelengths and less than 0.5 dB/cm at 847 and 1310 nm, while Film 5 exhibits higher loss at these wavelengths. Film 5 was deposited with the highest $N_2$/Ar:$SiH_4$/Ar flow rate ratio and the highest pre-deposition pressure. It is likely that this recipe leads to films rich in N-H bonds which is known to be an unwanted source of optical loss [2]. The increased loss at shorter wavelengths is anticipated to be a result of increased Si-H bonds in this deposition regime, potentially past the stoichiometric point of gas ratios.

In order to further investigate the films' optical quality, we measured the loss at a finer spacing of wavelengths from 1510–1600 nm, as shown in Fig. 3.4(a). The incorporation of hydrogen in the films is expected to lead to additional absorption in this wavelength regime [2]. Films 1–3 demonstrate higher loss around 1510 nm and a decrease of loss towards longer wavelengths past ~1540 nm, indicative of the presence of hydrogen in the films. Films 4 and 5, however, show consistent or increasing losses across this wavelength regime indicative of other dominant loss mechanisms rather than hydrogen absorption, such as substrate interaction or intrinsic material loss. Film 2 was the only film which was measurable for loss after annealing, demonstrated as Film 2A in Fig. 3.3(a), showing a loss decrease from 1520–1550 nm. This was due to all other films deposited on $SiO_2$-Si lifting off or cracking during the anneal step. To increase modal interaction with the planar waveguide layer, we also deposited a thicker film with the same recipe as Film 3, shown in Table 3.1 denoted as Film 6. This recipe was chosen as it demonstrated the lowest losses on average from visible to NIR telecommunication wavelengths. The

loss results for this 650 nm thick film are shown in Fig. 3.4 (b) from 638–1620 nm with finer 1480–1580 nm spacing shown in the inset.

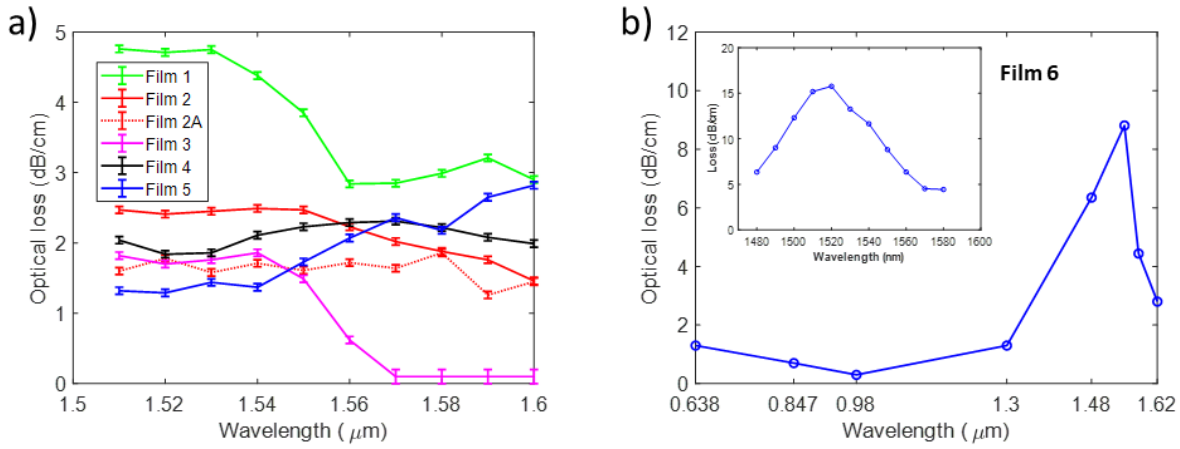


**Figure 3.4.** a) Optical loss of various films determined via prism coupling from 1510–1600 nm. b) Optical loss determined via prism coupling at various wavelengths in the visible to infrared for Film 6 and finer spaced loss measurements from 1480–1580 nm (inset). Connecting lines are to help guide the eye.

Each data point represents a loss measurement derived from a fit to an exponential loss curve obtained from a normally scanning fiber during measurement. The inherent uncertainty in this method is reflected in the data and increased for Film 3, which shows propagation losses on the order of 0.1 dB/cm beyond 1570 nm in Fig. 3.4(a), which is the measurable limit for the system. This loss trend is promising for applications in the telecommunications L-band (1570–1620 nm) and potentially longer wavelengths where new telecommunication and sensing windows are demanding low loss waveguides. Figure 3.4(b) shows that the thicker film has significantly higher losses from 1510–1580 nm with still relatively low losses at 638, 847, 980 and 1310 nm. Increasing the film thickness from 369 to 650 nm increases the modal interaction and overlap with the planar waveguide layer from ~70.0 to ~89.0 % at 1510 nm, while decreasing the interaction with

the air from ~8.9 to ~3.5 %. Doing so resulted in a film which demonstrates visible–NIR losses as low as 0.3 dB/cm at 980 nm, with increased C-band losses as high as ~8.0 dB/cm at 1550 nm shown in Fig. 3.4(b) and the inset, respectively. The increase in loss for Film 6 is expected to be attributed to the increased modal interaction with the hydrogen in the $SiO_xN_y:H_z$ films due to increased thickness. It may also be the case that increased pre-deposition pressures lead to higher hydrogen incorporation in comparison to Film 3.

Annealing the samples at 1000 °C for 1 hour caused the majority of films to be immeasurable due to stress-induced lifting of the film off the $SiO_2$, or in one case for Film 5, total failure showing visible cracks throughout the whole deposited layer. This was expected, as the films are relatively thick for $Si_xN_y$ depositions and therefore are expected to have high tensile stress. However, this was not the case for Film 2, which demonstrated a loss decrease of 0.8±0.1 dB/cm from 1520–1550 nm after annealing and not lifting off. This might be attributed to higher Si content in the film and decreased tensile stress. This data is shown as Film 2A in Fig. 3.3(a), with a dotted line to guide the eye in comparison to the losses measured prior to annealing. The remaining ~1.6 dB/cm of loss in this range suggests that other loss mechanisms rather than hydrogen content still need to be overcome for the S–L bands in our ECR-PEVCD $SiO_xN_y:H_z$ films.

### 3.3.3 Surface Roughness

To quantify the surface roughness of the films, we used AFM to inspect 1x1 $\mu m^2$ areas on multiple locations for selected samples on Si substrates. Films 2 and 3 were chosen due to their drastically different optical losses for visible wavelengths. It is anticipated any surface roughness will increase scattering losses, especially in the visible regime with the known $1/\lambda^4$ relationship. Surface homogeneity was also inspected and used to quantify uncertainty on the root mean square (RMS) reported roughness and peak-peak amplitude

values. A correlation between annealing and decreased peak-peak height is observed when measuring Film 3 before and after annealing; however, it is noted that for films of similar RMS roughness, drastically different (~10 dB/cm at 638 nm) optical loss is reported. A decrease in peak-peak amplitude of 1.65 ± 0.40 nm is observed after annealing Film 3, which is attributed to the densification of the film. After annealing out the hydrogen in Film 2, it demonstrates a higher optical loss at 1550 nm compared to the unannealed Film 3, while still demonstrating less surface roughness (RMS and peak-peak) as shown in Table 3.2 which summarizes the AFM amplitude plots in Fig. 3.5. This points to stoichiometry dominated optical loss mechanisms for the ECR-PECVD $SiO_xN_y:H_z$ films. This can also be attributed to the low percentage of optical intensity in the upper air cladding, on the order of ~3–9 % for most films measured. Moving forward, this is an important merit for multilayer systems, where interface losses may be exacerbated by higher surface roughness.

**Table 3.2.** Surface roughness from atomic force microscopy

| Film # | 2, annealed | 3, as-deposited | 3, annealed |
|---|---|---|---|
| RMS roughness (nm) | 0.95 ± 0.01 | 1.10 ± 0.01 | 1.01 ± 0.05 |
| Peak-peak amplitude (nm) | 9.55 ± 0.16 | 9.58 ± 0.12 | 7.93 ± 0.38 |

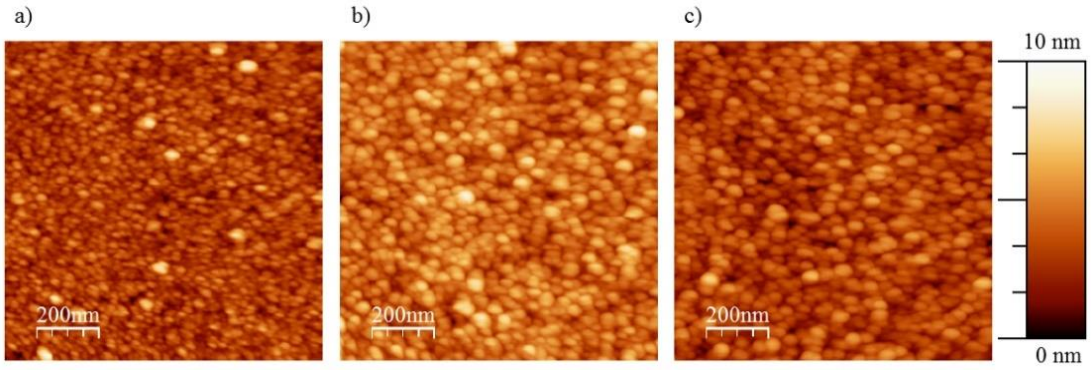


**Figure 3.5.** a) AFM amplitude plot for Film 2 annealed, b) Film 3 un-annealed, c) Film 3 annealed.

### 3.3.4 Composition Measurements

As shown in Table 3.1, a second round of depositions was performed to produce thinner films, on carbon substrates for RBS measurements, as well as 2x2 $cm^2$ Si pieces for annealing and ERDA measurements. The $SiO_xN_y:H_z$ films deposited on carbon substrates were used to measure RBS data while allowing for a separation of recoil energies between film and substrate, while the films deposited on Si pieces were used to quantify the amount of hydrogen incorporation via ERDA. Data was collected using a tandetron accelerator with $He^{4+}$ ions at 1.8 MeV 4° incident for RBS, and 2.9 MeV incident at a grazing angle of 75° for ERDA. The data obtained for each film is shown in Fig. 3.6. The uncertainty is reflected in the data point size for RBS, while the ERDA data is fit with higher sample dependent uncertainty due to a higher sensitivity with changing fit parameters.

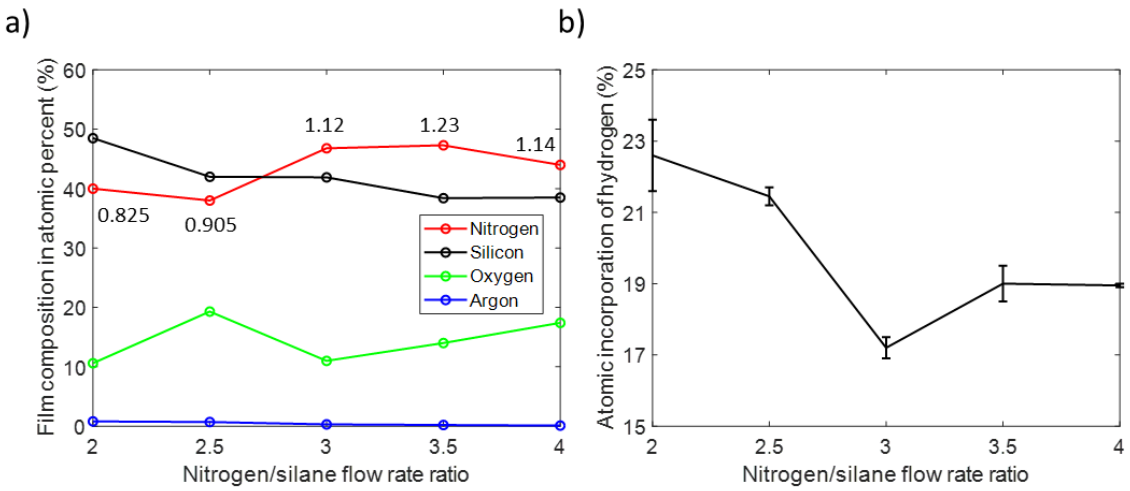


**Figure 3.6.** a) Film composition determined from RBS excluding hydrogen with N/Si ratio indicated. b) Hydrogen incorporation determined from ERDA before annealing. The incorporated hydrogen after annealing was measured to be below 0.1 at.% for all films. Connecting lines are to help guide the eye.

The deposition recipes studied produce films of varying N/Si composition ratios, which demonstrate an oxygen, and argon content of 10–20 and < 1% respectively. We observe the expected trend of decreasing Si content as the $N_2$/Ar flow increases, and conversely, the film composition becomes closer to a stoichiometric N/Si ratio of 1.333, as indicated in Fig. 3.6(a). However, this trend is no longer observed with further increasing $N_2$/Ar:$SiH_4$/Ar flow rate ratios as shown in [2]. We observe less nitrogen content in Film 5, at 20 sccm of $N_2$/Ar flow during deposition. This is also coupled with an increase in oxygen content in the film. The films contain 10 to 20% oxygen, as shown in Fig. 3.6(a), which would indicate the deposition of silicon-oxynitride films. However, the relatively high oxygen content does not correlate with the expected refractive index in such films, which typically have indices ranging from 1.48–1.68 using PECVD [35,36]. Future work aims to understand the distribution and bonding nature of $O_2$ in this system using Fourier

transform infrared spectroscopy (FTIR). The contamination is expected to be due to water vapour present in the vacuum chamber due to sample transfer, and possible $N_2$/Ar contamination with ambient $O_2$ from the gas transit lines before the MFC. The oxygen content is also anticipated to be a cause of the decreased N content as more Si-O bonds start to be favoured during deposition, rather than Si-N bond formation [37]. The abundance of oxygen in our film matrix can be explained by the presence of oxygen radicals in the plasma. At low $N_2$/Ar flow rates, there are low quantities of N radicals leading to Si-H or Si-Si bonds becoming favourable, resulting in the production of a silicon-rich film [38,39]. This effect is observed in Fig. 3.6(a), with a flow rate of 10 sccm of $N_2$/Ar producing a silicon-rich $SiO_xN_y:H_z$ film. ERD measurements show typical hydrogen incorporation of roughly 20% across the deposited films for ECR-PECVD deposition [13]. The lowest loss film (Film 3) is also the film showing the lowest hydrogen incorporation of 17.2 ± 0.5 at.%. After annealing, all films show below 0.1 at.% hydrogen incorporation.

Future work will focus on minimizing hydrogen in the chamber by decreasing $SiH_4$/Ar flow, and possibly including Argon flow to keep operating pressures at ~1–2 mTorr while also decreasing $N_2$/Ar flow. This may also be beneficial in reducing the $O_2$ content in the film or potentially providing insight into its sources. Additionally, longer pump down times after sample transfer before deposition may achieve a lower concentration of water vapour in the chamber, as well as a chamber bake step, which will both be considered in the future. The recipes used have shown that a non-stoichiometric and medium hydrogenated film leads to thicknesses and optical losses acceptable for integrated photonic devices for the visible and NIR wavelength regions. Some recipes show

promising losses in the important S, C and L communications bands even in unannealed films and further investigation of deposition conditions and recipes can lead to reduced hydrogen incorporation and losses in that spectral region.

### 3.4 Conclusion

We deposited $SiO_xN_y:H_z$ films on various substrates using ECR-PECVD with a fixed $SiH_4$/Ar precursor and varied $N_2$/Ar flow at 140 °C from 1.60–2.45 mTorr. To characterize the films, we used VASE and prism coupling to measure the refractive index and thickness, as well as the optical loss, respectively, before and after annealing. Refractive indices ranging from 1.81–2.07 were measured before annealing with optical losses as low as 1.3, 0.3 and 1.5 ± 0.1 dB/cm at 638, 980 and 1550 nm, respectively for films varying in thickness from 300–650 nm. Annealing for 1 hour at 1000 °C in $N_2$ resulted in decreased thicknesses and increased refractive indices pointing towards film densification, and hydrogen removal. Post-annealing loss measurements show a decrease of 0.8 ± 0.1 dB/cm from 1.52–1.57 μm. We quantified surface roughness with AFM showing an RMS roughness of 1.0 ± 0.1 nm for unannealed and annealed films of varying optical losses. Annealing was shown to decrease the peak-peak roughness amplitude by 1.65 ± 0.40 nm. We verified hydrogen removal using ERDA and observed it to decrease from 17.2 to 22.6 at.% to < 0.1 at.% after annealing. RBS was used to investigate the atomic composition of the films and showed films of varying N/Si stoichiometry with high oxygen content ranging from 10.6% to 19.3%. Despite the films being non-stoichiometric $SiO_xN_y:H_z$ and having medium hydrogen incorporation, low optical losses were still achieved from the visible to L telecommunication band using low deposition pressures and temperatures. This opens the possibility for applying such films in integrated photonic devices, in particular for post-processing fabrication of such

devices on samples already containing temperature- or pressure-sensitive organic or metal layers. Future work aims to reduce the hydrogen incorporation in the films by reducing the $SiH_4$/Ar gas flow rate during deposition, to reduce and gain further insight into oxygen sources and bonding mechanisms in the films via FTIR, and characterize the stress in deposited $SiO_xN_y:H_z$ films.

### 3.5 References


1. Bauters, J.F.; Heck, M.J.R.; John, D.; Dai, D.; Tien, M-.; Barton, J.S.; Liense, A.; Heideman, R.G.; Blumenthal, D.J.; Bowers, J.E. Ultra-low-loss high-aspect-ratio $Si_3N_4$ waveguides. *Opt. Express* **2011**, *19*, 3163.
2. Bucio, T.D.; Khokhar, A.Z.; Lacava, C.; Stankovic, S.; Mashanovich, G.Z.; Petropoulos, P.; Gardes, F.Y. Material and optical properties of low-temperature $NH_3$ -free PECVD $SiN_x$ layers for photonic applications. *J. Phys. D Appl. Phys.* **2017**, *50*, 025106.
3. Blumenthal, D.J.; Heideman, R.G.; Geuzebroek, D.; Leinse, A.; Roeloffzen, C. Silicon Nitride in Silicon Photonics. *Proc. IEEE* **2018**, *106*, 2209–2231, doi:10.1109/jproc.2018.2861576
4. Gorin, A.; Jaouad, A.; Grondin, E.; Aimez, V.; Charette, P. Fabrication of silicon nitride waveguides for visible-light using PECVD: a study of the effect of plasma frequency on optical properties. *Opt. Express* **2008**, *16*, 13509–13516, doi:10.1364/oe.16.013509.
5. Gonzalvez, J.; Luna, R.; Tudanca, M.; Sánchez, O.; Albella, J.; Martinez-Duart, J. Plasma-enhanced chemically vapour deposited Si3N4 thin films for optical waveguides. *Thin Solid Films* **1992**, *220*, 311–314, doi:10.1016/0040-6090(92)90590-8.
6. Barrios, C.A.; Sánchez, B.; Gylfason, K.B.; Griol, A.; Sohlström, H.; Holgado, M.; Casquel, R. Demonstration of slot-waveguide structures on silicon nitride / silicon oxide platform. *Opt. Express* **2007**, *15*, 6846.
7. Muñoz, P.; Micó, G.; Bru, L.; Pastor, D.; Pérez, D.; Doménech, J.; Fernández, J.; Baños, R.; Gargallo, B.; Alemany, R.; Sánchez, A.M.; Ciera, J.M.; Mas, R.; Domínguez, C. Silicon nitride photonic integration platforms for visible, near-infrared and mid-infrared applications. *Sensors* **2017**, *17*, 2088.
8. Hosseini, E.S.; Yegnanarayanan, S.; Atabaki, A.H.; Soltani, M.; Adibi, A. High quality planar silicon nitride microdisk resonators for integrated photonics in the visible wavelength range. *Opt. Express* **2009**, *17*, 14543–14551, doi:10.1364/oe.17.014543.
9. Goykhman, I.; Desiatov, B.; Levy, U. Ultrathin silicon nitride microring resonator for biophotonic applications at 970 nm wavelength. *Appl. Phys. Lett.* **2010**, *97*, 30–32.
10. Khan, S.A.; Shi, Y.; Chang, C.-M.; Jan, C.; Fan, S.; Ellerbee, A.K.; Solgaard, O. Optical separation of heterogeneous size distributions of microparticles on silicon nitride strip waveguides. *Opt. Express* **2015**, *23*, 8855–8866, doi:10.1364/oe.23.008855.
11. Gaugiran, S.; Gétin, S.; Fedeli, J.M.; Colas, G.; Fuchs, A.H.; Chatelain, F.; Dérouard, J. Optical manipulation of microparticles and cells on silicon nitride waveguides. *Opt. Express* **2005**, *13*, 6956–6963, doi:10.1364/opex.13.006956.

12. Sharma, S.K.; Barthwal, S.; Singh, V.; Society, A.E.; Kumar, A. PECVD based silicon oxynitride thin films for nano photonic on chip interconnects applications PECVD based silicon oxynitride thin films for nano photonic on chip interconnects applications. *Micron* **2012**, *44*, 339–346.
13. Yota, J.; Hander, J.; Saleh, A.A. A comparative study on inductively-coupled plasma high-density plasma, plasma-enhanced, and low pressure chemical vapor deposition silicon nitride films. *J. Vac. Sci. Technol. A* **2000**, *18*, 372–376, doi:10.1116/1.582195
14. Dabos, G.; Manolis, A.; Giesecke, A.; Porschatis, C.; Chmielak, B.; Wahlbrink, T.; Pleros, N.; Tsiokos, D. TM grating coupler on low-loss LPCVD based Si3N4 waveguide platform. *Opt. Commun.* **2017**, *405*, 35–38, doi:10.1016/j.optcom.2017.07.088.
15. Krückel, C.J.; Fülöp, A.; Ye, Z.; Andrekson, P.A.; Torres-Company, V. Optical bandgap engineering in nonlinear silicon nitride waveguides. *Opt. Express* **2017**, *25*, 15370–15380.
16. Subramanian, A.; Neutens, P.; Dhakal, A.; Jansen, R.; Claes, T.; Rottenberg, X.; Peyskens, F.; Selvaraja, S.K.; Helin, P.; Du Bois, B.; et al. Low-Loss Singlemode PECVD Silicon Nitride Photonic Wire Waveguides for 532–900 nm Wavelength Window Fabricated Within a CMOS Pilot Line. *IEEE Photon- J.* **2013**, *5*, 2202809, doi:10.1109/jphot.2013.2292698.
17. Chiles, J.; Nader, N.; Hickstein, D.D.; Yu, S.P.; Briles, T.C.; Carlson, D.; Jung, H.; Shainline, J.M.; Diddams, S.; Papp, S.B.; et al. Deuterated silicon nitride photonic devices for broadband optical frequency comb generation. *Opt. Lett.* **2018**, *43*, 1527–1530, doi:10.1364/ol.43.001527.
18. Dergez, D.; Schalko, J.; Bittner, A.; Schmid, U. Fundamental properties of a-$SiN_x$:H thin films deposited by ICP-PECVD for MEMS applications. *Appl. Surf. Sci.* **2013**, *284*, 348–353.
19. Kshirsagar, A.; Nyaupane, P.; Bodas, D.; Duttagupta, S.; Gangal, S. Deposition and characterization of low temperature silicon nitride films deposited by inductively coupled plasma CVD. *Appl. Surf. Sci.* **2011**, *257*, 5052–5058, doi:10.1016/j.apsusc.2011.01.020.
20. Charifi, H.; Slaoui, A.; Stoquert, J.P.; Chaib, H.; Hannour, A. Opto-Structural Properties of Silicon Nitride Thin Films Deposited by ECR-PECVD. *World J. Condens. Matter Phys.* **2016**, *6*, 7–16, doi:10.4236/wjcmp.2016.61002.
21. Wu, A.M.; Yue, H.Y.; Zhang, X.; Qin, F.W.; Li, T.; Jiang, X. Synthesis and Its Characteristic of Silicon Nitride Film Deposited by ECR-PECVD at Low Temperature. *Mater. Sci. Forum* **2010**, *654–656*, 1712–1715, doi:10.4028/www.scientific.net/msf.654-656.1712.
22. Keita, A.-S.; Naciri, A.E.; Delachat, F.; Carrada, M.; Ferblantier, G.; Slaoui, A. Dielectric functions of Si nanoparticles within a silicon nitride matrix. *Phys. Status solidi (c)* **2010**, *7*, 418–422, doi:10.1002/pssc.200982461.
23. Bosco, G.B.F.; Khatami, Z.; Wojcik, J.; Mascher, P.; Tessler, L.R. Excitation mechanism of $Tb^{3+}$ in a- $Si_3N_4$:H under sub-gap excitation. *J. Lumin.* **2018**, *202*, 327–331.
24. Ortiz-Santos, A.; Ramos, C.; Sister-Hernández, J.; Santana, G.; Dutt, A.; Ortiz-Santos, A.; Ramos, C.; Sastré-Hernández, J.; Santana, G.; Dutt, A. White electroluminescence from SiNx thin films by a PECVD equipment using dichlorosilane precursor and study of emission mechanism. *Mater. Technol.* **2019**, *35*, 1–8, doi:10.1080/10667857.2019.1603185

25. Hiraki, T.; Aihara, T.; Nishi, H.; Tsuchizawa, T. Deuterated SiN/SiON Waveguides on Si Platform and Their Application to C-Band WDM Filters. *IEEE Photon- J.* **2017**, *9*, 1–7, doi:10.1109/jphot.2017.2731996.
26. Yamada, K.; Tsuchizawa, T.; Nishi, H.; Kou, R.; Hiraki, T.; Takeda, K.; Fukuda, H.; Ishikawa, Y.; Wada, K.; Yamamoto, T. High-performance silicon photonics technology for telecommunications applications. *Sci. Technol. Adv. Mater.* **2014**, *15*, 24603, doi:10.1088/1468-6996/15/2/024603.
27. Wright, D.N.; Marstein, E.S.; Holt, A. Effect of annealing on PECVD silicon nitride films. In Proceedings of the 22nd European Photovoltaic Solar Energy Conference, Milan, Italy, 3–7 September 2007.
28. Esposito, E.M.; Mercaldo, L.V.; Veneri, P.D.; Lancellotti, L.; Privato, C. Annealing effects on PECVD-grown Si rich aSiNx thin films. *Energy Procedia* **2010**, *2*, 159–164, doi:10.1016/j.egypro.2010.07.022.
29. Bakardjieva, V.; Beshkov, G.; Vitanov, P.; Alexieva, Z. Effect of rapid thermal annealing on the properties of μPCVD and PECVD silicon nitride thin films. *J. Optoelectron. Adv. Mater.* **2005**, *7*, 377–380.
30. Ay, F.; Aydinli, A. Comparative investigation of hydrogen bonding in silicon based PECVD grown dielectrics for optical waveguides. *Opt. Mater.* **2004**, *26*, 33–36.
31. Dabkowski, R.P. Installation of a New Electron Cyclotron Plasma Enhanced Chemical Vapour Deposition (ECR-PECVD) Reactor and a Preliminary Study of Thin Film Depositions. Master's Thesis, McMaster University, Hamilton, ON, Canada, 2011.
32. Miller, J.; Khatami, Z.; Wojcik, J.; Bradley, J.; Mascher, P. Integrated ECR-PECVD and magnetron sputtering system for rare-earth-doped Si-based materials. *Surf. Coatings Technol.* **2018**, *336*, 99–105, doi:10.1016/j.surfcoat.2017.08.051.
33. Wilson, P.R.; Roschuk, T.; Dunn, K.; Normand, E.N.; Chelomentsev, E.; Zalloum, O.H.; Wójcik, J.; Mascher, P. Effect of thermal treatment on the growth, structure and luminescence of nitride-passivated silicon nanoclusters. *Nanoscale Res. Lett.* **2011**, *6*, 168, doi:10.1186/1556-276X-6-168.
34. Miller, J. A novel approach to thin film deposition and rare-earth incorporation for silicon integrated photonics. Doctorate Thesis, McMaster University, Hamilton Ontario, Canada, **2020**.
35. Wörhoff, K.; Driessen, A.; Lambeck, P.; Hilderink, L.; Linders, P.; Popma, T. Plasma enhanced chemical vapor deposition silicon oxynitride optimized for application in integrated optics. *Sens. Actuators A Phys.* **1999**, *74*, 9–12, doi:10.1016/s0924-4247(98)00325-2.
36. Criado, D.; Pereyra, I.; Alayo, M.I. Study of nitrogren-rich silicon oxynitride films obtained by PECVD. *Mater. Charact.* **2003**, *50*, 161–171.
37. Lide, D.R. (Ed.) *CRC Handbook of Chemistry and Physics*; CRC Press LLC: Boca Raton, FL, USA, 2004; Volume 85.
38. Alayo, M.; Pereyra, I.; Scopel, W.; Fantini, M. On the nitrogen and oxygen incorporation in plasma-enhanced chemical vapor deposition (PECVD) SiOxNy films. *Thin Solid Films* **2002**, *402*, 154–161, doi:10.1016/s0040-6090(01)01685-6.
39. Hussein, M.; Worhoff, K.; Sengo, G.; Driessen, A. Optimization of plasma-enhanced chemical vapor deposition silicon oxynitride layers for integrated optics applications. *Thin Solid Films* **2007**, *515*, 3779–3786, doi:10.1016/j.tsf.2006.09.046.

# Chapter 4

## Silicon Nitride Waveguide Prototyping via Ultraviolet Laser Resist Mask Writing

Reprinted in part with open access permission from: D. B. Bonneville, M. A. Méndez-Rosales, H. C. Frankis, L. M. Gonçalves, R. N. Kleiman, and J. D. B. Bradley, "Flexible and low-cost fabrication of optical waveguides by UV laser resist-mask writing," Opt. Mater. Express **9**, 1728-1737 (2019). https://doi.org/10.1364/OME.9.001728

This chapter includes the findings presented in a published manuscript on UV laser resist mask writing for the fabrication of optical waveguides in $Si_3N_4$ thin films. Attention is given to the fabrication procedures and important considerations of using negative photoresist as a soft mask for etching waveguides. Factors such as UV exposure power, designed feature size, bake times and development are discussed with reference to SEM images and analysis of fabrication metrics such as minimum realized feature size and gap, power-dependent feature expansion, and sidewall line-edge roughness. The formation of optical waveguides was achieved via RIE in $Si_3N_4$ thin films on thermally oxidized Si wafers. A ring resonator, 50/50 directional coupler, and Sagnac loop interferometer were fabricated and measured to demonstrate the versatility of the fabrication process for arbitrary devices with flexible substrate choice. Sections added in the following thesis chapter that were not included in the published manuscript include a paragraph in 4.1.2. on developer storage and lifetime, Figure 4.4 and 4.5 which include SEM images of patterns defined in resist on $Al_2O_3$ and on Si, sentences added to 4.1.3. considering the deposition temperature of the cladding and reflow of the resist before etching, and a reorganization

of the sidewall analysis discussion from the fabrication section to the characterization section. These alterations were made to include details related to the repeatability and best practices of the process in a more instructional manner, demonstrate the versatility of the method by showing arbitrary pattern definition on a variety of materials, and better match the style of the thesis. This chapter demonstrates a flexible patterning technique which can be used on a variety of thin-films and substrates for the realization of photonic devices which a centralized theme to the thesis.

**Abstract:** We report on UV laser photoresist mask writing as a tool for fabricating integrated optical waveguides and devices. Using 375 nm laser light and a pneumatically controlled direct writing stage, we defined mask features into a 250-nm-thick negative photoresist layer on a silicon nitride film on an oxidized silicon substrate. We investigated the feature size and edge roughness for different laser powers. Using the photoresist mask layer and reactive ion etching, we patterned high-refractive-index-contrast silicon nitride strip waveguides and devices with varying waveguide widths and gaps. We report on the structural and transmission characteristics of a directional coupler, Sagnac interferometer, and ring resonator and demonstrate 50/50 coupling at 1510 nm, 20 dB transmission drop at 1580 nm, and a *Q* factor of ~13,000 at 1576 nm, respectively. These results demonstrate that this technique can be applied to a variety of thin film materials and substrates for inexpensive and rapid prototyping of integrated photonic devices.

## 4.1 Introduction

Direct writing has been demonstrated as a flexible tool for altering material properties and structuring at the nano and micro scale without the need of a physical mask. The use of continuous or pulsed lasers and electron beams has been applied to a variety of material

systems to fabricate integrated photonic devices [1,2]. Electron-beam lithography (EBL) has finer resolution in comparison to laser direct write techniques which is advantageous when fabricating features with sub-micrometer dimensions or close proximity [3]. Laser direct write (LDW) is low-cost in comparison to EBL, thus is often more accessible and desirable in the research environment where fast turnaround and rapid and inexpensive prototyping of devices is advantageous. Ultra-violet (UV) pulsed, continuous and interference LDW lithography has been demonstrated to utilize the photochemical response of various materials to permanently induce refractive index changes in order to pattern waveguides and other structures [4–13]. LDW lithography has also been shown to be a flexible platform for structuring photoresist waveguides and microfluidic channels with the use of chemical development for a variety of applications [14–18].

Nevertheless, most LDW research and development has focused on writing waveguide structures directly in the material. The resulting small refractive index change typically limits the selection of materials systems to low-refractive-index-contrast waveguides with large core sizes and bend radii, or alternatively, polymer waveguides. To enable the technique to be applied more widely to a variety of thin film photonic materials and substrates, UV LDW can be instead applied to define a photoresist mask layer on the chip, followed by pattern transfer to the layer below through selective etching. Many established and emerging low- to high-refractive-index-contrast waveguide systems have feature sizes achievable by LDW and their research and development could benefit from UV laser resist mask patterning [19–23].

Here, we demonstrate UV laser resist mask writing as a tool to pattern silicon nitride optical waveguides on silicon. We use a continuous UV LDW system to write features in

a negative photoresist layer on a silicon nitride ($Si_3N_4$) thin film to act as an etch mask for the definition of $Si_3N_4$ waveguides and devices. We investigate feature sizes, edge roughness and gaps versus UV writing parameters. Compared to other work with pulsed laser resist-mask writing [24] we show that smaller resolution is achievable using a UV laser written photoresist mask and that this method offers more flexibility in terms of material choice. The results presented here indicate that UV laser resist mask writing offers a good compromise between cost, resolution, and flexibility next to pulsed LDW and other laser resist-mask writing techniques for prototyping integrated photonic devices.

## 4.2 Fabrication

### 4.2.1 Maskless UV Exposure System

The exposure setup consists of a commercial tabletop patterning system which utilizes a 375 nm laser diode and focusing optics to write a predefined design onto a sample. The write-lens assembly utilizes pneumatic and piezo control with a telescopic lens to focus the beam to the scanning stage, which is mechanically controlled by a roller bearing and air bearing for independent *x*- and *y*-axis translation, respectively, during exposure. An internal processor automatically determines the scan speed and write time from run to run, which increases with exposed area. Figure 4.1 shows a diagram of the exposure setup including the UV laser and focusing optics, the mechanically-controlled vacuum stage for moving the sample and scattering of UV light within the photoresist layer. This scattering plays an important role in feature definition at the relatively higher energies that are required for negative photoresist exposure as compared to positive photoresists. Using negative photoresist also minimizes the area required for exposure, lowering the write time when compared to using positive photoresists in this process.

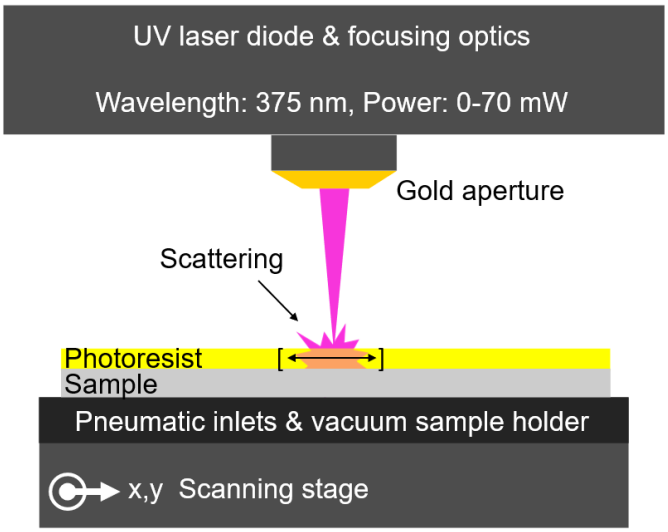


**Figure 4.1.** Diagram of the UV laser write system showing lateral UV light scattering during exposure of negative photoresist. The quoted system minimum feature size is 0.9 μm with 120 σ·nm edge roughness, an estimated write speed of 5 $mm^2$/minute, and output powers of 0–70 mW at 375 nm. The maximum substrate diameter is 10 cm.

### 4.2.2 Negative Resist Processing

We used the UV write setup to pattern a negative photoresist mask layer on a 7.5-cm-diameter silicon substrate with a 6-μm thermal $SiO_2$ layer and a 100-nm-thick low-pressure chemical vapor deposited (LPCVD) silicon nitride thin film. We selected NR7-250P negative photoresist, as the mask layer. Primer and the resist layer were spun on top of the substrate and material stack at 3000 rpm for 30 seconds. This leads to a 250-nm-thick resist layer which was then baked at 120°C for 3 minutes before UV exposure. After UV exposure, we baked the sample at 150°C for 5 minutes to harden the polymerized bonds and ensure high chemical contrast during development. We developed the sample at room temperature in a solution of 3:1 RD6 developer to deionized water for 10 seconds with manual agitation. The bake time prior to development

is subject to change depending on the substrate thermal conductivity, and exact chemistry and lifetime of the developer solution. Careful storage of developer solutions such as metal-ion containing TMAH-based solutions is imperative to ensuring a consistent fabrication process. All resists and developers undergo subtle changes after production over their lifetime, thus the optimal process parameters can also drift with regard to pre and post exposure bake and development times. It was noticed during this study that resists for negative developers react with ambient air to produce more bubbles and eventually a cloudy nature after aging significantly. It is recommended to calibrate the pre and post exposure bake steps with arbitrary pattern tests and spare test samples which mimic the actual samples to better control and understand the fabrication process before proceeding with longer dedicated device write times.

Standard GDSII layout software was used to create various designs, which are translated into the photoresist layer by the movement of the scanning stage during exposure. In this manner, maskless lithography is performed without the use of a virtual mask, and the UV laser writes the pattern directly into the photoresist layer. We defined straight waveguide features in the negative photoresist layer with designed widths varying from 0.6 to 1.4 μm and lengths of 2 cm using UV exposure powers ranging from 40 to 70 mW, as shown in Fig. 4.2. The designed waveguide features were rotated by 45° in order to simultaneously account for the resolution difference between each axis of movement by the independent air and roller bearings of the write stage during exposure. In order to fabricate waveguide designs in arbitrary *x* and *y* directions without any difference in resolution translating to the structure during exposure, we developed a high power write process whereby the resolution is limited by lateral scattering of UV light in the resist

layer. Higher exposure powers also ensure the feature edge roughness is dominated by optical scattering of the UV diode laser, rather than the mechanical motion of the stage. This methodology gives rise to a designed-to-fabricated feature increase, which has been characterized via scanning electron microscopy (SEM), as displayed in Fig. 4.2. Figure 4.2(a) demonstrates these results for waveguide features rotated by 45° relative to the write stage, showing the evolution of feature resolution at various exposure powers. Figures 4.2(b) and 4.2(c) show representative cross-sections of the resist mask profile after exposure and development of *y* axis straight and rotated features respectively.

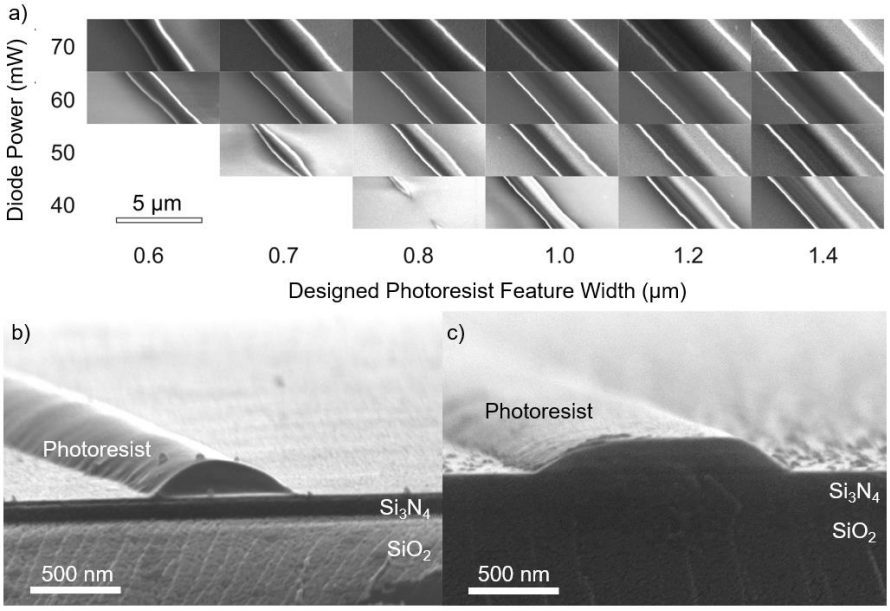


**Figure 4.2**. (a) Various widths of exposed and developed negative photoresist on $Si_3N_4$ films on thermally-oxidized silicon substrates. Features at narrow designed widths and lower energies demonstrate the *x*-*y* limitations of the stage's mechanical motion. (b) Resist feature cross section for 0.45 µm designed width exposed using only *y*-axis of stage motion at 70 mW. (c) Resist feature cross section for 0.65 µm designed width exposed using both x-y stage motion at 70 mW.

The width as measured from the SEM images in Fig. 4.2(a) are plotted in Fig. 4.3. As shown in Fig. 4.3, the minimum feature size increases with exposure power, and the relative feature expansion with respect to designed width is constant among different powers, varying from 2.1 μm at 50 mW to 2.2 μm at 70 mW.

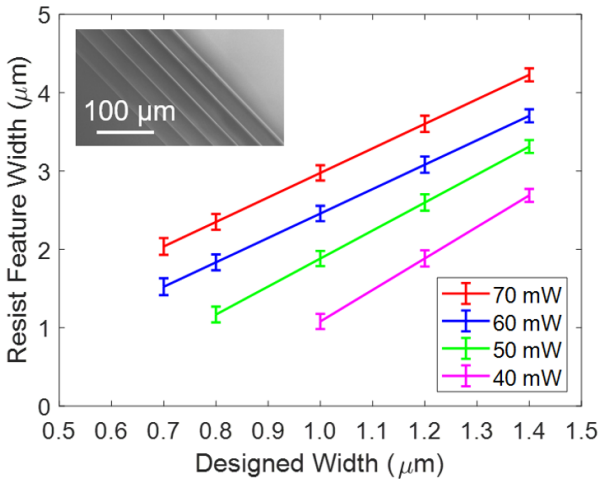


**Figure 4.3**. (a) Measured widths vs. designed width for photoresist features exposed at various laser diode powers. Inset: SEM of the 60 mW exposed set of features.

Characterizing the designed-to-exposed feature-width increase allows waveguides to be designed accounting for a nominal decrease in all feature sizes to achieve targeted dimensions. It is expected smaller features can be made than those shown by using designed widths below 0.6 μm, and solely exposing features using the *y* axis rather than *x* to utilize the finer control provided by the air bearing for *y* motion stage control, as shown in Fig. 4.2(b).

To further demonstrate the versatility in the write capabilities of the system, efforts were undertaken to use the fabrication process for designs on different substrates. Aluminium oxide was chosen as a candidate substrate due to its promise as a platform for waveguide amplifiers as discussed in Chapter 5, where identical steps were used to fabricate soft-

masks for etching, with results prior to etching and afterwards shown in Fig. 4.4a) and b) respectively. Wet chemical etching was carried out to fabricate waveguides, which demonstrated adhesion issues and had difficulty in the definition of smooth continuous sidewalls as shown in Fig. 4.4c)–d). It is anticipated primer layers may fix this in future work as well as additional reflow steps of the resist before etching. In addition, a variety of promotional campaigns for the CEDT were caried out, including using the process on silicon to celebrate the championship win of the Toronto Raptors in 2019, and the Movember campaign of 2020 as shown in Fig. 4.5, demonstrating the ability for the system to pattern arbitrary images as well as waveguide patterns.

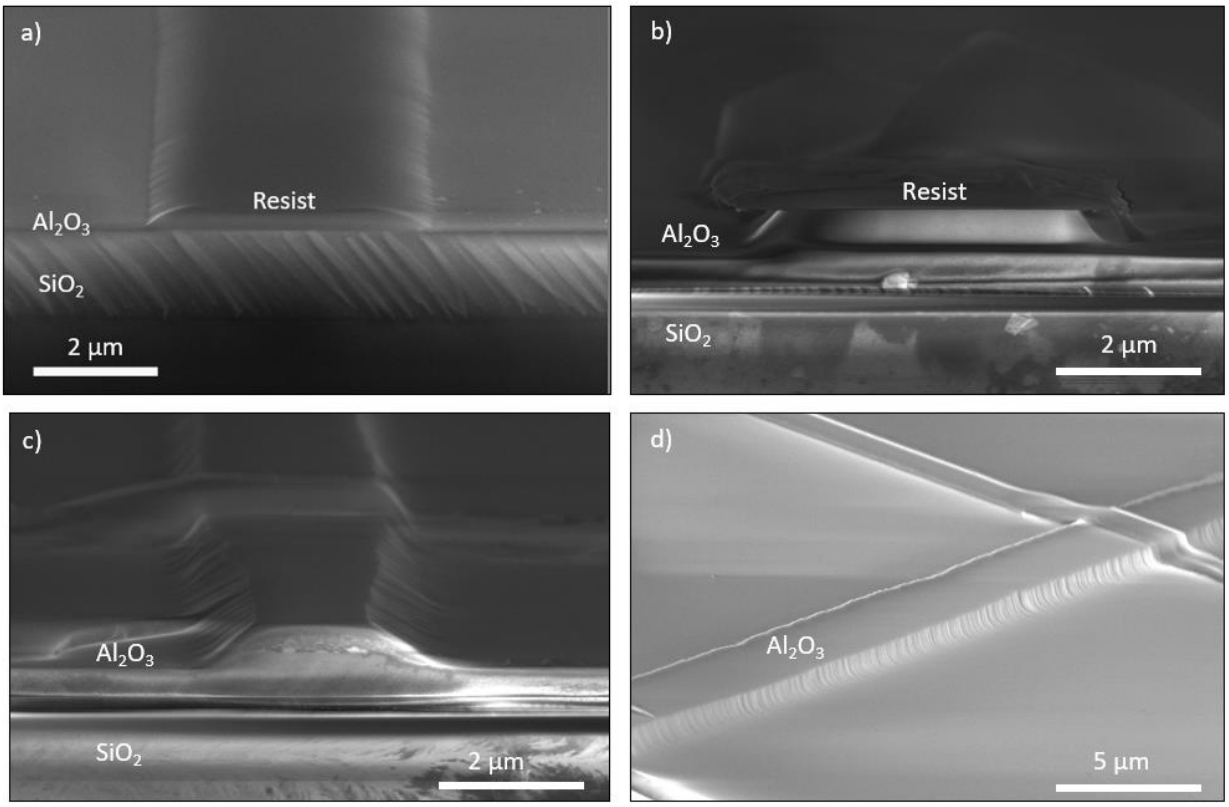


**Figure 4.4.** Soft-mask waveguide facet (a) before and (b) after wet-etching on $Al_2O_3$ fabricated with negative photoresist. (c) Final waveguide facet and (d) sidewalls fabricated in $Al_2O_3$ via UV mask writing and wet-chemical etching with visible resist mask adhesion failures.


**Figure 4.5**. Photoresist on Si for promotional samples created using the UV writing process.

### 4.2.3 $Si_3N_4$ Waveguide Etching via RIE

We selected UV laser powers of 60 and 70 mW to write mask features and pattern silicon nitride waveguides with varying widths and gaps. The exposures were carried out at 60 and 70 mW in order to optimize for sidewall roughness and smooth pattern transfer to the $Si_3N_4$ film layer as seen in Fig 4.2(a), which was found to be required for writing of straight

features in all directions in the *x*-*y* plane. To further smooth the sidewalls for waveguide pattern transfer during etching, a reflow step was carried out before RIE which consisted of a 120 °C 10-minute bake. This step also ensured strong adhesion of the polymer to the $Si_3N_4$ film layer. Varying gaps were studied to further investigate the patterning technique and its capability for fabricating waveguides with close proximity to one another. After defining the resist mask, we etched the $Si_3N_4$ film using reactive ion etching (RIE) with a $CF_4$-$O_2$ plasma. The etch parameters included gas flow rates of 22.5 sccm $CF_4$ and 2.5 sccm $O_2$ with 120 W of forward power at a pressure of 25 mTorr. The etching selectivity of $Si_3N_4$ to photoresist was determined to be 1.2:1.0 with a selectivity of 2:1 for $Si_3N_4$ to $SiO_2$. An etch time of 2 minutes was used with a 60 nm/min $Si_3N_4$ etch rate to ensure an etch depth of 100 nm. After stripping the resist in acetone and cleaning in isopropyl alcohol, a 1.8-µm-thick plasma-enhanced chemical vapour deposited (PECVD) $SiO_2$ film was deposited on top of the $Si_3N_4$ waveguides with 25 sccm $O_2$ and 2.5 sccm $SiH_4$/Ar (70/30 % dilute) at 2.5 mTorr with 500 W forward power. The deposition temperature was 140 °C, demonstrating the ability to deposit on thermally sensitive substrates which may break down at temperature above 200 or 400 °C such as those that include polymers or metal contact layers. After top cladding deposition the sample was cleaved to form end facets. The fabrication steps are shown in Fig. 4.6, as well as the electric field profile of the fundamental transverse electric (TE) mode at 1550 nm wavelength, calculated using a finite element method (FEM) modesolver as discussed in section 2.2.1.2.

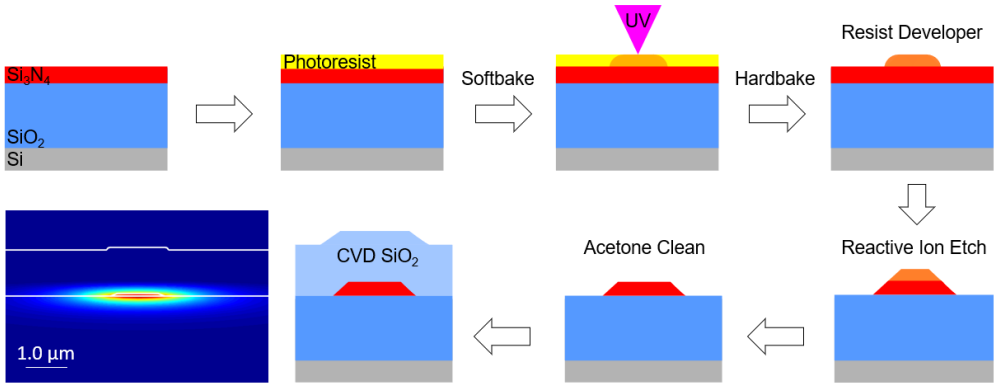


**Figure 4.6.** $Si_3N_4$ waveguide fabrication steps and calculated electric field profile of the fundamental TE mode at 1550 nm for a 1.6 µm × 0.1 µm $Si_3N_4$ strip waveguide.

SEM images of fabricated waveguides prior to top-cladding deposition are shown in Fig. 4.7. Figure 4.7(a) shows a top-down view of a variety of $Si_3N_4$ waveguides with varying designed widths and gaps at 70 mW exposure power. Figures 4.7(b) and 4.7(c) show SEM waveguide cross-section images for single, and adjacent waveguides respectively. It can be seen that the minimum gap starts to close at designed gap widths of 4.0, 5.2 and 5.8 µm for designed waveguide widths of 0.7, 0.8 and 1.0 µm, respectively. The gap width after fabrication versus the designed gap is plotted in Fig. 4.8 for write powers of 60 and 70 mW. The realized gap width is influenced by the combined effects of stage motion resolution, exposure-power-dependent waveguide width expansion, and designed gap width collectively. By selecting the correct write parameters, minimum gaps in the range of 1–2 µm are possible. It is observed by comparing identical designed waveguide widths, that on average ~170 nm smaller gaps are achievable with 70 mW exposure powers compared to 60 mW, with larger designed gaps required to compensate for the feature increase at higher powers.

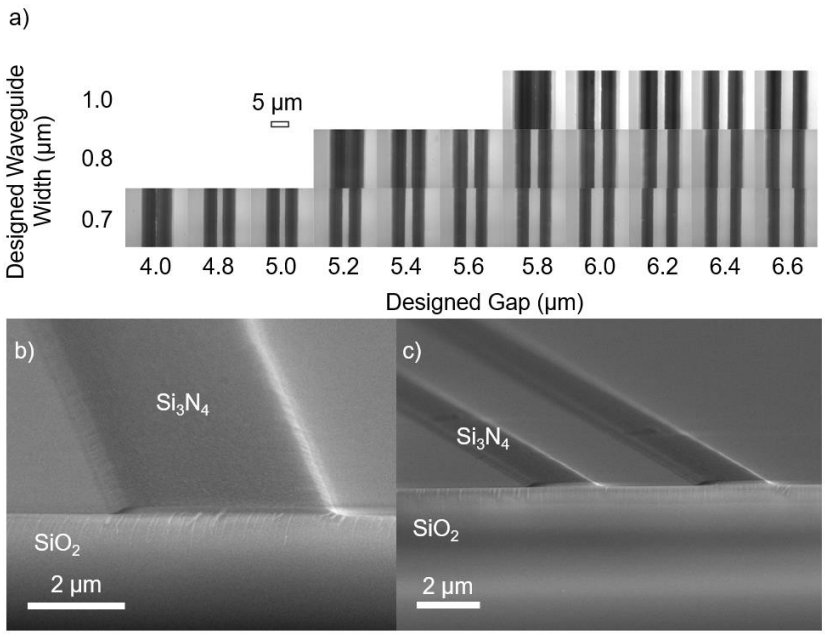


**Figure 4.7.** (a) Various fabricated $Si_3N_4$ waveguides with increasing width and gap demonstrating gap resolution at 70 mW exposure power. (b) Final fabricated $Si_3N_4$ waveguide cross section for a 0.7 μm designed width waveguide fabricated using 70 mW UV laser power. (c) Parallel fabricated waveguides in a coupler region for 0.7 μm designed widths at 70 mW with a designed gap of 5 μm.

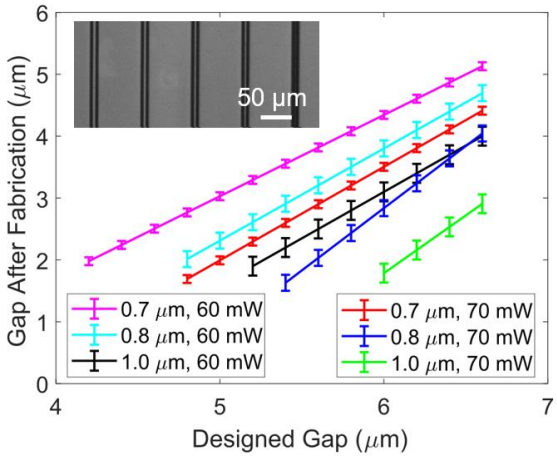


**Figure 4.8.** Measured gaps between fabricated waveguides of varying designed widths at 60 and 70 mW exposure powers. The measured waveguide widths are 2.1–2.8, 2.9–3.3 and 3.3–3.9 μm at 60 mW and 3.0–3.6, 3.4–4.1 and 4.1–4.7 μm at 70 mW for 0.7, 0.8 and 1.0 μm designed widths, respectively. Inset SEM image of waveguides with 1.0 and 7.0–6.2 μm designed width and gap respectively, with 70 mW exposure power.

An understanding of the width and gap resolutions using the demonstrated methodology enabled the design of various proof-of-concept passive waveguide structures for test. We selected standard passive integrated optical components, including a directional coupler, ring resonator and Sagnac loop mirror [25]. Waveguide mode and bend loss simulations were carried out to determine a minimum bending radius of 300 μm, which was chosen for a point coupled ring resonator, as well as supermode analysis [26] to discover a coupling length of 40 μm for a single mode 50/50 splitter at 1550 nm both based on a waveguide width of 1.6 and a gap of 1.1 μm. The coupling region of the Sagnac loop mirror was based on and identical to the included 50/50 splitter, with a loop radius identical to the ring resonator. These feature sizes were achieved using 70 mW exposure powers and designed widths and gaps of 0.7 μm and 2.8 μm respectively. We note that even smaller feature sizes in the straight sections and

designed gaps than those shown in Fig. 4.3 and Fig. 4.8 were achieved due to the independent use of the *y* axis during exposure of the waveguides lengthwise, and resolution-limited *x* axis motion of the roller bearing for gap formation. By keeping the coupler gaps parallel with respect to the *y* axis rather than rotated, it is expected that smaller gaps than those shown here can be achieved. Variations in designed widths to compensate for varying axis resolution for bent waveguides can also be considered.

## 4.3 Characterization

### 4.3.1 Sidewall Line-edge Roughness via SEM

To quantify the line-edge roughness (LER) in units of σ·nm, image processing was used on SEM images of waveguide resist masks following the methodology provided by [27] to express the area of saturated pixels surrounding each straight line as LER in units comparable to, and values below the quoted system specifications mentioned in Fig. 4.1. For the formation of features which are dominated by UV scattering as opposed to mechanical stage motion, it was concluded that higher powers of 60 and 70 mW are required during exposure. As seen in Fig. 4.9, 40 and 50 mW demonstrate significantly higher edge roughness at smaller designed widths, which we attribute to stage motion, whereas 60 and 70 mW show relatively width-independent LER, expected by a scattering dominated process.

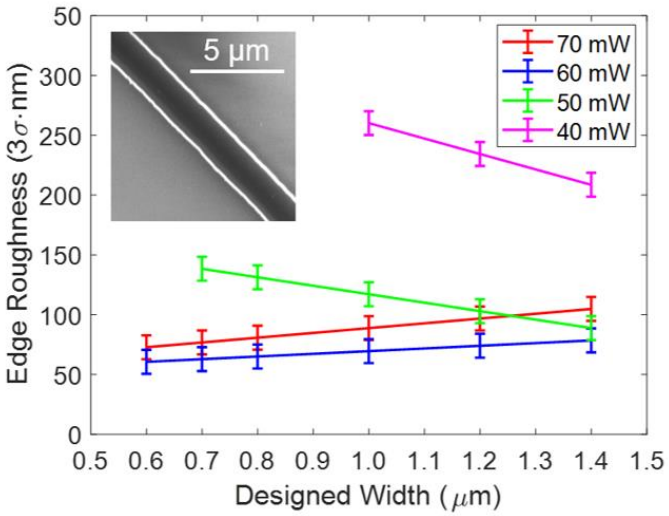


**Figure 4.9.** Calculated edge roughness vs. designed width exposed at various laser diode powers. Inset: SEM of resist feature for 0.8 μm designed width and 60 mW exposure power.

After analyzing the edge roughness, it is clear that operating above a certain power threshold is desirable for the formation of smooth sidewalls. It was therefore concluded in order to ensure the smallest features, gaps and smoothest sidewalls an exposure power of 70 mW would be used for the formation of waveguides and integrated photonic devices.

### 4.3.2 Waveguide Device Measurements

We measured the transmission spectra of the waveguides and devices using an edge coupling setup. The setup included a tunable 1510–1640 nm laser source, polarization maintaining fiber paddles for selecting TE polarization, lensed input and output fibers with 2.5-μm spot size for coupling to and from the chip and a photodetector for measuring the transmitted signal. Figure 4.10 shows the overall footprint of the fabricated devices as well as each coupling region prior to cladding revealing waveguide coupling gaps of 1.1, 2.1, and 1.5 μm for the Sagnac loop, directional coupler, and ring resonator respectively. Figure 4.11(a) shows the transmission spectra for each arm of the directional coupler

which was measured with a fixed input arm and output to a through and cross port to measure the coupled power from 1510–1580 nm. As seen from the transmission spectra in Fig. 11(a), a 50/50 splitting ratio is achieved at 1510 nm, shown by the similar signal powers. Figure 4.11(b) shows the transmission spectra for the Sagnac loop interferometer, demonstrating a 20 dB extinction ratio (ER) at 1580 nm, where the directional coupler is operating as a 50/50 splitter, causing the reflection of light. Figure 4.11(c) shows the transmission spectra for the ring resonator demonstrating resonances from 1510–1580 nm, with a wavelength-dependent ER ranging from 0.5 to 0.9 dB and a free spectral range (FSR) of ~1 nm. Note the measured insertion loss includes fiber loss, fiber-chip coupling loss and waveguide loss not subtracted from the measurements. A Lorentzian fit of a resonant dip is included in Fig. 4.11(d) at 1576 nm which was used to characterize and extract an internal quality factor of ~13,000, assuming the ring is under coupled due to the large gap and small ER.

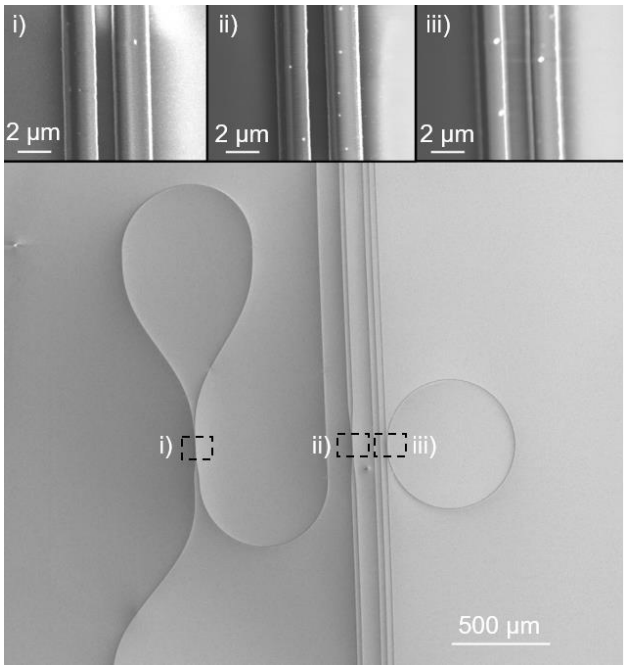


**Figure 4.10.** SEM images of total footprint (bottom) and coupling regions (top) for $Si_3N_4$ integrated optical devices fabricated using UV laser resist mask patterning. (i) 300-µm-radius Sagnac loop interferometer with 40 µm coupling length and width (*w)* and gap (*g)* of 1.9 and 1.1 µm respectively. (ii) Directional coupler with 40 µm coupling length and fabricated *w* and *g* of 2.1 and 1.1 µm respectively. (iii) 300-µm-radius point coupled ring resonator with *w* and *g* of 1.6 and 1.5 µm respectively.

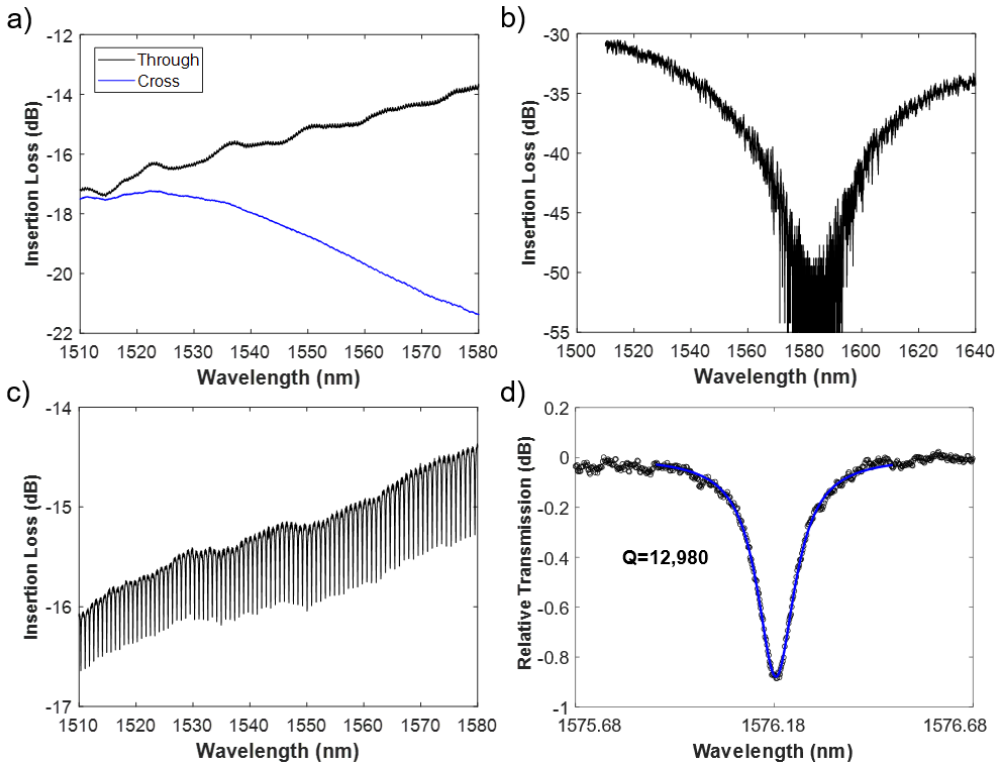


**Figure 4.11.** Transmission spectra for $Si_3N_4$ integrated optical devices fabricated using UV laser resist mask patterning. (a) Directional coupler showing 50/50 coupling at 1510 nm for 40 μm coupling length. (b) 300-μm-radius Sagnac loop interferometer with repeated coupler length, demonstrating a 20 dB extinction ratio at ~1580 nm (c) 300-μm-radius point coupled ring resonator. (d) Lorentzian resonance fit demonstrating a *Q* of 12,980 at 1576.2 nm.

Based on these proof-of-concept results, we propose that various waveguiding structures and photonic devices can be readily prototyped using this process. Investigation of UV patterning of additional resist mask materials, optimization of the resist processing (e.g. thickness and bake times) and improved waveguide etch recipes can lead to lower waveguide losses and higher *Q* factor resonators. This technique is also promising for post-processing of novel device layers with relaxed feature size and

alignment tolerances onto existing photonic integration platforms for new functionalities (e.g. in silicon photonic microsystems).

## 4.4 Conclusion

We introduced UV laser resist-mask patterning as a low-cost prototyping technique for the development of integrated optical waveguides and devices. Using a continuous UV laser source to pattern a negative photoresist etch mask, we defined waveguides in a silicon nitride thin film on silicon. We performed dose tests and characterized the negative resist features to measure the increase in designed feature dimensions and quantify the edge roughness. The gap resolution was also investigated before fabricating various devices to ensure minimum spacing between adjacent waveguides is achievable. We discovered that higher energy exposures with scattering-limited sidewall roughness is ideal for negative photoresist development for high contrast, straight, smooth sidewalls. A directional coupler, Sagnac interferometer and ring resonator were fabricated and measured demonstrating 50/50 coupling at 1510 nm, 20 dB drop at 1580 nm, and a Q factor of ~13,000 at 1576 nm respectively. The ability to prototype passive optical components was demonstrated with promise towards applying the patterning technique to a wide variety of applications and material systems.

## 4.5 References

1. R. R. Gattass and E. Mazur, “Femtosecond laser micromachining in transparent materials,” Nat. Photonics **2**(4), 219–225 (2008).
2. Y. Huang, G. T. Paloczi, A. Yariv, C. Zhang, and L. R. Dalton, “Fabrication and replication of polymer integrated optical devices using electron-beam lithography and soft lithography,” J Phys Chem B. **108**(25), 8606–8613 (2004).
3. T. Barwicz, M. A. Popovic, P. T. Rakich, M. R. Watts, H. A. Haus, E. P. Ippen, and H. I. Smith, “Microring-resonator-based add-drop filters in SiN: fabrication and analysis,” Opt. Express **12**(7), 1437–1442 (2004).
4. R. R. Krchnavek, G. R. Lalk, and D. H. Hartman, “Laser direct writing of channel waveguides using spin-on polymers,” J. Appl. Phys. **66**(11), 5156–5160 (1989).

5. L. Eldada, C. Xu, K. M. T. Stengel, L. W. Shacklette, and J. T. Yardley, “Laser-fabricated low-loss single-mode raised-rib waveguiding devices in polymers,” J. Lightwave Technol. **14**(7), 1704–1713 (1996).
6. M. Rosenberger, B. Schmauss, and R. Hellmann, “UV-writing of a superstructure waveguide Bragg grating in a planar polymer substrate,” Sensors **17**(9), 1964 (2017).
7. J. Missinne, A. Vasiliev, A. Elmogi, N. Teigell Beneitez, E. Bosman, B. Van Hoe, and G. Van Steenberge, “Bragg grating sensors in laser-written single mode polymer waveguides,” Procedia Eng. **120**, 878–881 (2015).
8. M. Svalgaard, “Direct writing of planar waveguide power splitters and directional couplers using a focused ultraviolet laser beam,” Electron. Lett. 33(**20**), 1694–1695 (1997).
9. G. D. Marshall, P. Dekker, M. Ams, J. A. Piper, and M. J. Withford, “Directly written monolithic waveguide laser incorporating a distributed feedback waveguide-Bragg grating,” Opt. Lett. **33**(9), 956–958 (2008).
10. S. Pelli, G. C. Righini, A. Scaglione, M. Guglielmi, and A. Martucci, “Direct laser writing of ridge optical waveguides in silica-titania glass sol-gel films,” Opt. Mater. **5**(1–2), 119–126 (1996).
11. M. Svalgaard, C. V. Poulsen, A. Bjarklev, and O. Poulsen, “Direct UV writing of buried single mode channel waveguides in Ge-doped silica films,” Electron. Lett. **30**(17), 1401–1403 (1994).
12. E. Zgraggen, I. Murat Soganci, F. Horst, A. La Porta, R. Dangel, B. J. Offrein, S. A. Snow, J. K. Young, B. W. Swatowski, C. M. Amb, O. Scholder, R. Broennimann, U. Sennhauser, and G.-L. Bona, “Laser direct writing of single-mode polysiloxane optical waveguides and devices,” J. Lightwave Technol. **32**(17), 3036–3042 (2014).
13. G. D. Marshall, M. Ams, and M. J. Withford, “Direct laser written waveguide-Bragg gratings in bulk fused silica,” Opt. Lett. **31**(18), 2690–2691 (2006).
14. M. Dubov, S. R. Natarajan, J. A. R. Williams, and I. Bennion, “Mask-less lithography for fabrication of optical waveguides,” Proc. SPIE **6881**, 688110 (2008).
15. V. Vaidyanathan and S. Wang, “A maskless fabrication approach of integrated optical waveguides for engineering technology students,” presented at the American Society for Engineering Education Annual Conference & Exposition, Chicago, Illinois, 18–21 June 2006.
16. J. C. Dingeldein, *Direct Write Fabrication of Waveguides and Interconnects for Optical Printed Wiring Boards* (Ph.D. Thesis, Michigan Technological University, 2012).
17. K. Kruse and C. Middlebrook, “Laser-direct writing of single mode and multi-mode polymer step index waveguide structures for optical backplanes and interconnection assemblies,” Photonics Nanostruct. Fundam. Appl. **13**, 66–73 (2015).
18. H. Hartwig, E. Sergeeva, N. Thomas, and D. Hohlfeld, “Precision laser direct writing of polymer optical waveguides and optofluidic systems,” in DGaO Proceedings (The German Branch of the European Optical Society, 2016), A16.

19. M. Belt, M. L. Davenport, J. E. Bowers, and D. J. Blumenthal, “Ultra-low-loss $Ta_2O_5$-core/$SiO_2$-clad planar waveguides on Si substrates,” Optica **4**(5), 532–536 (2017).
20. K. Wörhoff, J. D. B. Bradley, F. Ay, D. Geskus, T. P. Blauwendraat, and M. Pollnau, “Reliable low-cost fabrication of low-loss $Al_2O_3$:$Er^{3+}$ waveguides with 5.4-dB optical gain,” IEEE J. Quantum Elec. **45**(5), 454–461 **(**2009).
21. S. A. Vázquez-Córdova, M. Dijkstra, E. H. Bernhardi, F. Ay, K. Wörhoff, J. L. Herek, S. M. García-Blanco, and M. Pollnau, “Erbium-doped spiral amplifiers with 20 dB of net gain on silicon,” Opt. Express **22**(21), 25993–26004 (2014).
22. J. F. Bauters, M. J. R. Heck, D. D. John, M.-C. Tien, W. Li, J. S. Barton, D. J. Blumenthal, J. E. Bowers, A. Leinse, and R. G. Heideman, "Ultra-low-loss single-mode $Si_3N_4$ waveguides with 0.7 dB/m propagation loss," in *37th European Conference and Exposition on Optical Communications*, OSA Technical Digest, OSA Technical Digest (CD) (Optical Society of America, 2011), paper Th.12.LeSaleve.3.
23. G. C. Righini and A. Chiappini, “Glass optical waveguides: a review of fabrication techniques,” Opt. Eng. **53**(7), 071819 (2014).
24. A. Kiani, K. Venkatakrishnan, B. Tan, and V. Venkataramanan, “Maskless lithography using silicon oxide etch- stop layer induced by megahertz repetition femtosecond laser pulses,” Opt. Express **19**(11) 10834–10842 (2011).
25. Y. Zhang, S. Yang, H. Guan, A. E.-J. Lim, G.-Q. Lo, P. Magill, T. Baehr-Jones, and M. Hochberg, “Sagnac loop mirror and micro-ring based laser cavity for silicon-on-insulator,” Opt. Express **22**(15), 17872–17879 (2014).
26. L. Chrostowski and M. Hochberg, *Silicon Photonics Design: From Devices to Systems* (Cambridge University Press, 2015).
27. J. R. Bickford, “Automatic stripe analysis tool” (Army Research Laboratory, Report No. ARL-TR-6469, 2013). https://www.arl.army.mil/arlreports/2013/technical-report.cfm?id=6765

# Chapter 5

## Co-Doped Erbium Ytterbium Aluminium Oxide Waveguides for Optical Amplifiers

Reprinted in part with open access permission from: Dawson B. Bonneville, Henry C. Frankis, Renjie Wang, and Jonathan D. B. Bradley, "Erbium-ytterbium co-doped aluminium oxide waveguide amplifiers fabricated by reactive co-sputtering and wet chemical etching," Opt. Express 28, 30130-30140 (2020). https://doi.org/10.1364/OE.402802

This chapter includes the findings presented in a published manuscript on the fabrication and characterization of co-doped $Al_2O_3$:$Er^{3+}$:$Yb^{3+}$ waveguide amplifiers. The films are prepared via reactive magnetron co-sputtering and patterned with conventional contact lithography and wet chemical etching. Film loss measurements are used to calibrate the deposition process using prism coupling. SEM is used to investigate patterned waveguides and optimize the fabrication procedure. Waveguides were fabricated and measured demonstrating low-loss at ~980 and ~1530 nm wavelengths in interest of optical amplification. Internal net gain is demonstrated from ~1530–1570 nm via optical pumping at 976 nm using a fiber-edge coupled setup. The following chapter highlights these findings in detail alongside takeaways from the fabrication process and etching procedure. Sections which were included in the following thesis chapter but not in the published manuscript include discussions in 5.2.2 on the specifics for the etching procedure set up and variation in etch rates, as well as takeaways from process optimization and wet-chemical etching using $H_3PO_4$. This includes the addition of figures

2 and 3 and were added to give the chapter more instructional content for the reader. This chapter demonstrates an application of versatile and low-cost fabrication techniques for the realization of active devices in a rare earth integrated material which is a centralized theme to the thesis.

**Abstract:** We report on the fabrication and optical characterization of erbium-ytterbium co-doped aluminum oxide ($Al_2O_3$:$Er^{3+}$:$Yb^{3+}$) waveguides using low-cost, low-temperature deposition and etching steps. We deposited $Al_2O_3$:$Er^{3+}$:$Yb^{3+}$ films using reactive co-sputtering, with $Er^{3+}$ and $Yb^{3+}$ ion concentrations ranging from 1.4 – 1.6 × $10^{20}$ and 0.9 – 2.1 × $10^{20}$, respectively. We etched ridge waveguides in 85 % pure phosphoric acid at 60°C, allowing for structures with minimal polarization sensitivity and acceptable bend radius suitable for optical amplifiers and avoiding alternative etching chemistries which use hazardous gases. Scanning-electron-microscopy (SEM) and profilometry were used to assess the etch depth, sidewall roughness, and facet profile of the waveguides. The $Al_2O_3$:$Er^{3+}$:$Yb^{3+}$ films exhibit a background loss as low as 0.2 ± 0.1 dB/cm and the waveguide loss after structuring is determined to be 0.5 ± 0.3 dB/cm at 1640 nm. Internal net gain of 4.3 ± 0.9 dB is demonstrated at 1533 nm for a 3.0 cm long waveguide when pumped at 970 nm. The material system is promising moving forward for compact Er-Yb co-doped waveguide amplifiers and lasers on a low-cost silicon wafer-scale platform.

## 5.1 Introduction

Erbium-doped devices have become a cornerstone in the telecommunications industry, first by seeing their spotlight in erbium doped fiber amplifiers and lasers [1], and now by continuing their development into photonic integrated circuits (PICs). Recently, on-chip rare-earth doped waveguide amplifiers and lasers (REDWAs and REDWLs) have been

shown to offer advantages when it comes to power output and stability [2] in comparison to other silicon compatible optical amplifiers and lasers including those based on III-V materials or other processes such as stimulated Raman scattering. When integrated into a silicon platform, many doors are opened for REDWAs and REDWLs in chip scale applications needing compact optical amplifiers and lasers [2–4] for not only telecommunications, but also biological and environmental sensing [5].

Various glass rare-earth host materials are available with suitable lanthanide solubilities which can be patterned and integrated with a silicon substrate. Among these, aluminum oxide has demonstrated itself as a platform for rare earth amplifiers and lasers [2–4, 6–9] based on its high transparency, high rare earth solubility, high chemical and mechanical stability and moderate refractive index contrast for compact devices. Waveguide fabrication methods have been well-established using reactive co-sputtering deposition and reactive ion etching [6,10,11]. Net optical gain of 2.0 dB/cm has been demonstrated in $Al_2O_3$:$Er^{3+}$ waveguide amplifiers [8], as well as 20 dB net gain for 12.9 and 24.4 cm long $Al_2O_3$:$Er^{3+}$ spiral waveguides [3] when pumped at 980 and 976 nm respectively, and up to 4 dBm of on chip optical signal power. To achieve higher gain per unit length various strategies such as slot waveguides and atomic layer deposition have been applied [9] which have shown 20.1 dB/cm optical gain in a 250 μm long waveguide showing promise for ultra-compact devices.

To improve the pump absorption and efficiency in compact amplifier and lasers while likewise allowing for low-loss waveguide structures, $Yb^{3+}$ ions have been suggested as a co-dopant in the optical host matrix. $Yb^{3+}$ ions have a peak absorption cross section one order of magnitude larger than $Er^{3+}$ ions and absorption spectrum spanning from 850–

1000 nm, providing increased likelihood of absorption for pump light [13,14]. The $^2F_{5/2}$ excited state of the $Yb^{3+}$ ions resonantly provides energy to the $^4I_{11/2}$ level of the $Er^{3+}$ ions increasing the pumping efficiency by sensitizing the energy conversion process. The enhanced pump absorption can lead to higher signal output powers [15], and ytterbium's broad absorption around 940 nm has been proposed as a route to temperature insensitive pumping [16]. Additionally, increasing the $Er^{3+}$ dopant concentration can lead to higher optical gain, but due to clustering and fast quenching [17] of the ion emissions, optical gain in singly-doped $Al_2O_3$:$Er^{3+}$ amplifiers is limited. It is therefore of interest to fabricate $Al_2O_3$:$Er^{3+}$:$Yb^{3+}$ waveguide amplifiers with low material losses which from fiber simulations and film work also suggest to potentially mitigate the effects from rare-earth clustering sites [14, 15–19].

Fabricating $Al_2O_3$:$Er^{3+}$:$Yb^{3+}$ waveguide amplifiers in a low-cost, low-temperature and low environmental impact manner is of interest as it continues to grow as an emerging technology. $Al_2O_3$:$Er^{3+}$:$Yb^{3+}$ waveguides on silicon have been demonstrated using different deposition methods, including ion implantation of sputtered $Al_2O_3$ films [13,14] and middle frequency sputtering, which achieved 5.2 dB/cm net gain in a 10.5 mm long waveguide [20]. However, these methods both required high temperature annealing to obtain high optical quality thin films. Although a fine control of morphology is available with Atomic Layer Deposition (ALD) [21,22] its lower deposition rates, higher cost, and lack of process flexibility is less attractive for deposition of thick gain layers (1.0 μm). For these reasons, we have utilized reactive magnetron co-sputtering where individual Er, Yb and Al sputtering targets are placed in a chamber with ambient $O_2$ and Ar. In this manner, the purity of the rare-earth targets can be controlled, doping of the gain layer can be

carried out in-situ at relatively low temperature and relatively fast deposition rates can lead to thick films with homogenous doping profiles. To structure the films, we utilize wet chemical etching in order to avoid the use of chlorine-bromine gas chemistries [10]. Phosphoric acid (85 m.%) was selected for its low cost, availability, and relatively safe nature when diluted [11]. This process allows for the use of conventional contact lithography and is well-suited to typical dimensions employed in rare-earth-doped $Al_2O_3$ amplifiers and lasers [3,12]. Here, our fabrication process is reported and characterized as well as the material properties and optical gain results for co-doped $Al_2O_3$:$Er^{3+}$:$Yb^{3+}$ waveguides.

## 5.2 Fabrication

### 5.2.1 Reactive RF Magnetron Co-Sputtering of Er:Yb:$Al_2O_3$

We deposited $Al_2O_3$:$Er^{3+}$:$Yb^{3+}$ films via reactive magnetron sputtering on three-inch silicon substrates with 6 µm of thermally grown silicon dioxide. Three-inch metallic aluminum, erbium and ytterbium targets of 99.999, 99.9 and 99.9% purity, respectively, were co-sputtered in an argon/oxygen ambient. To improve the quality and optical loss of the films the substrate is heated during depositions by a heating element and is backed by an RF substrate bias to provide thermal/kinetic energy into the films. The dopant concentrations were controlled by selecting the sputtering power applied to the erbium and ytterbium targets and measured using Rutherford backscattering spectrometry (RBS) at Western University's Tandetron facilities. The concentrations were determined based on RBS measurements in singly-doped calibration films deposited using identical Er or Yb sputtering powers because it was difficult to resolve the separate Er and Yb RBS signals in the co-doped films. The concentrations in the co-doped films were verified in absorption measurements and based on the known Er and Yb absorption cross sections [17]. A

design of experiments was carried out to obtain high-quality optical films based on the work of Magden et al. on $Al_2O_3:Er^{3+}$ films using a similar deposition system [4]. We note that further optimization of the deposition process can lead to better film properties and losses, particularly at lower wavelengths and work in this direction is on-going. The deposition parameters for the three $Al_2O_3:Er^{3+}:Yb^{3+}$ films specifically selected for waveguide experiments are outlined in Table 5.1 as well as the measured $Er^{3+}$ and $Yb^{3+}$ ion concentrations from singly-doped calibration RBS measurements. A diagram of the deposition chamber can be seen in Fig. 5.1 (a).

**Table 5.1.** $Al_2O_3:Er^{3+}:Yb^{3+}$ film deposition parameters

| Deposition parameters | | Film 1 | Film 2 | Film 3 |
|---|---|---|---|---|
| Gas flow rate | Argon (sccm) | 100 | 100 | 100 |
| | Oxygen (sccm) | 3.35 | 3.4 | 3.4 |
| Sputtering power | Aluminum (W) | 230 | 200 | 200 |
| | Erbium (W) | 29 | 25 | 25 |
| | Ytterbium (W) | 40 | 25 | 30 |
| Substrate conditions | Deposition temperature (°C) | 450 | 400 | 400 |
| | Substrate bias power (W) | 70 | 70 | 70 |
| | Deposition time (min) | 150 | 165 | 165 |
| Vacuum conditions | Process pressure (mTorr) | 1.6 | 2.0 | 2.0 |
| Concentrations from RBS [Er / Yb] ($10^{20}$ $cm^{-3}$) | | 1.4 / 1.2 | 1.4 / 1.3 | 1.4 / 2.1 |
| Refractive index & thickness from VASE (nm) | | 1.616 / 1068 | 1.620 / 980 | 1.624 / 927 |

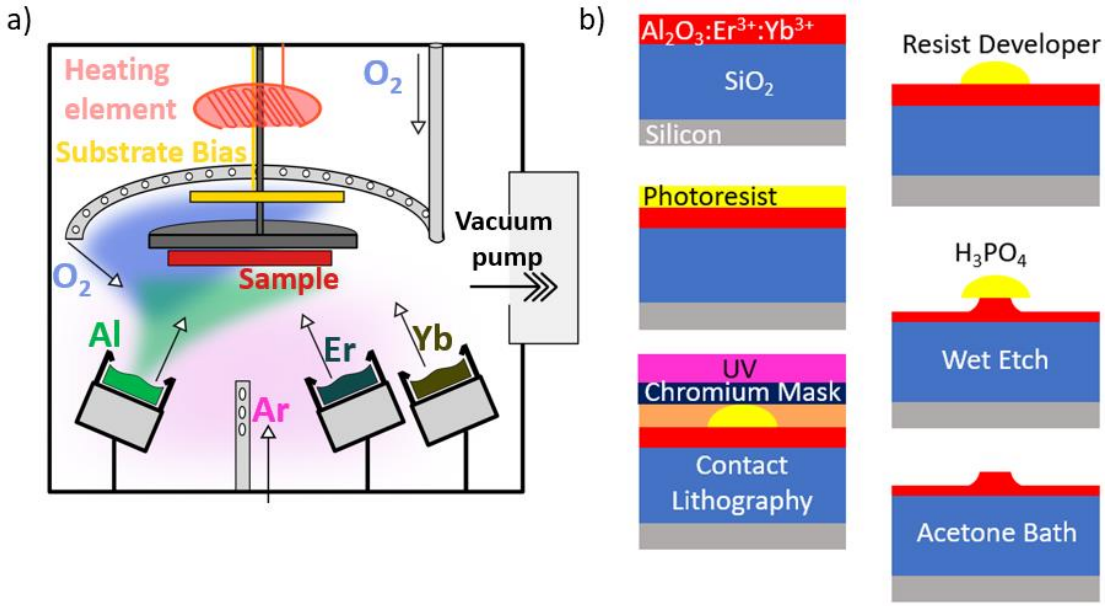


**Figure 5.1.** (a) Diagram of sputter deposition chamber showing 3 RF magnetron sputtering guns with metallic Al, Er, and Yb targets, argon and oxygen gas inlets, a sample heating element, and a substrate bias plasma. (b) Processing steps for fabrication of $Al_2O_3:Er^{3+}:Yb^{3+}$ waveguides.

### 5.2.2 Patterning of Er:Yb:$Al_2O_3$ Waveguides via Wet-Chemical Etching

Before etching the $Al_2O_3:Er^{3+}:Yb^{3+}$ films used to fabricate waveguides, we performed etch tests on several $Al_2O_3:Er^{3+}:Yb^{3+}$ films to verify etch rates, and ensure the photoresist would not degrade in the heated phosphoric acid. We defined large mesa features (2 cm × 2 cm) using contact lithography in an 800-nm-thick S1808 photoresist layer spun on at 3500 rpm for 45 s with a soft bake of 110°C for 1.5 minutes. We performed exposures using 5.7 mW/cm$^2$ 365-nm UV light for 9 seconds, after which the resist was soft baked again, before development in pure MF-319 developer for ~1 minute. We hard baked the sample at 130°C for 10 minutes to reflow the resist sidewalls. After many samples were prepared in a similar manner, we immersed them in ~250 mL of 85% pure $H_3PO_4$ at 60 ± 3°C with a stirring magnet at 1.5 Hz for various amounts of time and rinsed them in de-

ionized water after removal. We then assessed the etch depths using a stylus profilometer after removing the resist layer with acetone. We observed repeatable etch rates for films of similar composition, including 27±1 nm/min for a sample $Al_2O_3$:$Er^{3+}$:$Yb^{3+}$ co-doped film denoted Film 3 as shown in Table 5.1. However, it was discovered that etch rates were to some extent composition dependent and varied slightly from film to film (~25–35 nm/min). In general, it was observed that co-doped films have lower etch rates (~10 nm/min) than singly-doped and undoped films, which might be related to various factors including the film composition, density and/or porosity and bears further investigation when etching films of varying dopant concentrations. Figure 5.2 show an image of the processing setup during wet-etching of a full 3-inch sample.

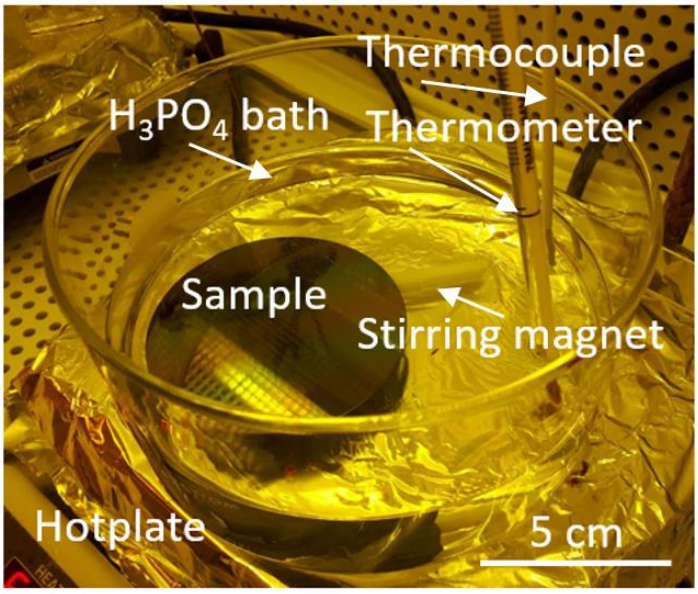


**Figure 5.2.** Image of processing setup with labelled components used for wet-etching.

We patterned the $Al_2O_3$:$Er^{3+}$:$Yb^{3+}$ films using an S1808 photoresist mask and wet etching in phosphoric acid ($H_3PO_4$). The phosphoric acid isotropically etches the $Al_2O_3$:$Er^{3+}$:$Yb^{3+}$ films, leading to smooth sidewalls but undercut of the photoresist mask,

which is an acceptable tradeoff given the typical etch depths and widths required for rare-earth-doped ridge waveguide amplifiers [8]. Further, it is straightforward, low-cost, and avoids etching in hazardous chlorine and bromine-based gases alternatively used to etch $Al_2O_3$ waveguides [10]. It was discovered during process optimization that a relatively large volume of acid is required for stable etch rates and repeatable results (~250 mL). This is due to the chemical process for wet-etching $Al_2O_3$ in $H_3PO_4$, which requires a certain $H^+$ ion concentration. The H+ concentration is reduced as the reaction occurs rendering the solution less acidic throughout the etch time as governed by its reaction stoichiometry [21]:

$$Al_2O_3 + 6H^+ \rightarrow 2Al^{3+} + 3H_2O.$$

Additionally, consistent etch results were achieved by keeping this concentration homogenous in the etchant mixture with the stir magnet, and by raising the sample during etching on a pedestal inside the acid bath which was levelled prior to the start. It was also observed that subsequent cooling and re-heating of the acid to etch a new sample leads to a roughening of the films' surface for samples doped with rare earth ions. It is anticipated since erbium and ytterbium do not take part in the chemical etching process they may exist in the solution as grouped clusters. This roughened surface after etching, as well as an over etched waveguide with the undercut photoresist is shown in Fig. 5.3 (a) and b) respectively.

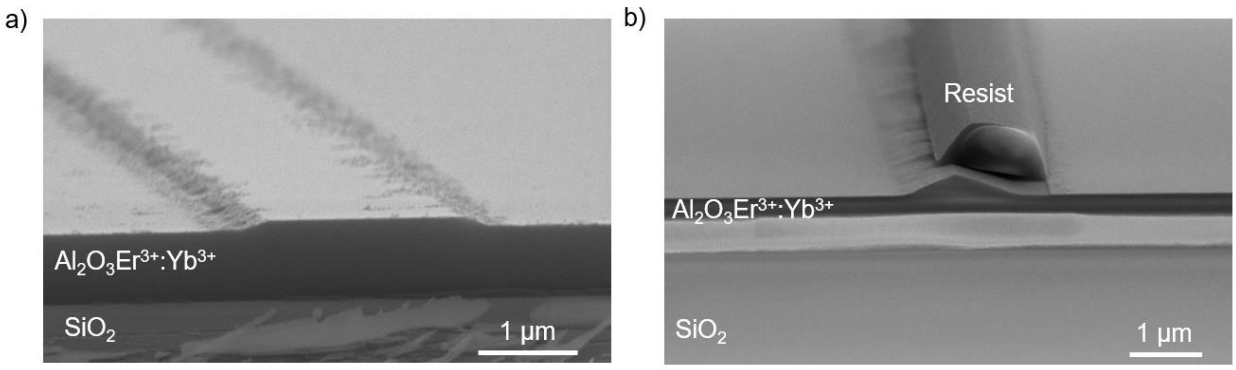


**Figure 5.3.** SEM image of the cross section of an $Al_2O_3:Er^{3+}:Yb^{3+}$ waveguide after (a) etching with re-used acid leading to roughening and (b) after over-etching leading to resist lift-off.

We then used the contact photolithography and wet etching process to define straight waveguide features of varying widths in an $Al_2O_3:Er^{3+}:Yb^{3+}$ film. We formed the waveguide end facets by cleaving, and then removed the photoresist mask with acetone and brief immersion in nitric acid ($HNO_3$). We inspected the final facet profile and sidewalls via scanning electron microscopy (SEM), as shown in Fig 5.4 (a–d) for select widths of 2.0–5.0 µm. As seen in Fig. 5.4 (d) the sidewall roughness is visibly low, with slight curtaining of the waveguide sidewalls laterally to the propagation direction. For samples intended for waveguide measurements, an additional fabrication step was taken to spin on a 1.0-µm-thick glass fluoropolymer to act as a top-cladding layer. We performed this spin at 1750 rpm for 40 seconds with post bakes of 50, 80, and 180°C for 10, 30 and 30 minutes respectively.

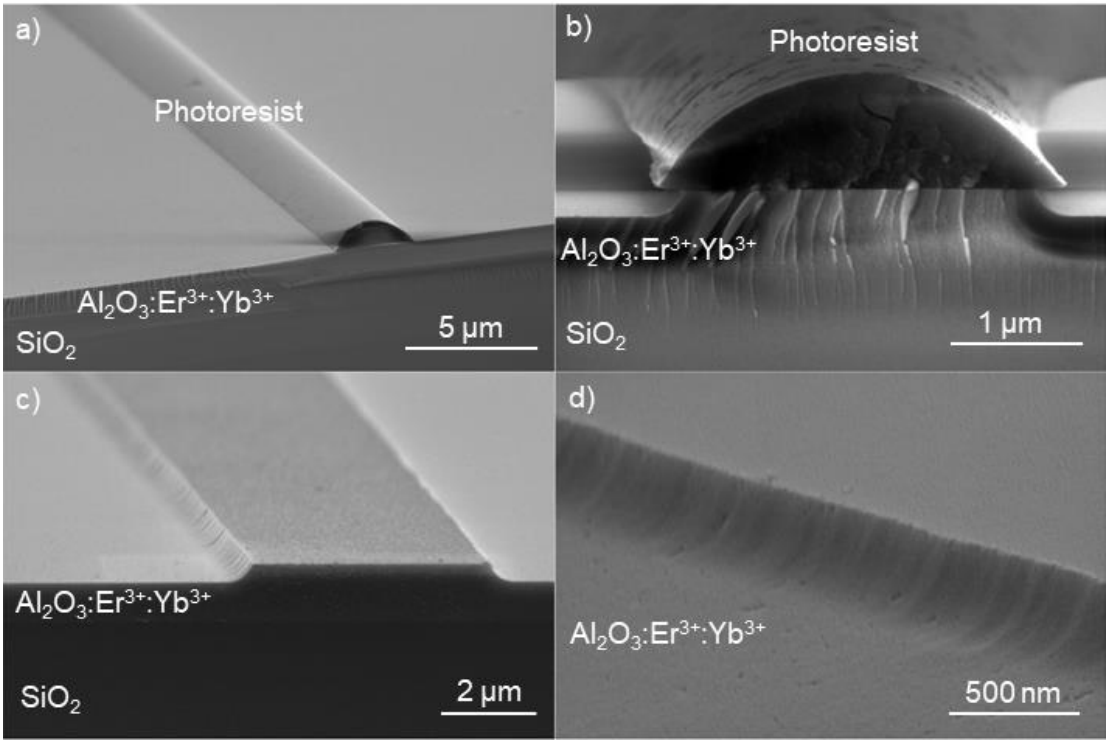


**Figure 5.4.** (a) Photoresist mask on an $Al_2O_3:Er^{3+}:Yb^{3+}$ film on oxidized silicon wafer prior to etching. (b) Waveguide facet profile after etching and before photoresist removal showing curved sidewalls. (c) Image of an $Al_2O_3:Er^{3+}:Yb^{3+}$ waveguide after photoresist removal. (d) Close-up view of the waveguide sidewall.

Here ridge waveguide structures are utilized which also allows for polarization insensitive pump and signal operation [12] around 980 and 1550 nm. After the etch process was validated, we designed and fabricated single mode waveguides and ring resonator structures to be used in characterizing the waveguide losses, polarization dependence, and optical gain. We designed a lithography mask aimed at waveguide loss measurements for transverse electric (TE) and transverse magnetic (TM) modes at 1640 nm as well as gain measurements from 1510–1640 nm. Using previous works as a starting point [3,12], the single mode conditions for TE and TM modes at 980 and 1550 nm were investigated and obtained for a 1.0 µm thick film, 250 nm etch depth and 2.2 µm

wide waveguide resulting in a simulated minimum bend radius of ~2.4 mm. We used the above processing steps to fabricate a series of straight 2.2-μm-wide waveguides with lengths up to 5 cm and ring resonator structures with nominal gaps (i.e. gaps on the contact mask) varying from 0.8–5.0 μm and radii of 3000 μm.

## 5.3 Characterization

To optically characterize the films and waveguides, three main measurements were performed to extract and confirm the relative rare-earth concentrations, polarization dependent signal background losses, and optical gain from 1510–1640 nm. To do so, a single film was prioritized for each measurement to accommodate the varying waveguide structures required, namely short waveguides for optical absorption measurements, ring resonators of varying gaps for loss measurements, and longer waveguides for gain measurements using 970 nm pumping. Table 5.2 summarizes these measurements and their results for the three films shown in Table 5.1, where grayed out entries represent measurements which were not performed for that film.

**Table 5.2.** $Al_2O_3:Er^{3+}:Yb^{3+}$ film and waveguide characterization summary

| Objective | Measurement | Film 1 | Film 2 | Film 3 |
|---|---|---|---|---|
| Concentration ($10^{20}$ $cm^{-3}$) | Optical absorption (Er / Yb) | 1.4 / 1.8 | | |
| Loss (dB/cm) | Prism coupling [847 nm] (film loss) | 2.1 ± 0.1 | 1.1 ± 0.1 | 1.6 ± 0.1 |
| | Prism coupling [1550 nm] (film background loss) | 0.4 ± 0.1 | 0.3 ± 0.1 | 0.2 ± 0.1 |
| | Ring resonator [1640 nm] (waveguide loss) | | 0.9 ± 0.1 | |
| Gain [1533 nm] (dB/cm) | 970 nm pump-probe (waveguide) | | | 1.4 ± 0.3 |

### 5.3.1 Optical Loss via Prism Coupling and Waveguide Absorption

We investigated the thickness, refractive index, and propagation loss in all three $Al_2O_3:Er^{3+}:Yb^{3+}$ films using the prism coupling method for pump and signal wavelengths.

Optical techniques were used to measure dopant concentrations for short waveguides patterned into Film 1 to avoid the difficulties in differentiating between the signals of Er and Yb co-dopants, which have similar atomic mass, using RBS [19]. The thickness of Film 1 was determined to be 1070 nm, and the refractive indices were found to be 1.616 and 1.604 at 638 and 1550 nm, respectively. The optical loss of the fundamental transverse-electric (TE) polarized mode of the film was first measured from 1510–1640 nm, where erbium absorption, but no ytterbium absorption, is present, to characterize the erbium dopant concentration. We measured the loss at different wavelengths within this range and compared it to the known erbium absorption cross section of $Al_2O_3:Er^{3+}$ [8], and accounting for the calculated overlap of the optical mode with the $Al_2O_3:Er^{3+}:Yb^{3+}$ waveguide (80%), used the fit to extract the erbium dopant concentration. These optical measurements were then used to verify the concentrations determined from RBS calibration measurements using singly-doped films as shown in Table 5.1. Figure 5.5 (a) shows the loss measured at each wavelength, while (b) shows the loss versus absorption cross section, giving an erbium ion concentration of $1.7\times10^{20}$ ions/cm$^3$. Losses measured around 980 nm are the result of both erbium and ytterbium absorption combined. The previously calculated erbium concentration and known absorption cross sections in $Al_2O_3:Er^{3+}$ [17] can be used to calculate the contribution of erbium atoms to the absorption in this range. By subtracting the estimated erbium absorption loss from the total measured loss, the remaining absorption loss is considered the result of ytterbium absorption and background loss. That loss is similarly fit compared to the known $Al_2O_3:Yb^{3+}$ absorption cross sections [17] to extract an ytterbium ion concentration. Here, we measured the loss through a short 0.5-cm-long ridge waveguide (etch depth of 250 nm and width of 2.2 μm),

because the high absorption, large input powers and > 1 cm propagation length required to obtain measurable signal on the prism coupling system resulted in significant $Yb^{3+}$-ion excitation and absorption saturation in the film. Figure 5.5 (c) shows the measured loss and the contribution of the erbium and ytterbium ions to the total loss. Figure 5.5 (d) shows the measured ytterbium-absorption related loss versus cross section, which is fit to extract an $Yb^{3+}$ ion concentration of $1.8\times10^{20}$ ions/$cm^3$. Using the same fittings (and film loss measurements in the range 950–970 nm where saturation does not occur), the background loss of the film was measured to be 2.3 and 0.6 dB/cm at 980 and 1550 nm, respectively. From these fittings we can conclude a slight underestimation of Yb concentration (~0.4–0.6 ions/$cm^3$) is obtained from the RBS singly-doped film calibration measurements for Film 1 which is considered for future depositions and relative dopant level optimization.

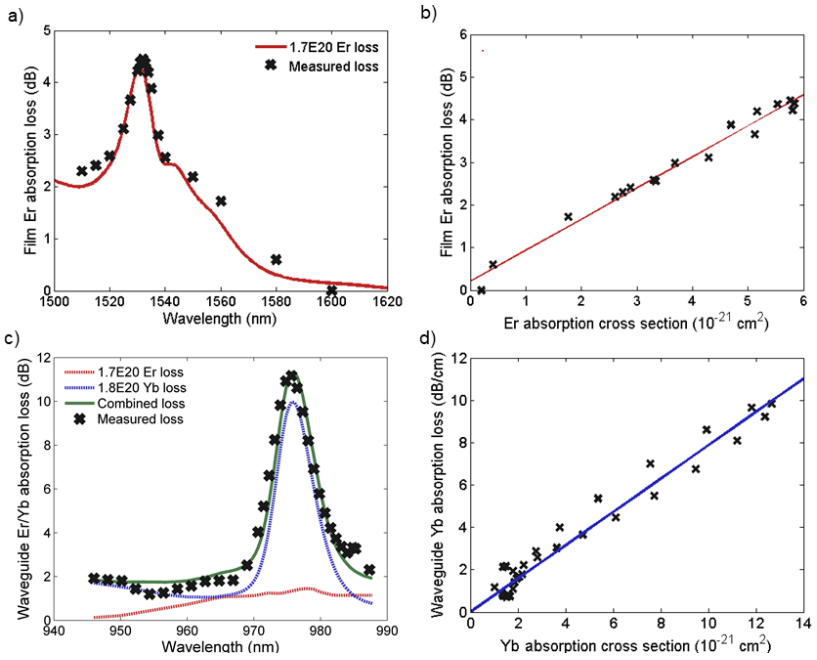


**Figure 5.5.** (a) Measured $Al_2O_3$:$Er^{3+}$:$Yb^{3+}$ film absorption loss versus wavelength around 1532 nm and (b) $Er^{3+}$ absorption cross section to extract an erbium ion concentration of $1.7 \times 10^{20}$ ions/cm$^3$. (c) The combined total $Al_2O_3$:$Er^{3+}$:$Yb^{3+}$ waveguide absorption loss measured around 975 nm. The calculated erbium absorption loss (red line) based on the samples measured ion concentration and measured absorption cross sections in [17] is subtracted from the total loss (black dots), leaving the ytterbium-related absorption loss (blue line). (c) The measured ytterbium-related absorption loss in the waveguide fit against the $Yb^{3+}$ absorption cross section at each wavelength, used to determine a $1.8 \times 10^{20}$ ions/cm$^3$ ytterbium concentration.

### 5.3.2 Passive Waveguide Device Measurements

We measured ring resonators at varying gaps patterned into Film 2 to extract the internal Q factor and waveguide propagation loss for the fundamental TE and TM modes at 1640 nm. We used edge coupling and manual micrometer-controlled stages to launch 1510–1640 nm laser light from polarization maintaining 2.5 μm spot size lensed fibers into the fabricated $Al_2O_3$:$Er^{3+}$:$Yb^{3+}$ waveguides. To control the launched polarization to the waveguide facet, we adjusted polarization paddles in between measurements. By fitting

resonance spectra as shown in Fig. 5.6 (a–b), waveguide losses were estimated for varying wavelengths and launched polarizations. To confirm the TE and TM nature of the modes we observed shifting resonant wavelengths, and consistent free spectral range differences between TE and TM modes. A summary of the ring resonator measurements is shown as insets in Fig 5.6 (a–b), with overlapped Lorentzian fits to the spectra for TE and TM modes. Figure 5.6 (c–d) demonstrates the simulated TE modes in the measured waveguide at signal and pump wavelengths respectively, while Fig. 5.6. (e–f) includes a diagram and image of a ring resonator during measurement.

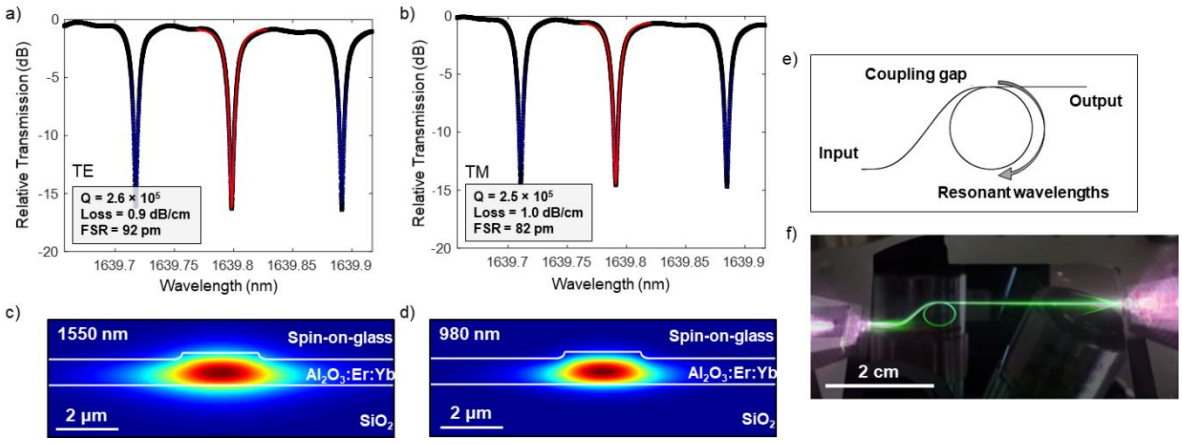


**Figure 5.6.** (a) TE and (b) TM transmission spectra for a ring resonator with a 3.0 µm designed gap and overlaid Lorentzian fits for extracting the quality factor. Simulated TE mode at (c) 1550 nm and (d) 980 nm for a 2.2 µm wide waveguide structure with 250 nm etch depth and 1.0 µm thick film. (e) Diagram of ring resonator waveguide coupled structure demonstrating bus and ring region. (f) Photograph of chip during measure with dual side 970 nm pumping used to illuminate ring with characteristic green erbium emission.

Figure 5.6 demonstrates the results from the ring resonator measurements for Film 2. It can be seen in the insets of Fig 5.6 (a–b) that we observed relatively polarization insensitive losses at 1639 nm, showing similar results within error. To be certain the

resonance can be used for an estimation of waveguide loss the ring is required to be in the under-coupled regime. This was verified by sweeping the mentioned gaps for each wavelength and polarization conditions which arrived at a 3.0 μm gap for TE and TM 1640 measurements. The characteristic green glow of the erbium ions in the waveguide during measurement can be seen in Fig. 5.6 (f), while pumping at 970 nm. From these resonance measurements, an upper-limit estimation of waveguide signal losses can be appropriately concluded for the waveguide fabrication process. These measurements were used to estimate the waveguide losses and quantify the internal net gain in a 3.0-cm-long straight waveguide structured in Film 3.

### 5.3.3 Optical Amplification Measurements with 970 nm Pumping

We measured optical gain by using the setup shown in Fig. 5.7 (a). We used dual side pumping with two 970 nm diode lasers to increase the amount of on-chip pump power and fiber wavelength division multiplexers (WDMs) to combine/separate the pump from the 1510–1640 nm signal. The incident pump and signal powers were measured using an integrating sphere, with estimated –4.5 dB coupling losses per facet of the waveguide based on insertion loss measurements. High launched signal powers were achieved with the use of an external EDFA in the set-up. Besides the WDM, separating and filtering of the pump light was carried out with additional free space filtering before reaching the photodetector. We also utilized lock-in amplification to separate the amplified signal from the amplified spontaneous emission (ASE) during measurement. The waveguide transmission spectra for varying pump powers are shown in Fig. 5.7 (b) for patterned Film 3 in a 3.0-cm-long, 2.2 μm wide waveguide with 250 nm etch depth. Waveguide loss estimates based on ring resonator measurements in Film 2 provide an upper limit on propagation losses at 1640 nm as shown in Fig. 5.6 (a). To extract the internal gain in

straight waveguides patterned into Film 3, waveguide losses were determined using a combination of insertion loss measurements and upper limits provided by ring resonator measurements in Film 2. Lower insertion loss measurements for Film 3, and the absence of ring coupling and excess bending losses suggest a waveguide propagation loss range which includes the lower limit background film loss and upper limit estimate from fit resonant data. This results in a waveguide loss estimate of 0.5 ± 0.3 dB/cm for Film 3 which was used to quantify the internal gain and associated error margin. Figure 5.7 (c) summarizes this internal net gain for selected wavelengths at different pump powers. The inset shows the internal net gain measured for varying signal powers at 1533 nm at peak pump power.

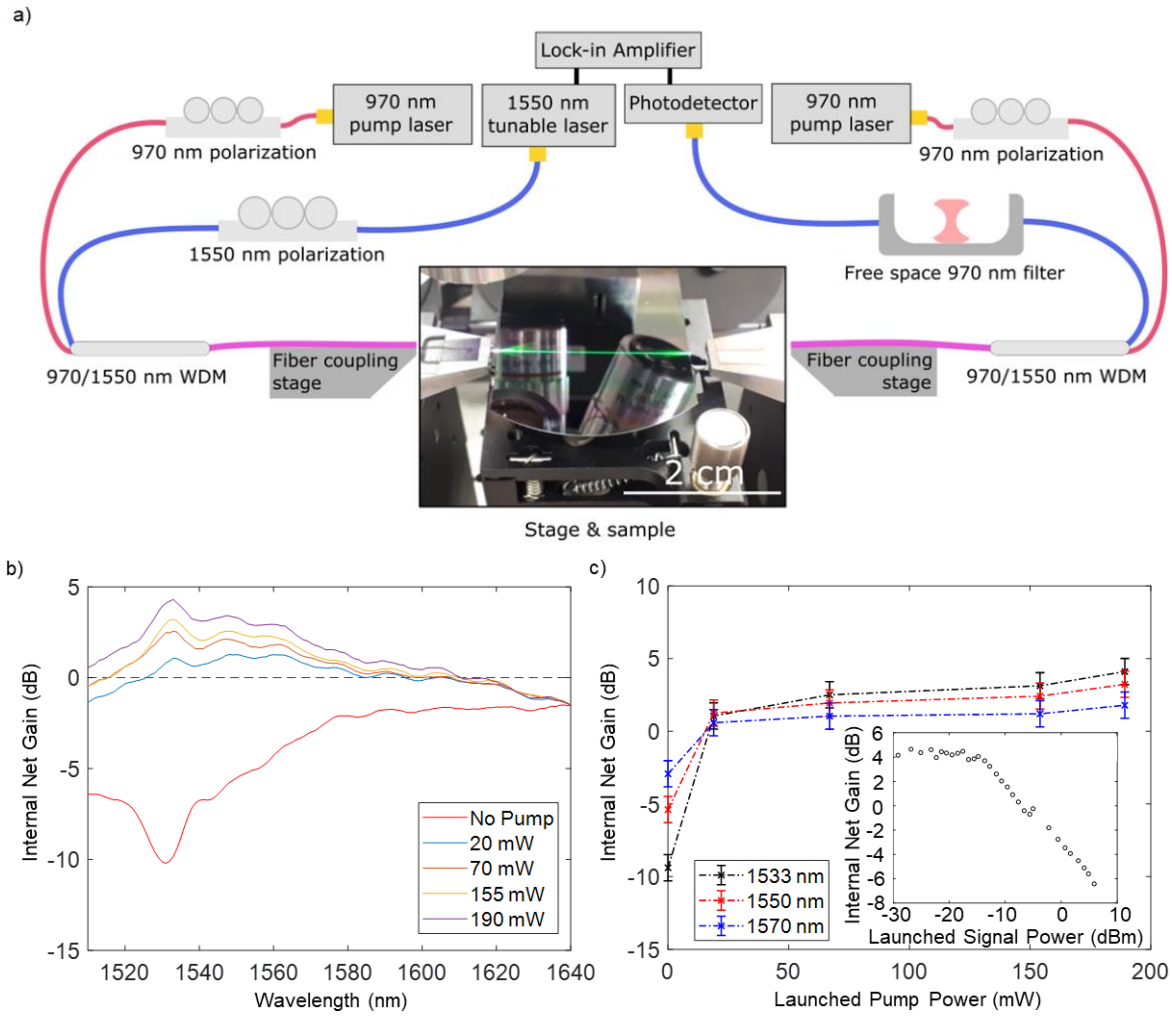


**Figure 5.7.** (a) Diagram of measurement setup and photograph of sample during measurement. (b) Pumped and un-pumped transmission spectra from 1510–1640 nm in 1.0 μm thick Film 4 with a 2.2 μm wide waveguide and an etch depth of 250 nm at varying internal pump powers demonstrating inverted rare earth absorption dip and internal net gain at low-level signal powers. (c) Internal net gain plotted for various wavelengths and pump powers. Peak internal net gain of 4.3 ± 0.9 dB measured at 1533 nm. Internal net gain measured for varying launched 1533 nm signal powers at 190 mW launched pump power (inset).

We measured a peak internal net gain of 4.3 ± 0.9 dB at 1533 nm for a 3.0 cm long waveguide, corresponding to 1.4 ± 0.3 dB/cm. We also demonstrated that net internal gain

was achieved up to ~–8.5 dBm launched signal power. It should be noted that with limited pump power on-chip due to high insertion loss, we did not observe gain saturation, which points toward higher gain being possible with decreased coupling and propagation losses. Compared to previous works for singly-doped $Al_2O_3$:$Er^{3+}$ waveguide amplifiers on Si which demonstrated 1.6 and 2.0 dB/cm gain with background losses of 0.19 and 0.23 dB/cm and were fabricated using similar methods [3, 8], this result shows comparable performance with promise moving forward with decreased losses.

Future work aims to demonstrate higher net gain in longer waveguides by decreasing the optical losses for both pump and signal wavelengths. Material related film losses can be optimized with variations in oxygen flow and temperature during deposition [19]. Improved fiber-chip coupling and optimized rare-earth dopant ratios is also expected to lead to superior performance [14] with lower pump thresholds for gain and higher gain per unit length. Additionally, decreasing $Er^{3+}$ clustering sites which have been shown to lead to fast quenching processes in $Al_2O_3$:$Er^{3+}$ amplifiers [3], may be possible with $Yb^{3+}$ co-doping [18,19]. This can be verified by modelling the results shown here using a rate equation solver for the co-doped matrix, similar to the quenching considerations shown in [3]. By building in parameters obtained from spectroscopic characterization of the $Al_2O_3$:$Er^{3+}$:$Yb^{3+}$ films [19], such a model will allow for optimization of the relative doping concentrations and waveguide length to maximize amplifier and laser performance.

### 5.4 Conclusion

We demonstrated a flexible and low-cost process for co-sputtering of $Al_2O_3$:$Er^{3+}$:$Yb^{3+}$ thin films and their subsequent patterning with contact lithography and $H_3PO_4$ wet-etching. We used SEM and profilometry to assess the etch rates and sidewall roughness as well

as facet profile throughout the waveguide fabrication process. Optical pumping via edge coupling was shown to produce 4.3 ± 0.9 dB internal net gain at 1533 nm for a 3.0 cm long, 2.2 μm wide waveguide with a 250 nm etch depth in a 1.0 μm thick film, with $Er^{3+}$ and $Yb^{3+}$ dopant concentrations of $1.4 \times 10^{20}$ and $2.1 \times 10^{20}$ ions/cm$^3$, respectively. This gain compares to previous works for $Al_2O_3$:$Er^{3+}$ on Si waveguide amplifiers fabricated using similar methods and includes pathways to improve. The material platform and fabrication process show promise for producing waveguide amplifiers and lasers with high gain, efficient pump absorption and high output power for telecommunications, LIDAR, bio sensors and photonic integrated circuit applications.

### 5.5 References


1. P. C. Becker, N. A. Olsson, and J. R. Simpson, *Erbium-Doped Fiber Amplifiers: Fundamentals and Technology* (Academic Press, 1999).
2. J. D. B. Bradley and M. Pollnau, “Erbium-doped integrated waveguide amplifiers and lasers,” Laser Photonics Rev. **5**(3), 368–403 (2011).
3. S. A. Vázquez-Córdova, M. Dijkstra, E. H. Bernhardi, F. Ay, K. Wörhoff, J. L. Herek, S. M. García-Blanco, and M. Pollnau, “Erbium-doped spiral amplifiers with 20 dB of net gain on silicon,” Opt. Express **22**(21), 25993–26004 (2014).
4. E. S. Magden, N. Li, Purnawirman, J. D. B. Bradley, N. Singh, A. Ruocco, G. S. Petrich, G. Leake, D. D. Coolbaugh, E. P. Ippen, M. R. Watts, and L. A. Kolodziejski, “Monolithically-integrated distributed feedback laser compatible with CMOS processing,” Opt. Express **25**(15), 18058–18065 (2017).
5. E. H. Bernhardi, K. Werf, A. Hollink, K. Worhoff, R.M. de Ridder, V. Subramaniam, and M. Pollnau, “Intra-laser-cavity microparticle sensing with a dual-wavelength distributed-feedback laser,” Laser Photonics Rev. **7**(4), 589–598 (2013).
6. K. Worhoff, J. D. B. Bradley, F. Ay, D. Geskus, T. P. Blauwendraat, and M. Pollnau, “Reliable low-cost fabrication of low-loss $Al_2O_3$:$Er^{3+}$ waveguides with 5.4-dB optical gain,” IEEE J. Quantum Electron. **45**(5), 454–461 (2009).
7. M. Pollnau and J. D. B. Bradley, “Optically pumped rare-earth-doped $Al_2O_3$ distributed-feedback lasers on silicon,” Opt. Express **26**(18), 24164 (2018).
8. J. Bradley, L. Agazzi, D. Geskus, F. Ay, K. Worhoff, and M. Pollnau, “Gain bandwidth of 80 nm and 2 dB/cm peak gain in $Al_2O_3$:$Er^{3+}$ optical amplifiers on silicon,” J. Opt. Soc. Am. B. **27**(2), 187-196 (2010).
9. J. Rönn, W. Zhang, A. Autere, X. Leroux, L. Pakarinen, C. Alonso-ramos, A. Säynätjoki1, H. Lipsanen, L. Vivien, E. Cassan and Z. Sun, “Ultra-high on-chip

optical gain in erbium-based hybrid slot waveguides," Nat. Commun. **10**(1), 432 (2019).
10. J. D. B. Bradley, F. Ay, K. Wörhoff, and M. Pollnau, "Fabrication of low-loss channel waveguides in $Al_2O_3$ and $Y_2O_3$ layers by inductively coupled plasma reactive ion etching," App. Phys. B **89**(2-3), 311–318 (2007).
11. B. Zhou, and W. F. Ramirez, "Kinetics and modeling of wet etching of aluminum oxide by warm phosphoric acid," J. Electrochem. Soc. **143**(2), 619-623 (1996).
12. Özden, M. Demirtas, and F. Ay, "Polarization insensitive single mode $Al_2O_3$ rib waveguide design for applications in active and passive optical waveguides," J. Opt. Soc. Eu. Rapid Pub. **10**, 15005 (2015).
13. Strohhöfer, and A. Polman, "Absorption and emission spectroscopy in $Er^{3+}$–$Yb^{3+}$ doped aluminum oxide waveguides," Opt. Mater. **21**(4), 705-712 (2003).
14. Strohhöfer and A. Polman, "Relationship between gain and Yb3+ concentration in $Er^{3+}$–$Yb^{3+}$ doped waveguide amplifiers," J. Appl. Phys. **90**(9), 4314–4320 (2001).
15. T. Matniyaz, F. Kong, M. T. Kalichevsky-Dong, and L. Dong, "Record 302W single-mode power from an Er/Yb fiber MOPA," Opt. Lett. **45**(10), (2020)
16. O. D. Varona, W. Fittkau, P. Booker, T. Theeg, M. Steinke, D. Kracht, J. Neumann, and P. Wessels, "Single-frequency fiber amplifier at 1.5 μm with 100 W in the linearly-polarized TEM 00 mode for next-generation gravitational wave detectors," Opt. Express **25**(21)**,** 2634–2636 (2017).
17. L. Agazzi., *Spectroscopic Excitation and Quenching Processes in Rare-Earth-Ion-Doped Al2O3 and their Impact on Amplifier and Laser Performance*, (Ph.D. Thesis, University of Twente, 2012).
18. E. Yahel, and A. Hardy. "Efficiency optimization of high-power , $Er^{3+}$ – $Yb^{3+}$ -codoped fiber amplifiers for wavelength-division-multiplexing applications," J. Opt. Soc. **20**(6), 1189–1197 (2003).
19. R. Wang, McMaster University, 1280 Main Street West, Hamilton, ON. And and J. D. B. Bradley are preparing a manuscript to be called "Ytterbium and erbium doped aluminum oxide thin films: co-sputtering deposition, photoluminescence, luminescent lifetime, energy transfer and quenching fraction."
20. Q. Song, J. Gao, X. Wang, H. Chen X. Zheng, T. Wang, C. Li, and C. Song, "Fabrication of $Yb^{3+}$:$Er^{3+}$ co-doped $Al_2O_3$ ridge waveguides by the dry etching," Opt. Eng. **46**(4), 040509 (2007).
21. K. Solehmainen, M. Kapulainen, P. Heimala, and K. Polamo, "Erbium-doped waveguides fabricated with atomic layer deposition method," IEEE Photonics Techol. Lett. **16**(1), 194–196 (2004).
22. M. Demirtas, C. Odaci, N. K. Perkgoz, C. Sevik, and F. Ay, "Low loss atomic layer deposited $Al_2O_3$ waveguides for applications in on-chip optical amplifiers," IEEE J. Sel. Top. Quantum Electron. **24**(4), 1–8 (2018).

# Chapter 6

## Hybrid Silicon-Tellurium-Dioxide DBR Resonators Coated in PMMA for Biological Sensing

This chapter includes the results for two Si DBR waveguide devices which were tested with a variety of claddings and used as sensors after being coated with $TeO_2$ and PMMA layers. The PMMA-$TeO_2$-Si DBRs were fabricated using a standard silicon photonics foundry process and back-end deposition and post-processing. Oxygen plasma treatment was shown to provide hydrophilicity to the PMMA films by water contact angle measurements. Thermal, water and bovine serum albumin protein sensing were demonstrated, as well as the functionalization of PMMA via plasma treatment to allow chemisorption of proteins on the sensor surface. Optical simulations of the modal properties of the DBR sensors are discussed, as well as prospects on moving forward with the devices as a platform for laser sensors with rare-earth integration. This work represents a manuscript which is in preparation by the authors and has been included in the thesis due to its combination of CMOS compatible flexible fabrication techniques to realize an optical sensor with a Si waveguide and an oxide glass capable of rare-earth integration.

**Abstract:** We report on silicon waveguide distributed Bragg reflector (DBR) cavities hybridized with a tellurium dioxide ($TeO_2$) cladding and coated in plasma functionalized poly (methyl methacrylate) (PMMA) for label free biological sensors. We describe the device structure and fabrication steps, including reactive sputtering of $TeO_2$ and spin coating and plasma functionalization of PMMA on foundry processed Si chips, as well as the characterization of two DBR designs via thermal, water, and bovine serum albumin

(BSA) protein sensing. Plasma treatment on the PMMA films was shown to decrease the water droplet contact angle from ~70 to ~35°, increasing hydrophilicity for liquid sensing, while adding functional groups on the surface of the sensors intended to assist with immobilization of BSA molecules. Thermal, water and protein sensing were demonstrated on two DBR designs, including waveguide-connected sidewall (SW) and waveguide-adjacent multi-piece (MP) gratings. Limits of detection of 60 and 300 $\times 10^{-4}$ RIU were measured via water sensing, and thermal sensitivities of 0.11 and 0.13 nm/°C were measured from 25–50 °C for SW and MP DBR cavities, respectively. Plasma treatment was shown to enable protein immobilization and sensing of BSA molecules at a concentration of 2 µg/mL diluted in phosphate buffered saline (PBS), demonstrating a ~1.6 nm resonance shift and subsequent full recovery to baseline after stripping the proteins with sodium dodecyl sulfate (SDS) for a MP DBR device. These results are a promising step towards active and laser-based sensors using rare-earth-doped $TeO_2$ in silicon photonic circuits, which can be subsequently coated in PMMA and functionalized via plasma treatment for label free biological sensing.

## 6.1 Introduction

Portable diagnosis for antigens, including viruses, DNA, proteins, and a variety of other biologically relevant species has become a necessity to limit the spread of disease and avoid future pandemics. To achieve this, industry requires a cost-effective solution which is mass-producible and allows for diagnostics in the field instead of relying on expensive laboratory facilities. Integrated optical waveguide technology enables this, by providing compact lab-on-chip biological and environmental sensors, capable of sensitive, real-time, and rapid assessment.

Amongst the photonic material platforms, silicon-on-insulator (SOI) has proven itself as a cornerstone of the field and reliable choice for waveguide sensor devices [1–4]. Repeatable and low-cost SOI photonic devices are possible by leveraging complementary metal-oxide-semiconductor (CMOS) fabrication processes to produce Si waveguides which have been demonstrated to show sensing capabilities for a number of devices [5]. Integrated photonic sensors have demonstrated themselves as competitive alternatives to laboratory and healthcare optical sensor standards such as surface plasmon resonance techniques [6]. In integrated photonic biosensors, refractive index, physical and thermal fluctuations all can be monitored by changes in the transmission of an optical resonator, which when interrogated by a laser in the presence of an analyte can provide real-time rapid monitoring and sensing for a variety of biologically relevant species and processes. These devices have been realized on the Si photonic platform as a variety of resonators including rings, disks and interferometers [3], as well as 1D photonic crystal rings [7], and Bragg grating waveguides [5]. While rings and disks are highly compact, they suffer from drawbacks such as low free-spectral range and thus limited dynamic sensing capability, and reduced sensitivity due to limited surface area coverage. On the other hand, distributed Bragg gratings provide stopbands with dynamic and unique, non-repeating resonances and are scalable in terms of sensing area, which has enabled their application as high quality evanescent waveguide sensors [8].

Device sensitivity is a key feature for optical sensors, which benefits from significant modal overlap with the sensing region. This can be achieved with various design methods, however those which increase sensitivity sacrifice quality factors due to increased overlap with an optically lossy analyte. Laser based sensing instead of basic

passive resonator-based refractive index sensing allows for detection of smaller single particles, free space or far-field interrogation, and intensity-based sensing [9] all of which utilizes the ultra-narrow emission of a laser line. Rare earth ions have been demonstrated to enable monolithic lasers with low cost and wavelength versatility, making them attractive to silicon photonics platforms [10–12]. Various demonstrations of laser based sensors have emerged, including $Er^{3+}$ and $Yb^{3+}$ doped $SiO_2$ microtoroids [13,14], patterned rare-earth doped $Al_2O_3$ to form DFB cavities [15] and ring resonators [16] for biological and environmental monitoring. Implementing these devices on an SOI chip, where the laser resonator is integrated into the silicon waveguide layer and the photonic sensor is not a stand-alone device but co-integrated with other devices such as detectors, can allow for an ultra-compact form-factor with optical sensing and electronic readout all on the same chip. Significant efforts on the $Al_2O_3$ platform, which is a well-established rare earth host material, have led to demonstrations of passive and active $Yb^{3+}$ doped sensors [17] with limits of detection of ~1.0 and $3.7 \times 10^{-6}$ respectively, as well as self-referenced rings with PMMA integrated gratings [18]. $TeO_2$ is another attractive rare-earth host material for integrated photonics due to its relatively higher refractive index (n ~2.0–2.1), nonlinear optical properties, low loss [19] and relatively high solubility for rare-earth ions like $Er^{3+}$, which has enabled on-chip optical amplification and lasing [20] and makes it prospective for laser-based sensors. In addition to its recent demonstration as a cladding for high-Q resonators [21] and monolithic laser material on SOI via incorporation of rare-earth dopants [11], the high refractive index of the $TeO_2$ cladding enables the mode to be ‘pulled’ up to the top layer where sensing occurs for better sensitivity. A $TeO_2$ microcavity coupled to a Si waveguide has been demonstrated as a sensor platform,

which however suffered from bus coupling control and limited sensing surface area [22]. Si-$TeO_2$ hybridized DBR waveguides might provide a promising alternative pathway as a biological sensor and have promise in development as an on-chip laser with scalable area and dynamic sensitivity for sensing.

In both passive and laser-based sensors, surface layer functionalization is important for facilitating biological interactions with proteins or viruses including immobilization, binding, and/or adsorption (physisorption and chemisorption). Additional surface chemistry is required for these interactions, which can be achieved through functionalization via the addition of oxygen rich groups which influence bonding sites for the biomarkers. Rather than performing functionalization directly on the Si or oxide cladding surface, which may lead to deleterious optical effects such as loss in the resonator, materials like polymers may be coated on top of the waveguides and functionalized by a variety of chemical or plasma methods. These polymers must also be optically transparent as to not introduce excess losses to the waveguides. PMMA is a prospective material for integration into sensor designs due to its high transparency in the near infrared, relatively low cost, and proven capability for functionalization via oxygen plasma treatment [23]. PMMA has been applied in integrated optical sensors, including as a fluorescently tagged biological sensing material for the detection of Chlamydia trachomatis specific immunoglobulins [24].

Here we report on the design, fabrication, optical properties, and sensor results of functionalized PMMA coated hybrid Si-$TeO_2$ waveguide with distributed Bragg reflector (DBR) cavities. Two Si DBR designs are characterized and compared with a variety of cladding materials including PMMA, $TeO_2$ and CYTOP, as well as a combination of

deposited $TeO_2$ and spin-coated PMMA. A fabrication process for directly functionalizing Si-$TeO_2$/PMMA sensors for chemisorption is demonstrated as well as subsequent thermal, water, and protein sensing using BSA. It is demonstrated that plasma functionalization enables direct immobilization and sensing of BSA on the PMMA surface and is not deleterious to the optical performance of the Si-$TeO_2$ DBR resonator. These results demonstrate a promising platform for passive and rare-earth laser-based sensing on silicon photonic chips and pathways for optimizing the design moving forward.

## 6.2 Design and Fabrication

### 6.2.1 Reactive Magnetron Sputtering of $TeO_2$ on Si Foundry Waveguides

The uncoated sensor chips were fabricated using the Advanced Micro Foundry (AMF) silicon photonics fabrication process, with 0.22 μm thick × 0.5 μm wide silicon strip waveguides on 2.0 μm of buried oxide on silicon substrates. Two DBR resonator designs were selected to study the sensor performance when adjusting properties such as the optical mode overlap with the sensing medium and grating structure: one with sidewall (SW) corrugations of 60 nm and a period of 326 nm in a 500 nm wide Si waveguide, and one with multiple 140 nm wide grating pieces with a period of 341 nm and a 250 nm gap adjacent to a 400 nm wide Si waveguide. The periods were selected to obtain resonances for the transverse electric (TE) polarized fundamental mode around 1550 nm. Gradual transitions of 50 μm length were included for both the multi-piece (MP) bus width taper and grating gap which reduces from 0.8 μm to 0.25 μm. Cavity lengths of 1200 and 1100 μm and symmetric gratings lengths of 500 and 600 μm were used in the SW and MP design, respectively. To improve edge coupling to the waveguide, inverse tapering was used to expand the mode which consists of 50 μm long transitions to a 180 nm waveguide width at the facet. SEM images of each DBR type are shown in Fig. 6.1 a)–b) before

depositing $TeO_2$, and inset images of the transition sections and details of the design as well as schematics of the resonators are displayed in Fig. 6.1 c) and d). The two designs represent distinct variations of the DBR strip waveguide and allow for comparison between cavities with high grating strengths and Si overlap (SW design) vs. cavities with larger modes, weaker grating perturbations and higher overlap in the surrounding materials (MP design). SW DBR waveguide resonators were selected for investigation based on their well understood operation for single mode passive resonator devices and sensors [5]. It was anticipated that the MP design would demonstrate resonances with decreased bandwidth due to lighter perturbations to the waveguide mode [25], which is advantageous for the realization of sensors and laser cavities due to sharper, more selective resonance spectra.

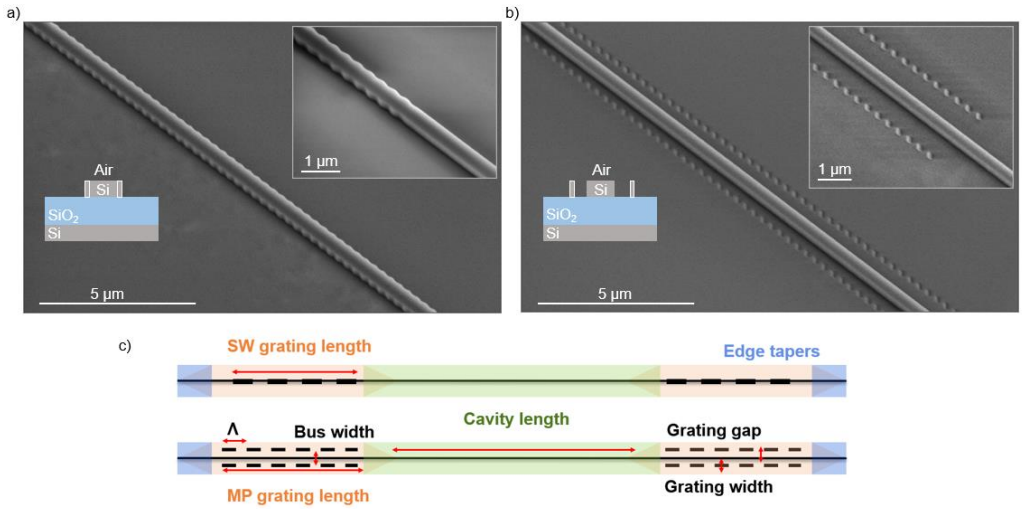


d)

| Grating Type | Bus Width (µm) | Period [Λ] (µm) | Grating Width (µm) | Grating Gap (µm) | Grating Length (mm) | Cavity Length (mm) |
|---|---|---|---|---|---|---|
| Sidewall (SW) | 0.5 | 0.341 | 0.06 | 0.00 | 0.5 | 1.2 |
| Multi-piece (MP) | 0.4 | 0.326 | 0.14 | 0.25 | 0.6 | 1.1 |

**Figure 6.1.** SEM images of (a) sidewall (SW) and (b) multi-piece (MP) silicon DBR waveguides with insets showing transition sections and cross section diagrams of the waveguide grating structures. Design schematic (c) and specifications (d) of SW and MP DBR gratings.

We deposited 500 nm of $TeO_2$ as an end of line process using reactive radio frequency (RF) magnetron sputtering after receiving the uncladded SOI chips from the foundry following the procedure outlined in [26]. The process is carried out at room temperature and a chamber pressure of 3 mTorr in oxygen and argon ambient, with a deposition rate of ~23 nm/min. The experimental procedures as described in [26], including prism coupling loss measurements and fine tuning of the deposition recipe, are used to optimize the deposited films for low optical propagation loss. Room temperature deposition of the $TeO_2$ film allows for deposition on thermally sensitive materials such as metals for electrical contacts in photodetectors or thermal tuning capabilities which are both desirable for sensor applications.

### 6.2.2 Polymer Spin Coating & Functionalization via Oxygen Plasma

PMMA spin coating was carried out at 1750 rpm for 45 seconds with a bake temperature of 80 °C for 1.5 minutes followed by a cure step of 150 °C for 10 minutes on $TeO_2$ coated chips. To functionalize the PMMA layer and activate $O_2$ groups on the surface, oxygen plasma treatment was carried out with a Harrick plasma cleaner at 750 mTorr for 1 min with 27.5 W of RF power. This process was repeated for any chips which required subsequent measurements after submersion in liquid and air drying or significant time spent out in open air. The stability of the process is time sensitive and known to decay once exposed to ambient conditions for approximately a week [23]. Immediate PDMS or SU8 microfluidic capping may protect the functional groups from interacting with the environment and decreasing in surface energy, as SU8 has shown to provide more stability in surface energy in ambient conditions after functionalization [23]. In this manner, the sensing layer could be protected from the environment or analyte until a controlled delivery method is carried out, allowing for increased stability of the packaged sensor.

Figure 6.2 summarizes the overall fabrication process of the DBR waveguide sensor. To investigate the DBR response for different cladding refractive indices, DBR devices were also coated with PMMA and CYTOP without any $TeO_2$ film. CYTOP spin coating was carried out at 1750 rpm for 45 seconds, with a bake and cure time of 120 and 180 °C for 1.5 and 10 minutes respectively.

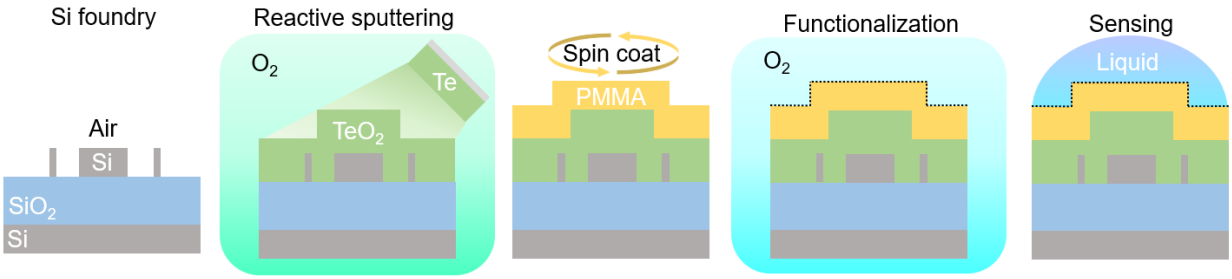


**Figure 6.2.** DBR waveguide sensor fabrication steps (shown for the MP DBR design).

## 6.3 Characterization

### 6.3.1 DBR Transmission Measurements

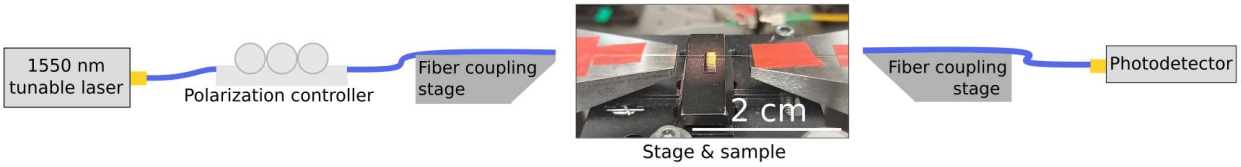


**Figure 6.3.** Illustration of the fiber coupling setup used for DBR transmission measurements and image of the sample during test.

The edge coupling setup shown in Fig. 6.3 was used to characterize the DBR cavities. Manual micrometer-controlled stages were used to launch 1510–1640 nm laser light from 2.5 μm spot size lensed fibers. Initially, uncladded chips received from foundry were measured to investigate the impact from variation in Si waveguide fabrication features from the multi-project wafer (MPW) run. Also, before and after measurements can be used to track the resonances and test the devices sensitivity to cladding. The measured

resonances for air cladded SW gratings are shown in Fig. 6.4, demonstrating the variation among identically designed devices on different chips from the same SOI wafer. MP grating resonances were observed only on a couple of devices with air cladding as the reduced overlap in the grating pieces causes weak perturbations to the mode. In two samples this was achieved demonstrating an average central wavelength of 1510.8 nm and ER of 11.8, but others are anticipated to be resonating at a lower wavelength than 1510 nm outside the measurement capabilities of the set-up used.

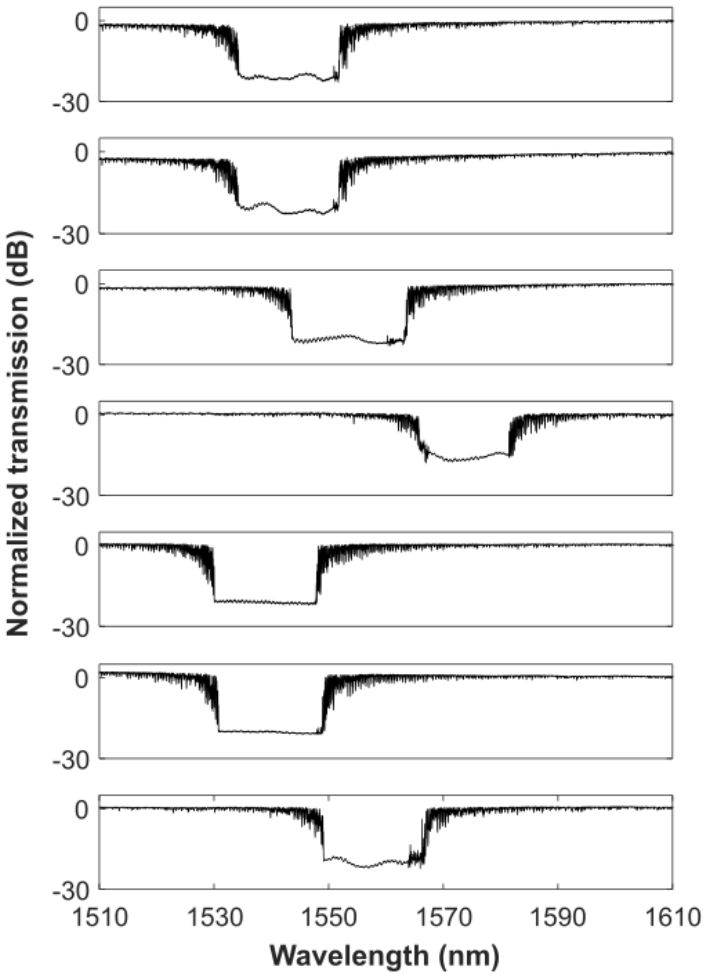


**Figure 6.4.** Comparison of spectra collected from the same uncladded SW DBR design on different chips. The average central wavelength is 1550.5 nm with a standard deviation of 12.1 nm.

After measuring resonances with air cladding, selected samples were either spin coated with PMMA, CYTOP or sputter coated with $TeO_2$ to investigate the SW and MP DBR transmission spectra with different top-cladding refractive indices. These measurements are shown in Fig. 6.5, with insets displaying SW measurements prior to coating, and zoomed-in views of the MP intra-band DBR resonances. Figure 6.6 demonstrates the transmission from fully fabricated samples with 500 nm of deposited $TeO_2$ and 200 nm of subsequently spin-coated PMMA. The calculated quality factors are indicated for the samples intended for subsequent sensor measurements. The quality factors in Fig. 6.6 are calculated using the ratio of the resonance wavelength to the full width at half maximum (FWHM) for intra-band resonances, which have bandwidths in the pm range. Table 6.1 summarizes these measurements including details on the resonant spectra and calculated grating properties for each structure. For each resonance shown in Figs. 6.5 and 6.6 the measured and calculated FWHM, extinction ratio (ER) and central wavelength is also listed in Table 6.1.

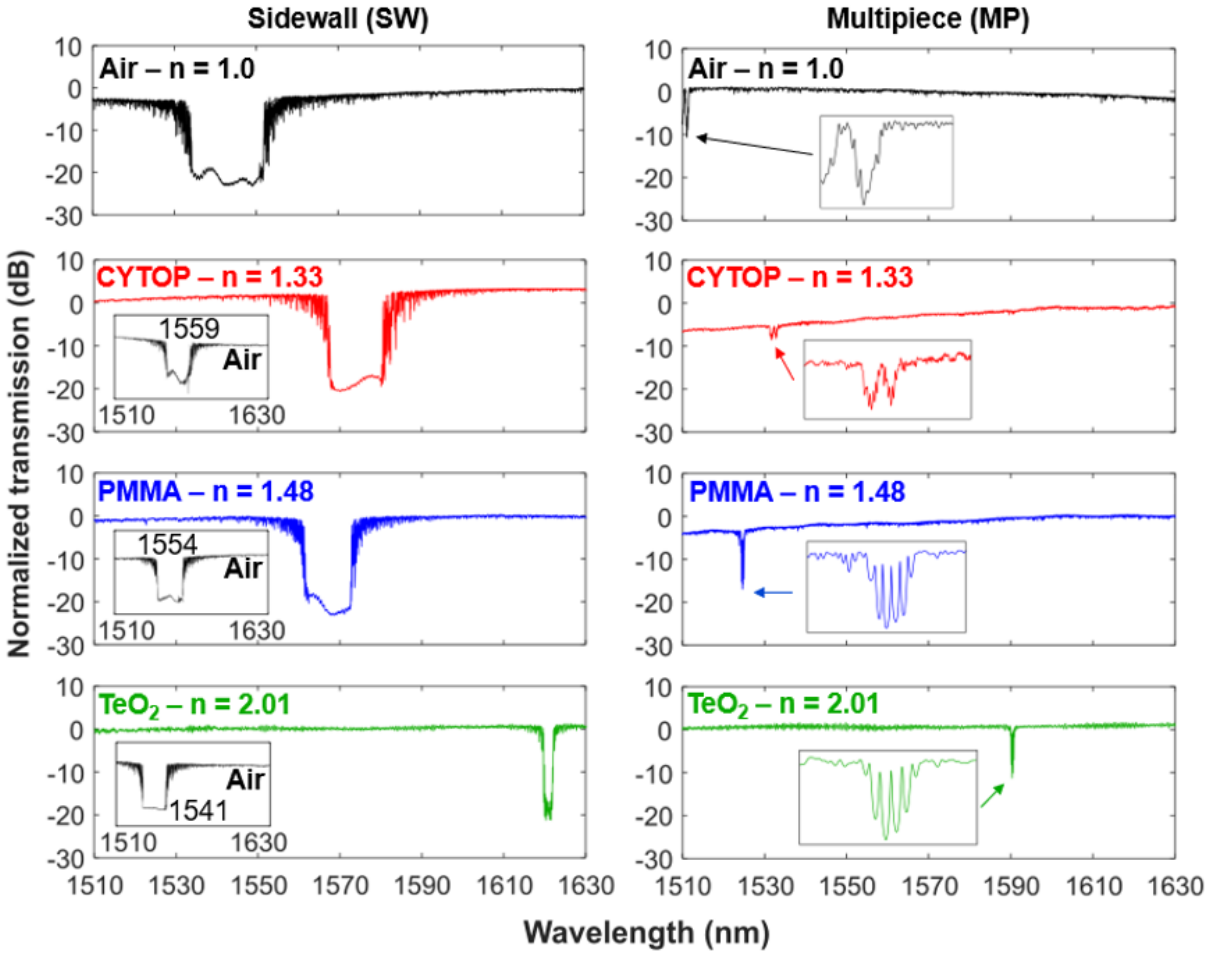


**Figure 6.5.** Comparison of spectra collected from MP and SW DBR resonances with different top-cladding materials, including air, CYTOP, PMMA and $TeO_2$ with thicknesses of N/A, 500, 800 and 900 nm respectively.

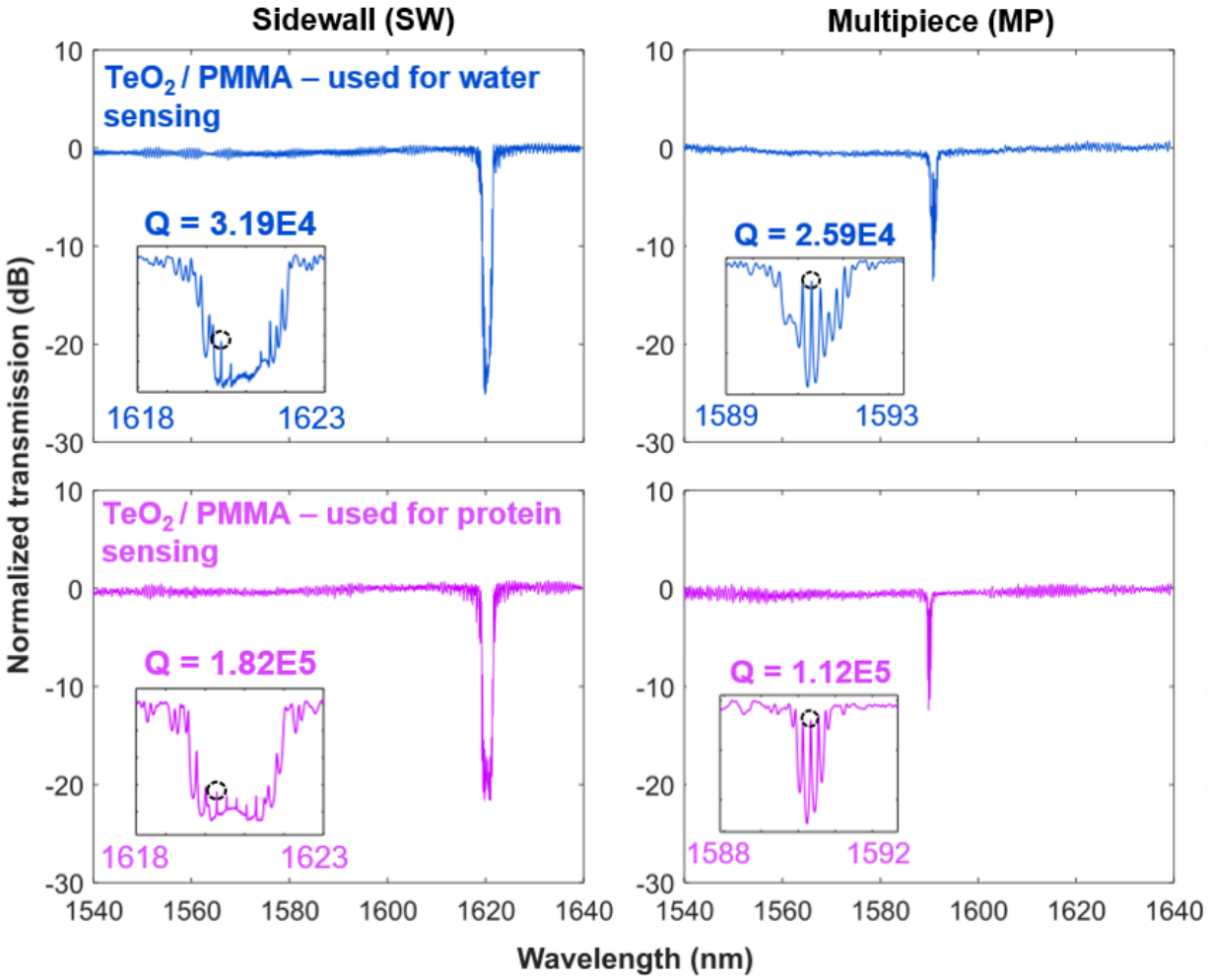


**Figure 6.6.** Transmission spectra for $TeO_2$- and PMMA-coated MP and SW DBRs on two samples, used for water sensing and protein sensing separately. The insets show close-up views of the resonances. The quality factors are calculated using the ratio of the wavelength to the FWHM of the indicated resonances with black dotted circles.

**Table 6.1.** Summary of calculated and measured properties of fabricated SW and MP DBR waveguides.

| Design | | Calculation | | | | | Measurement | |
|---|---|---|---|---|---|---|---|---|
| **Cladding [index, thickness (nm)]** | **Grating** | **$N_{eff}$** | **Power in gratings (%)** | **Grating strength, $\kappa$ ($\times 10^5$ $m^{-1}$)** | **FWHM (nm)** | **ER (dB)** | **Central $\lambda$ (nm)** | **FWHM (nm)** |
| Air (1.0) | SW | 2.49 | 1.65 | 5.47 | 0.40 | 21.5 | 1541.7 | 19.9 |
| | MP | 2.20 | 0.01 | 3.35 | 0.47 | 11.4 | 1510.6 | 2.43 |
| CYTOP (1.33, 950) | SW | 2.52 | 2.04 | 4.98 | 0.41 | 21.6 | 1574.0 | 14.1 |
| | MP | 2.24 | 0.03 | 3.26 | 0.48 | 6.6 | 1532.4 | 1.62 |
| PMMA (1.48, 800) | SW | 2.54 | 2.26 | 4.59 | 0.40 | 23.2 | 1566.4 | 11.0 |
| | MP | 2.29 | 0.04 | 3.05 | 0.46 | 14.5 | 1524.7 | 0.64 |
| $TeO_2$ (2.05, 500) | SW | 2.63 | 3.28 | 2.82 | 0.42 | 21.7 | 1620.8 | 2.42 |
| | MP | 2.39 | 0.31 | 1.84 | 0.48 | 12.2 | 1590.3 | 0.71 |
| $TeO_2$ / PMMA (2.05, 500 / 1.48, 200) | SW | 2.63 | 3.27 | 2.80 | 0.42 | 23.4 | 1620.8 | 2.20 |
| | MP | 2.42 | 0.25 | 1.86 | 0.47 | 14.5 | 1591.4 | 0.90 |

The results demonstrate sharp and narrow resonance spectra for MP gratings with wider and deeper resonances for SW DBRs. In some cases, split resonances are observed as is the case for CYTOP in Fig 6.5. This can be due to counter propagating modes of slightly varying loss, asymmetry in the fabrication process or a variety of other effects from processing the samples. An estimation of the devices' resonant wavelength was made to design the gratings for the S-L telecommunication band for a variety of coating materials. The calculated FWHM are displayed in Table 6.1, following procedure outlined in [27] using the penetration length of the mode into the grating for $Al_2O_3$ DBRs. These were found to be 0.43 and 1.8 nm lower than measurement data for $TeO_2$/PMMA MP and SW devices, respectively, with overestimations for air and polymer clad devices (10+ nm). This is likely due to differences between the designed and simulated structures, and those realistically defined during fabrication. Matrix methods were not used to

calculate the reflectivity spectrum of the resonators, which is suggested for future work to obtain calculated ERs and causes for deviation from design to operation for the devices.

In order to gain insight into the properties of the fabricated DBRs and study pathways for future improved designs, the optical mode profiles, effective indices, optical intensity overlap with the different waveguide materials, and modal areas are plotted in Figs. 6.7 a) and b), c) and d), e) and f) and as insets in Fig. 6.7 c) and d), respectively. In the plots the $TeO_2$ film thickness is variable, in order to consider potential active sensor designs, which would require careful optimization of the mode overlap with both the gain medium (doped $TeO_2$) and the sensing medium (PBS). The higher effective index in the SW DBR designs is due to the mode being heavily confined to the Si bus, which also leads to a smaller modal area and less overlap with the sensing region and $TeO_2$ layer. In contrast, the MP grating pieces pull the mode further away from the bus causing a larger modal area and subsequent higher modal overlap in the $TeO_2$ and top PMMA layer and analyte for sensing. Here the difference in overlap can be observed between the materials which constitute the DBR sensor for the SW and MP design. The most crucial changes are in the Si gratings and $TeO_2$ layer, which vary from 3.0 and 19.5 to 0.53 and 30.4 % partial power overlap between the SW to MP design, respectively, when coated with 500 nm of $TeO_2$. Although a longer cavity is needed to achieve comparable grating strengths to the SW design, MP designs provide a useful tradeoff for active sensors where not only the surface overlap is crucial for performance, but the hybrid material surrounding the Si waveguide core is required to have high optical overlap. By tuning parameters like the Si bus width, DBR grating piece width and gap, $TeO_2$ thickness, and PMMA thickness the

design can be tuned to optimize for increased sensitivity and overlap with the analyte or in this case PBS liquid layer.

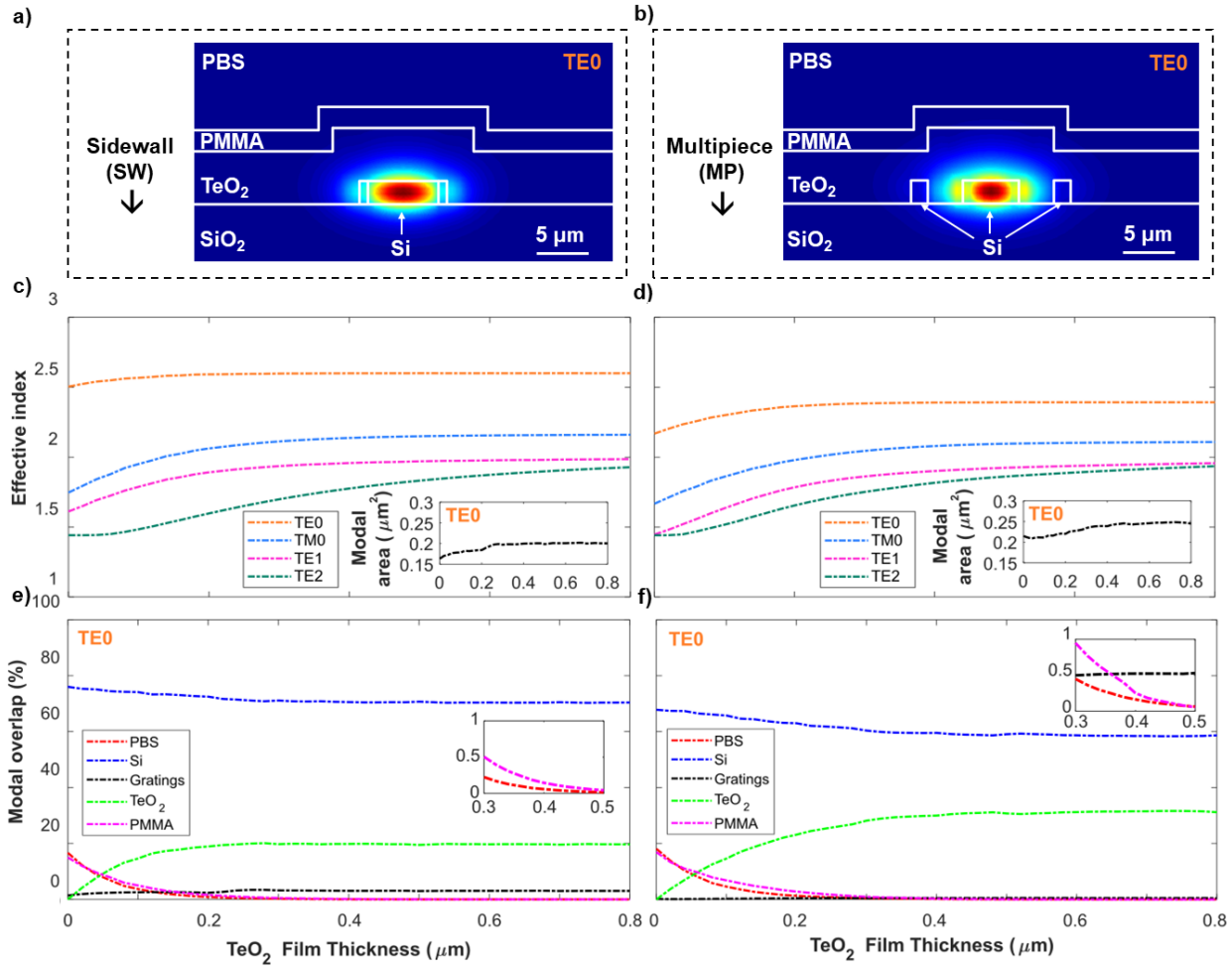


**Figure 6.7.** Transverse electric field profile for (a) SW and (b) MP grating designs for a $TeO_2$ and PMMA thickness of 500 and 200 nm, respectively. Effective indices for (c) SW and (d) MP waveguide gratings for the first four modes with inset fundamental modal area for varying $TeO_2$ thickness. Partial power overlap for the fundamental transverse electric (TE0) mode in (e) SW and (f) MP waveguide grating materials and inset closeup of PBS sensing fluid, PMMA, and grating overlaps for $TeO_2$ film thicknesses of interest.

### 6.3.2 Plasma Functionalization

To quantify the impact of plasma exposure for functionalization, liquid drop water contact angle measurements were carried out on PMMA films on 3-inch Si wafers using a ramé-hart goniometer characterization system following the procedure outlined in previous work [28]. The plasma exposure was carried out using $O_2$ at a pressure of 750 mTorr with 27.5 W of forward power at varying times. The $O_2$ plasma treatment was anticipated to impart oxygen-based functional groups with increased energy on the PMMA surface, which in turn can increase hydrophilicity. Increased hydrophilicity can be observed by a decreased contact angle when a water droplet comes into contract with the top surface. The results are shown in Fig. 6.8, demonstrating a ~40° decrease in contact angle after 5 minutes of plasma treatment which shows a distinct transition from a hydrophobic to a hydrophilic surface.

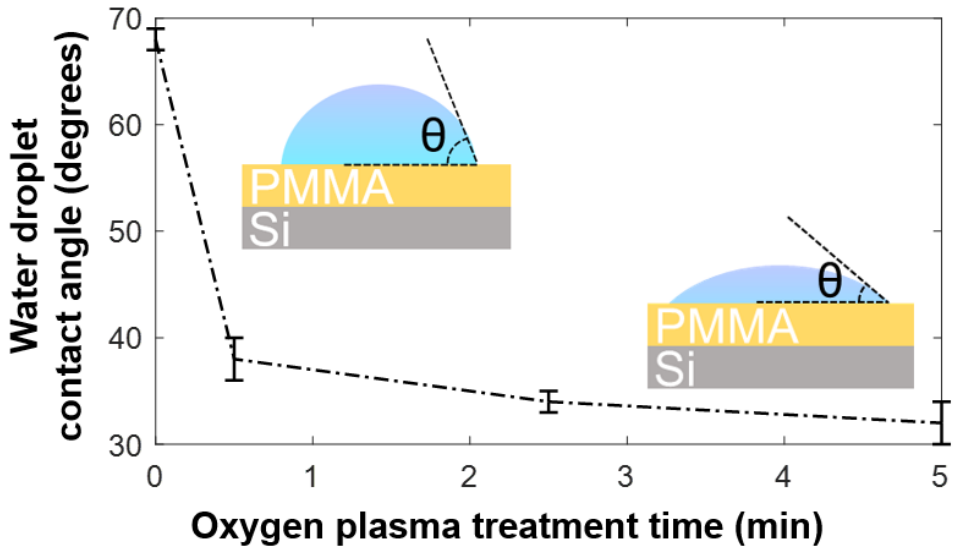


**Figure 6.8.** Water droplet contact angle as a function of oxygen plasma treatment for 200-nm-thick PMMA films on silicon substrates with inset drawings illustrating different contact angles.

After verifying the surface activation via water droplet measurements on Si wafers, the $TeO_2$ and PMMA coated DBR samples corresponding to the measurements in Fig. 6.6 were treated with plasma. A 1-minute exposure was used for the DBR chip treatment based on the limited change in contact angle for longer times and because additional plasma exposure times might prove damaging to the $TeO_2$ layer beneath the relatively thin PMMA layer. The samples were measured before and immediately after functionalization to ensure significant surface scattering or absorption losses were not introduced and the optical transmission spectra of the DBRs were found to be relatively unaffected by the plasma treatment. Figure 6.9 shows this comparison and confirms a negligible difference in the optical transmission of the hybrid Si-$TeO_2$/PMMA DBR device, with zoomed in inset highlighting the similarity and overlap of intra-band DBR resonances before and after plasma treatment. These results suggest the imparted chemical functionalization of the surface layer of the PMMA is not deleterious to the optical performance of our sensors.

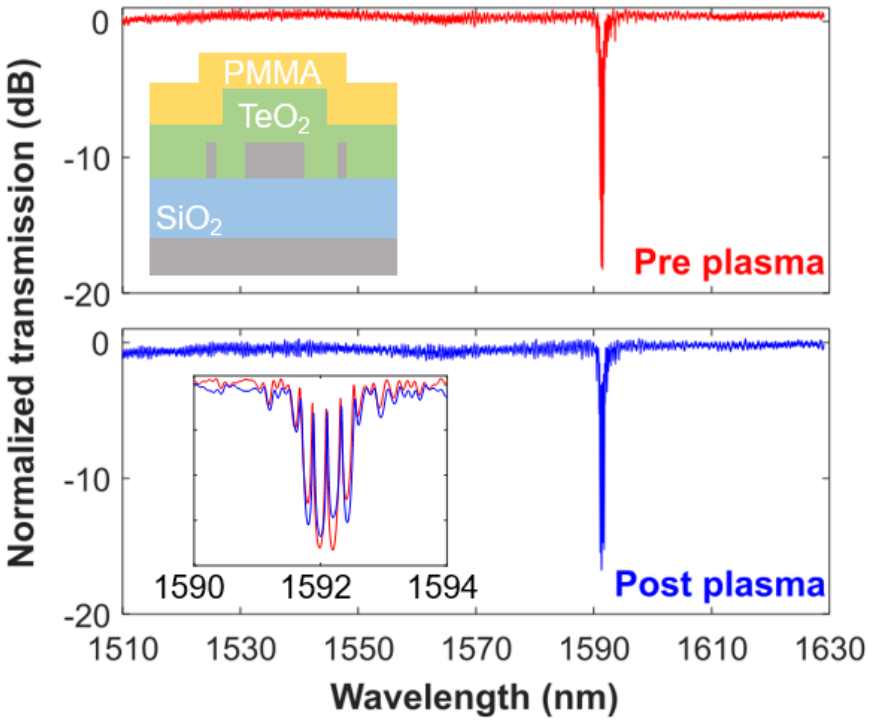


**Figure 6.9.** Comparison of a DBR transmission spectrum measured on the same sample before and after plasma treatment, demonstrating a negligible impact on the optical performance. Insets: cross sectional drawing of the MP DBR measured (top) and close-up of DBR responses pre- and post-plasma treatment at 1590 nm (bottom).

### 6.3.3 Thermal Sensing

To investigate the Si-$TeO_2$/PMMA DBR as a temperature sensor, a sample was placed on a stage with a copper mount and Peltier cooler while the resonance was tracked during heating from 25 to 50 °C. To obtain each data point, a feedback circuit maintained the desired stage temperature for 5 minutes before taking an optical measurement. The results are displayed in Fig. 6.10, with a photograph of the sample during the test shown in the inset.

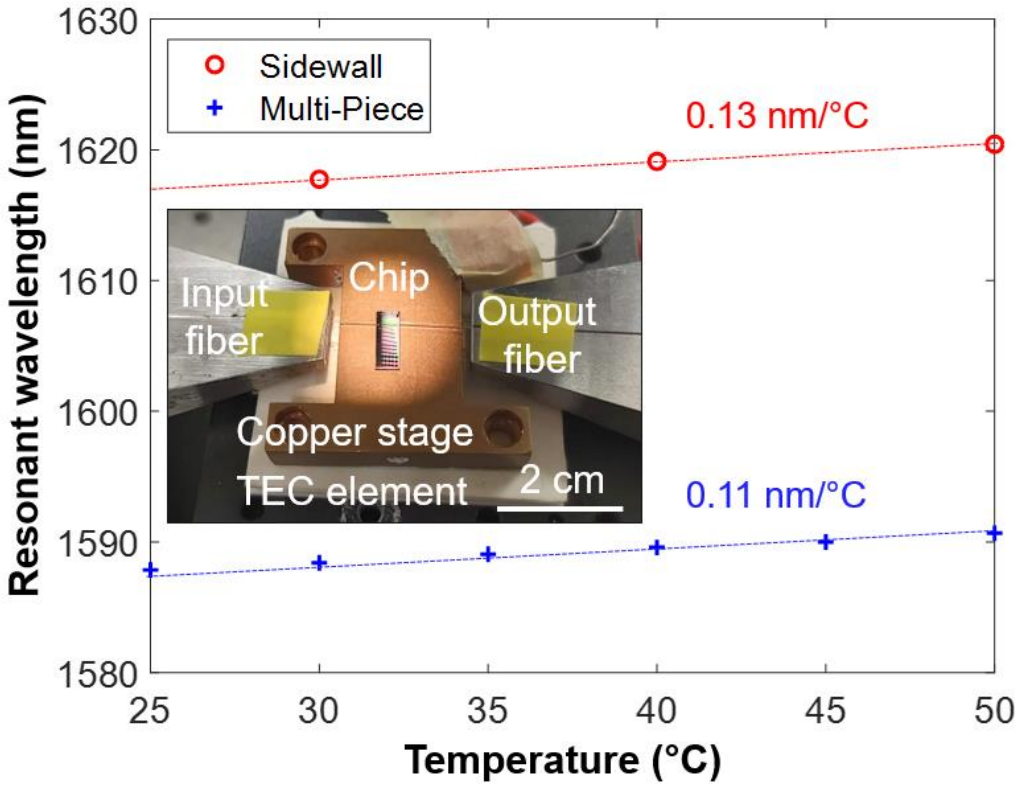


**Figure 6.10.** Central resonant wavelength shift as a function of temperature for SW and MP waveguide gratings and inset photograph of sample during test with TEC element and copper stage for thermal control.

Figure 6.10 demonstrates a thermal sensitivity which is almost identical for both designs, but higher for the SW case, where the optical overlap with the Si layer and grating pieces is higher, and therefore has more interaction with the high thermo-optic coefficient Si material. The thermal resonance shift is caused by a combination of the materials' thermal expansion and the overall thermo-optical effect which is primarily influenced by the thermo-optic coefficients and mode overlap with the Si and $TeO_2$ layers. The thermo-optic coefficients of bulk Si and $TeO_2$ are 1.8 and $0.7 \times 10^{-4}$ respectively. The other materials such as $SiO_2$ and PMMA do not have a significant impact because of their relatively lower thermo-optic coefficients. The thermo-optic coefficient ($\sigma_T$) of the sensors

was calculated using the measured thermal sensitivity ($S_T = \Delta\lambda/\Delta T$), measured resonant wavelength ($\lambda_0$), and calculated group index ($n_g$) which depends on the calculated dispersion of the fundamental mode: $n_g = n_{eff} + \lambda_0(dn_{eff}/d\lambda)$. This yields a result of $n_g$ = 3.39 and 3.22, and subsequently using $\sigma_T = S_T(n_g/\lambda_0)$, leads to a $\sigma_T$ of 2.74 and 2.23 × $10^{-4}$ $°C^{-1}$ at 1610 and 1590 nm for SW and MP gratings, respectively. For both devices this demonstrates a result slightly higher than the thermo-optic coefficient of Si, and well above results reported for $TeO_2$ [29]. Although PMMA and $TeO_2$ have less prominent contributions to thermal sensitivity on this platform, their thermal stability is the limiting factor in applications of these sensors in high temperature environments. $TeO_2$ and PMMA have known temperature limits of approximately 200°C [30,31], which still makes them suitable for applications in the biological domain where temperatures at these scales are not relevant for the study of biological interactions. Here, a relatively high thermal sensitivity is demonstrated compared to other $TeO_2$ integrated sensors [22], and Bragg gratings [32], [33], on the SOI platform, which can be considered an advantage or drawback depending on the sensing application and the relative importance of noise factors and environmental fluctuations. In future designs with higher optical overlap in the $TeO_2$ and sensing layer it is anticipated that lower thermal sensitivities can be achieved.

### 6.3.4 Liquid Sensing

Liquid sensing was carried out with deionized (DI) water and PBS as a solution for diluting BSA protein. As shown in many demonstrations [1,2,4], PDMS, PMMA cap layers or SU-8 microfluidic structures can selectively deliver liquid to channels and specific waveguides or arrays on the chip. These delivery channels can in theory be easily integrated into our sensing scheme with PMMA already being the top layer and acting as a cap layer for a functionalized surface. However, for the purposes of this study, liquids were simply

dropped onto the surface of the sample during the test without control of the flow or volume of liquid. DI water was used to determine the sensors' bulk sensitivity using the well-known relation $S_{bulk} = \Delta\lambda/\Delta n_{liquid}$ which leads to a result of 10.2 and 0.16 nm/RIU from a shift of 3.3 and 0.05 nm for MP and SW DBRs, respectively. The reduced water droplet contact angle from plasma treatment did not lead to an increased shift from evanescent interaction with the DBR mode, because the droplet covered the entire device in both cases. The plasma enabled hydrophilicity was noticed during measurement however, the water did not bead to the surface of the PMMA, but rather stuck and formed a film on the top of the sensor after treatment. The water sensing measurement process is depicted in Fig. 6.11 a), while Fig. 6.11 b) shows the transmission measurements before and after plasma treatment with water coverage, and Fig. 6.11 c) shows images of the sample in air and during water sensing.

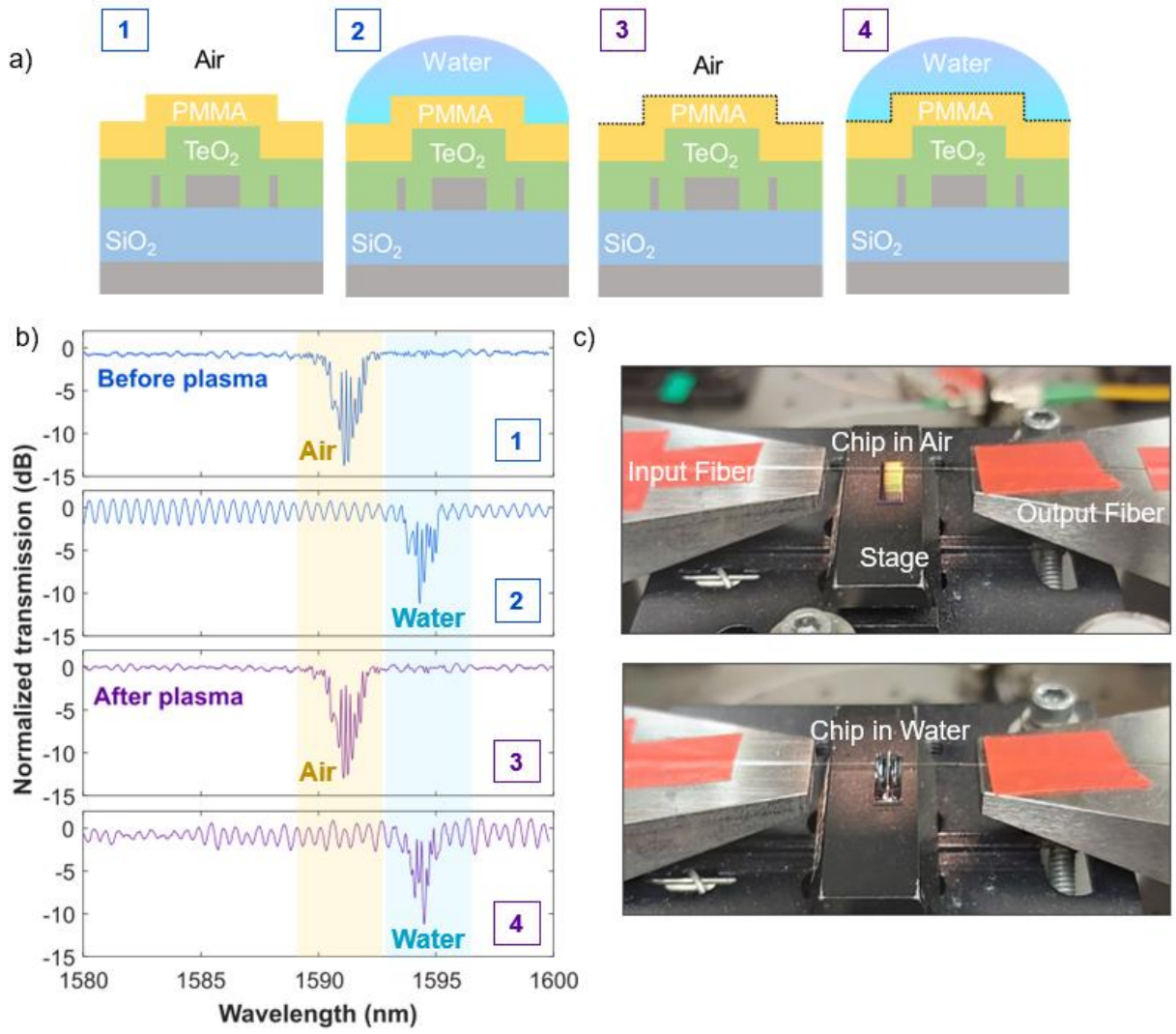


**Figure 6.11.** (a) Cross section of measurement and fabrication steps and (b) corresponding labelled transmission spectra obtained from the MP DBR grating shown in Fig. 6.8, showing a shift of 3.3 nm in water with and without plasma treatment. (c) Images of the chip with plasma treatment during measurement in air and water.

The SW DBRs demonstrated two orders of magnitude lower sensitivity compared to MP DBRs under water exposure. This can be attributed to the reduced modal overlap with the water (0.016 vs. 0.064 % for SW and MP devices, respectively). When considering future sensor devices with similar designs and rare-earth doped oxide layers

that also operate as a laser, excess loss due to increased overlap with the analyte, especially water, needs to be considered and balanced in the design in order to maintain high *Q* factors. To determine the limit of detection (LoD), the relation LoD = $1/QS_{bulk}$ was used. The MP and SW DBRs demonstrated limits of detection of 60.0 and ~300 $\times 10^{-4}$ RIU, respectively. Table 6.2 compares the figures of merit and properties of various Si DBR and distributed feedback (DFB) devices, including their sensitivity, LoD, sensing quality (*Q*) factor, wavelength, and waveguide structure. Here we have focused on SOI-based devices which have also reported sensitivities based on liquid sensing. The sensitivities and limits of detection reported here are lower than state-of-the-art silicon photonic evanescent field sensors shown in the table. However, we show similar or higher Q factors and the addition of $TeO_2$ and PMMA layers demonstrates a functional hybrid sensor platform which can in future allow for rare-earth laser biological sensors on the SOI platform.

**Table 6.2.** Various Si DBR and DFB sensing demonstrations (*calculated).

| **Waveguide details [material/device]** | **Wavelength/ polarization (nm)** | **Sensing analyte (bulk/surface)** | ***Q* factor [$10^3$]** | **Bulk sensitivity (nm/RIU)** | **LoD (RIU) [$10^{-4}$]** | **Ref** |
|---|---|---|---|---|---|---|
| PMMA-PDMS-SOI / SWG MP DFB | 1550 / TE | NaCl / polymer assay | ~8.0 | 579.2 | 3.6 | [34] |
| SOI / Slot DFB | 1550 / TE | NaCl / biomolecules | 15.0 | 340.0 | 3.0 | [35] |
| PDMS-SOI / Strip DFB | 1517 / TE | NaCl / b-Biotin streptavidin | 27.6 | 59 | 9.3 | [36] |
| PDMS-SOI / Slot DFB | 1530 / TE | NaCl / b-Biotin streptavidin | 15.0 | 340 | 3.0 | [36] |
| PMDS-SOI / Strip SW Uniform | 1552 / TE | Water / N/A | N/A | 0.05* | N/A | [37] |
| PMMA-$TeO_2$-SOI / Strip MP DBR | 1590 / TE | Water / BSA | 25.9 | 10.2 | 60 | This work |
| PMMA-$TeO_2$-SOI / Strip SW DBR | 1610 / TE | Water / N/A | 31.9 | 0.16 | ~300 | This work |

### 6.3.5 Protein Sensing

Protein sensing was investigated using BSA in PBS buffer solution. A PBS baseline was first measured before incubation with the BSA, which showed a permeant change in the resonance (~1.0 nm redshift) of the MP DBR Si-$TeO_2$/PMMA sensor. 2.0 µg/mL of BSA was then diluted into the PBS buffer solution and the functionalized sample was incubated in it for 1 hour. The chip was then measured after being flushed with PBS to ensure excess proteins were removed from the surface and only attached proteins were measured. This resulted in a 1.6 nm shift attributable to protein immobilization on the surface of the PMMA for the MP DBR. SDS was used afterwards to strip the proteins from the surface of the sensor, which demonstrated a recovery of the initial baseline resonant wavelength. Two MP samples were tested and measurements were carried out to ensure repeatability of the result and the requirement of $O_2$ plasma functionalization for BSA immobilization. No noticeable shift was detected for the SW resonances. This is due to the lower sensitivity in SW devices as shown via water sensing. The protein sensing measurement process and the results from each step are displayed for the MP DBR sensor in Fig. 6.12.

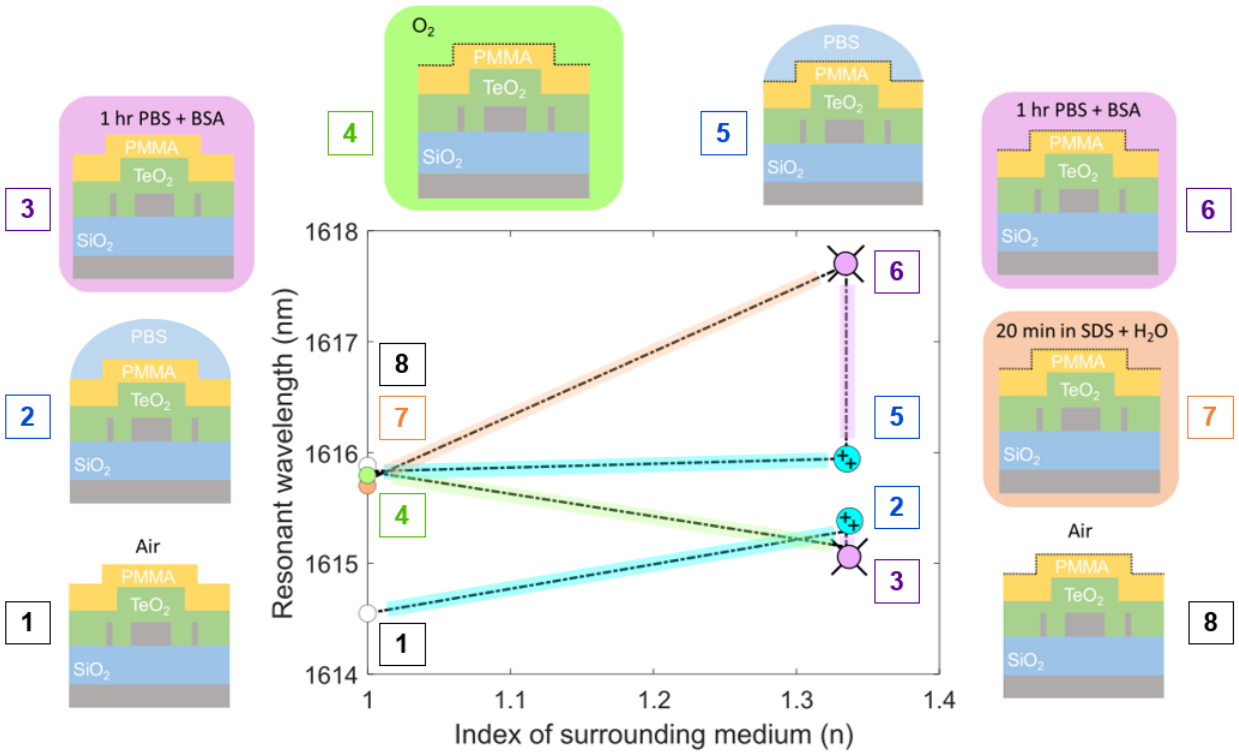


**Figure 6.12.** Central resonant wavelength shift for different measurement steps during protein sensing for top layer changes from 1) air, 2) PBS baseline, 3) PBS + BSA immersion, 4) air after acetone clean and $O_2$ plasma functionalization, 5) PBS rinsing, 6) PBS + BSA immersion with functionalization and protein immobilization, 7) air after SDS immersion and protein stripping, and 8) air repeated 1 hour after.

The plasma functionalized PMMA layer used here can remove the need for an initial chemical functionalization step, which sometimes requires biotin for selective attachment or harmful chemicals such as toluene, and is distinct from other functionalization methods applied in biological sensing studies on Si [34]. This manner of functionalization allows for the direct chemisorption and immobilization of blocking proteins by the interaction of molecules such as BSA to the oxygen-based functional sites provided by the plasma treated PMMA surface. Compared to physisorption, this functionalization strategy and immobilization through chemisorption allows for a decreased chance for the proteins to

denature on the surface [24]. This provides a more robust and stable surface for the subsequent detection of antibodies, viruses and other biologically relevant species which require detection in biological fluids such as blood [38]. With the added ability of hydrophilicity control, $O_2$-plasma functionalized PMMA's inclusion in the hybrid sensor stack enables liquid-based sensing for the biological domain using resonators with active sensing potential. Direct plasma functionalization of PMMA, as a top layer on Si-$TeO_2$ DBR resonators provides a novel platform for the sensing of proteins via specific and non-specific binding in silicon photonic circuits.

Without real-time measurements, control of the flow and concentration and monitoring of the binding events for the BSA, a concentration minimum study [34] or Langmuir dissociation constant calculation [39] is not carried out here. Future work will focus on measurement technique optimization in order to properly assess changing concentrations and monitoring in real time of resonant wavelengths. In addition, improved hybrid sensor designs will be investigated based on this initial demonstration. Using plasma functionalized PMMA as a biological interface layer in combination with rare-earth doped $TeO_2$ is a novel prospective approach to hybrid laser sensors for silicon photonic platforms. More generally, a direct approach of functionalization to achieve immobilization and detection of proteins on a polymer surface opens many pathways for novel handheld silicon photonic devices and sensors.

### 6.4 Conclusion

We have demonstrated the fabrication and characterization of a PMMA coated Si-$TeO_2$ hybrid DBR waveguide sensor for biological applications. Two Si DBR designs were designed and fabricated using a standard silicon photonic foundry process, which enables low cost, volume production. The transmission response of the DBRs was investigated

around 1550 nm for a variety of top-cladding materials and the quality factors for PMMA coated Si-$TeO_2$ devices were calculated yielding values of 1.82 and 1.12 × $10^5$ for SW and MP devices respectively. Plasma functionalization of the PMMA surface was carried out and characterized via water droplet contact angle and transmission measurements, demonstrating a decrease in angle from 70 to 35° and minimal effect on the optical spectra of the DBRs, respectively. Thermal sensing was performed demonstrating a shift of 0.13 and 0.11 nm/°C for SW and MP DBRs respectively, over a temperature range of 25–50 °C. Liquid sensing was performed with DI water in order to calculate the bulk sensitivities of the MP and SW devices. Resonance shifts of 0.05 and 3.2 nm were measured, which correspond to sensitivities of 0.16 and 10.2 nm/RIU for SW and MP DBRs respectively. MP DBR devices were then used to demonstrate the immobilization of blocking proteins using PBS as a buffer solution with a BSA concentration of 2 µg/mL. It was observed that plasma functionalization is required to detect a shift after incubation with the protein solution, suggesting the binding is taking place on the PMMA functionalized surface via chemisorption. Using an SDS stripping solution, the sensor's original resonant condition was recovered after sensing, suggesting potential re-use of single devices. These Si-$TeO_2$ hybridized DBRs coated in plasma treated PMMA demonstrate a pathway towards improved functionalized devices for protein sensing applications and the potential for active resonator sensors based on rare-earth-doped $TeO_2$ layers on silicon photonic chips.

### 6.5 References

1. L. Chrostowski, S. Grist, J. Flueckiger, W. Shi, X. Wang, E. Ouellet, H. Yun, M. Webb, B. Nie, Z. Liang, K.C. Cheung, S.A. Schmidt, D.M. Ratner, N. A. F. Jaeger "Silicon photonic resonator sensors and devices," Laser Reson. Microresonators, Beam Control XIV, vol. 8236, p. 823620, 2012.

2. E. Luan, H. Shoman, D. M. Ratner, K.C. Cheung, L. Chrostowski, “Silicon photonic biosensors using label-free detection,” Sensors (Switzerland), vol. 18, no. 10, pp. 1–42, 2018.
3. K. De Vos, I. Bartolozzi, E. Schacht, P. Bienstman, and R. Baets, “Silicon-on-Insulator microring resonator for sensitive and label-free biosensing,” vol. 15, no. 12, pp. 7610–7615, 2007.
4. A. F. Gavela, D. G. García, J. C. Ramirez, and L. M. Lechuga, “Last advances in silicon-based optical biosensors,” Sensors (Switzerland), vol. 16, no. 3, pp. 1–15, 2016.
5. S. Schmidt, J. Flueckiger, W. Wu, S.M. Grist, S. Talebi Fard, V. Donzella, P. Khumwan, E.R. Thompson, Q. Wang, P. Kulik, X. Wang, A. Sherwali, J. Kirk, K.C. Cheung, L. Chrostowski, D. Ratner., “Improving the performance of silicon photonic rings, disks, and Bragg gratings for use in label-free biosensing,” Biosensing Nanomedicine VII no. 916660M-1, 2014.
6. A. M. Shrivastav, U.Cvelbar and I. Abdulhalim, “A comprehensive review on plasmonic-based biosensors used in viral diagnostics,” Comm. Biology, vol. 4 no. 70 pp. 1–12, 2021.
7. S. M. Lo, S. Hu, G. Gaur, Y. Kostoulas, S. M. Weiss, and P. M. Fauchet, “Photonic crystal microring resonator for label- free biosensing,” Opt. Express, vol. 25, no. 6, pp. 7046–7054, 2017.
8. S. Kaushal, R. Cheng, M. Ma, A. Mistry, M. Burla, L. Chrostowski, and J. Azaña, “Optical signal processing based on silicon photonics waveguide Bragg gratings : review,” Front. Of Opt. vol. 11, no. 2, pp. 163–188, 2018.
9. T. Reynolds, N. Riesen, A. Meldrum, X. Fan, J.M.M. Hall, T.M. Monro, A. François “Fluorescent and lasing whispering gallery mode microresonators for sensing applications,” Laser Photonics Rev., vol. 11, no. 2, pp. 1–20, 2017.
10. L. Agazzi, J. D. B. Bradley, M. Dijkstra, F. Ay, G. Roelkens, R. Baets, K. Wörhoff, M. Pollnau, “Monolithic integration of erbium-doped amplifiers with silicon-on-insulator waveguides,” Opt. Express, vol. 18, no. 26, p. 27703, 2010.
11. K. M. Kiani, H. C. Frankis, C. M. Naraine, D. B. Bonneville, A. P. Knights, and J. D. B. Bradley, “Lasing in a hybrid rare-earth silicon microdisk,” Laser Photonics Rev., vol. 16, no. 1, 2022.
12. N. Li, M. Xin, Z. Su, E.S. Magden, N. Singh, J. Notaros, E. Timurdogan, P. Purnawirman, J. D. B. Bradley, M. R. Watts “A silicon photonic data link with a monolithic erbium-doped laser,” Sci. Rep., vol. 10, no. 1, pp. 1–9, 2020.
13. L. He, Ş. K. Özdemir, J. Zhu, W. Kim, and L. Yang, “Detecting single viruses and nanoparticles using whispering gallery microlasers,” Nat. Nanotechnol., vol. 6, no. 7, pp. 428–432, 2011.
14. E. P. Ostby and K. J. Vahala, “Yb-doped glass microcavity laser operation in water,” Opt. Lett., vol. 34, no. 8, p. 1153, 2009.
15. E.H. Bernhardi, K.O. van der Werf, A.J.F. Hollink, K. Wörhoff, R.M. de Ridder, V. Subramaniam, and M. Pollnau, “Intra-laser-cavity microparticle sensing with a dual-wavelength distributed-feedback laser,” Laser Photonics Rev., vol. 7, no. 4, pp. 589–598, 2013.

16. M. de Goede, M. Dijkstra, R. Obregón, J. Ramón-Azcón, E. Martínez, L. Padilla, F. Mitjans, and S.M. Garcia-Blanco "$Al_2O_3$ microring resonators for the detection of a cancer biomarker in undiluted urine ," Opt. Express, vol. 27, no. 13, p. 18508, 2019.
17. M. Goede, L. Chang, J. Mu, M. Dijkstra, R. Obregón, E. Martínez, L.Padilla, F. Mitjans, and S. M. Garcia-Blanco "$Al_2O_3$:$Yb^{3+}$ integrated microdisk laser label-free biosensor," Opt. Lett., vol. 44, no. 24, pp. 5937–5940, 2019.
18. M. Goede, M. Dijkstra, L. Chang, N. Acharyya, G. Kozyreff, R. Obregón, E. Martínez, S. M. García-Blanco "Mode-splitting in a microring resonator for self-referenced biosensing," Opt. Express, vol. 29, no. 1, pp. 346–358, 2021.
19. S. J. Madden and K. T. Vu, "Very low loss reactively ion etched Tellurium Dioxide planar rib waveguides for linear and non-linear optics," Opt. Express, vol. 17, no. 20, pp. 369–373, 2009.
20. K. Vu and S. Madden, "Tellurium dioxide Erbium doped planar rib waveguide amplifiers with net gain and 2 . 8dB / cm internal gain," Opt. Express, vol. 18, no. 18, pp. 19192–19200, 2010.
21. K. M. Kiani, D. B. Bonneville, A. P. Knights, and J. D. B. Bradley, "High-Q $TeO_2$–Si hybrid microring resonators," Appl. Sci, vol. 12 no. 3 pp. 1363 2022.
22. H. C. Frankis, D. Su, D. B. Bonneville, and J. D. B. Bradley, "A tellurium oxide microcavity resonator sensor integrated on-chip with a silicon waveguide," Sensors, vol. 18, pp. 4061, 2018.
23. R. Landgraf, M. K. Kaiser, J. Posseckardt, B. Adolphi, and W. J. Fischer, "functionalization of polymer sensor surfaces by oxygen plasma treatment," Procedia Chem., vol. 1, no. 1, pp. 1015–1018, 2009.
24. S. Sathish, N. Ishizu, and A. Q. Shen, "Air plasma-enhanced covalent functionalization of poly(methyl methacrylate): High-throughput protein immobilization for miniaturized bioassays," ACS Appl. Mater. Interfaces, vol. 11, no. 49, pp. 46350–46360, 2019.
25. X. Wang, W. Shi, H. Yun, S. Grist, N. A. F. Jaeger, and L. Chrostowski, "Narrow-band waveguide Bragg gratings on SOI wafers with CMOS-compatible fabrication process," Opt. Express, vol. 20, no. 14, pp. 3013–3015, 2012.
26. H. C. Frankis, K. Miarabbas Kiani, D. B. Bonneville, C. Zhang, S. Norris, R. Mateman, A. Leinse, N. D. Bassim, A. P. Knights, and J. D. B. Bradley, "Low-loss TeO 2 -coated Si 3 N 4 waveguides for application in photonic integrated circuits," Opt. Express, vol. 27, no. 9, p. 12529, 2019.
27. E. H. Bernhardi, "Bragg-grating-based rare-earth-ion-doped channel waveguide lasers and their applications," University of Twente, 2012.
28. T. Huhtamäki, X. Tian, J. T. Korhonen and R. H. A. Ras "Surface-wetting characterization using contact-angle measurements," Nat. Protoc., vol. 13, pp. 1521–1538, 2018.
29. T. Honma, N. Ito, T. Komatsu, and V. Dimitrov, "Thermo-optic properties and electronic polarizability in alkali tellurite glasses," J. Am. Ceram. Soc., vol. 93, no. 10, pp. 3223–3229, 2010.
30. R. A. H. El-Mallawany, Tellurite glasses handbook: physical properties and data, Second Edition, CRC Press 2002.

31. U. Ali, K. J. Bt. A. Karim and N. A. Buang, “A review of the properties and applications of poly (Methyl Methacrylate) (PMMA),” Polym. Rev., vol. 55, no. 4, pp. 678–705, 2015.
32. N. N. Klimov, S. Mittal, M. Berger, and Z. Ahmed, “On - chip silicon waveguide Bragg grating photonic temperature sensor,” Opt. Lett., vol. 40, no. 17, pp. 4–7, 2015.
33. G. Kim, H. Lee, C. Park, S. Lee, B. Lim, H. Bae, and W. Lee, “Silicon photonic temperature sensor employing a ring resonator manufactured using a standard CMOS process,” Opt. Express, vol. 18, no. 21, pp. 22215–22221, 2010.
34. E. Luan, H. Yun, M. Ma, D.M. Ratner, K.C. Cheung, L. Chrostowski, “Label-free biosensing with a multi-box sub-wavelength phase-shifted Bragg grating waveguide,” Biomed. Opt. Express, vol. 10, no. 9, pp. 4825–4838, 2019.
35. X. Wang, S. Grist, J. Flueckiger, N. A. F. Jaeger, and L. Chrostowski, “Silicon photonic slot waveguide Bragg gratings and resonators", Opt. Express, vol. 21, no. 16, pp. 19029–19039, 2013.
36. S. T. Fard, S. M. Grist, V. Donzella, S. A. Schmidt, J. Flueckiger, X. Wang, W. Shi, A. Millspaugh, M. Webb, D. M. Ratner, K. C. Cheung, and L. Chrostowski, “Label-free silicon photonic biosensors for use in clinical diagnostics,” Silicon Photonics VIII, vol. 8629, p. 862909, 2013
37. A. S. Jugessur, J. Dou, J. S. Aitchison, R. M. De La Rue, and M. Gnan, “A photonic nano-Bragg grating device integrated with microfluidic channels for bio-sensing applications,” Microelectron. Eng., vol. 86, no. 4–6, pp. 1488–1490, 2009.
38. K. N. Sask, “Antithrombogenic biomaterials : surface modification with an antithrombin- heparin covalent complex,” McMaster University, 2018.
39. Y. L. and L. Shen, “From Langmuir kinetics to first- and second-order rate Equations for adsorption,” Langmuir, vol. 24, no. 20, pp. 11625–11630, 2008.

# Chapter 7

## Conclusions

### 7.1 Summary

This thesis focused on the realization of various fabrication techniques to realize waveguides in silicon-based materials for passive devices, optical amplifiers and sensors.

ECR-PECVD was shown to provide high optical quality silicon oxynitride thin films, while depositing at low pressures and temperatures which allows for deposition on thermally sensitive substrates. Films up to 650 nm were deposited at 140 °C and 1.5 mTorr demonstrating low visible losses, but higher losses in the C-band influenced by ~15–20% hydrogen incorporation. The lack of requirement for high temperature annealing coupled with losses of < 0.5 dB/cm at 980 nm is promising for NIR applications as well as nonlinear photonics and integration with hybrid layers for active devices. Due to the low deposition temperature, these films could even be deposited on flexible substrates such as polymers.

Maskless UV writing in negative photoresist was demonstrated to lead to controllable features and adjacent gaps with low sidewall roughness. The process was used to fabricate $Si_3N_4$ waveguides using RIE, leading to the demonstration of three passive devices, a 50/50 coupler, a Sagnac loop, and a ring resonator, which exhibited 50/50 coupling at 1510 nm, 20 dB drop at 1580 nm, and a Q factor of ~13,000 at 1576 nm, respectively. Without the need of a new photomask for adjusting designs, the fabrication process is economically of interest for start-up companies or research collaboration opportunities where new materials and device designs are under development. This

process is particularly useful for rapid prototyping of waveguide devices in a flexible manner.

Reactive magnetron sputtering was used to deposit $Al_2O_3:Er^{3+}:Yb^{3+}$ thin films for waveguide amplifiers. Co-doping of Er and Yb was carried out during deposition using solid metallic targets, and patterning of the waveguides was carried out using conventional lithography and wet chemical etching. By using hot phosphoric acid, which is relatively safe to work with and dispose of, and only requires a wet-bench, as an etchant as opposed to chlorine-based RIE, reliable fabrication can still be achieved for a fraction of the price and with reduced safety considerations. The $Al_2O_3:Er^{3+}:Yb^{3+}$ film losses were optimized for pump and signal wavelengths of ~980 and 1530 nm respectively and were also used to determine the rare-earth dopant concentrations. After structuring, the waveguide loss was determined to be 0.5 ± 0.3 dB/cm at 1640 nm and internal net gain of 4.3 ± 0.9 dB was demonstrated at 1533 nm for a 3.0 cm long waveguide when pumped at 970 nm. The amplifiers demonstrate a promising pathway forward for the co-doped $Al_2O_3:Er^{3+}:Yb^{3+}$ material platform which with more optimization is expected to lead to efficient pumping at ~980 nm, and shorter devices in comparison to singly doped $Al_2O_3:Er^{3+}$.

Silicon DBR waveguide resonators were hybridized with $TeO_2$ and coated with PMMA for biological sensing. Water, thermal and protein sensing were demonstrated leading to a limit of detection of $5.9 \times 10^{-3}$ RIU, thermal sensitivity of 0.13 nm/°C and a 1.6 nm shift after BSA attachment from of 2 µg/mL diluted in buffer, respectively. Plasma treatment was shown to increase hydrophilicity and functionalized the polymer on the top surface of the chip allowing for chemisorption and biological sensing. Protein sensing using a

rare-earth compatible host medium ($TeO_2$) represents a significant step towards laser-based sensors for low limits of detection on silicon photonic chips. The $TeO_2$ layer is deposited at room temperature, and heat treatment of the polymer does not exceed 150°C which allows the material stack to be integrated onto a variety of platforms, including silicon photonic active chips with photodetectors, electrical readout and metallic connections for sensing circuits.

## 7.2 Future Work

Future work is recommended for each experimental demonstration in this thesis. These will be discussed individually by chapter with specific steps and procedures that could be optimized, as well as suggested pathways towards worthwhile adjacent projects.

Throughout the deposition process for ECR-PECVD of $Si_3N_4$ there are many factors that influence the optical quality of films. Conditions such as pressure and temperature, relative gas flows, and chamber pre-bake could be further investigated for improving the quality of films deposited. In general, $Si_3N_4$ deposited by ECR-PECVD suffer from losses in the telecommunication bands due to incorporated hydrogen. Minimizing its sources in the process and understanding further its impact on optical loss is recommended for future study. The relative gas flows used could be further adjusted to reduce the amount of hydrogen in the films, such as discovering recipes which use less $SiH_4$. Stoichiometry measurements revealed the presence of unwanted oxygen as well in the films, which points towards water vapour likely being present in the chamber. Due to the transfer of samples in the top mounted load-lock, it is recommended to bake out the chamber with surface heaters before depositing after repeated use. There are also additional characterization steps that could have been taken to further analyze the films which would aid in understanding the optical loss mechanisms and results after annealing. $Si_3N_4$ films

deposited by PECVD typically are under tensile stress, which is exacerbated for thicker depositions. Here, 650 nm was deposited which demonstrated high loss in the C-band, for a gas flow recipe which was identical to another 350 nm film which exhibited low-losses. This change could be due to many factors, however characterizing the tensile stress via wafer bowing measurements would reveal the influence of stress when comparing identical film recipes with varying thicknesses. It was also observed that annealing lead to cracking in many films, but not the films which contained the highest Si content. It is therefore recommended to investigate silicon rich $Si_xN_y$ films for stress and the impact this has on surviving subsequent heat treatment. Lastly, the bonding characteristics of hydrogen and the impact this has on optical loss is recommended for future study. Measurements such as FTIR would reveal the dominant bonds, N-H, Si-H, and O-H which contribute to the losses from incorporated hydrogen. Measurements which reveal these characteristics before and after annealing may also reveal information on the silicon rich films and their capabilities for withstanding heat treatment. An understanding of the loss mechanisms will also point towards further ways of optimizing the deposition process and producing higher optical quality non-stoichiometric films.

Overall, the UV writing process with negative photoresist could be improved in terms of repeatability and control of feature sizes. To achieve reliable dimensions using the process, calibration was needed to anticipate the design-to -fabricated feature width when operating near the systems resolution limits. This was due to the UV writing being operated at high powers and relying on the scattering of light within the proximity of the designed feature to form smooth sidewalls for the waveguide mask. In future it would be recommended to discover lower operating exposure power recipes which use multiple

passes to ensure cross-linking of the resist without excessive optical scattering, which results in feature expansion. It is anticipated this would lead to better control of small feature gaps for devices such as ring resonators and couplers. Additionally, there are many material systems which would benefit from the use of UV writing which were not explored in this thesis. The process could be applied to direct writing waveguides in materials such as PMMA, or germanium oxide which can experience a refractive index change after UV exposure. All of these would benefit from fine feature control, and reliable writing recipes.

Optimizing the $Al_2O_3:Er^{3+}:Yb^{3+}$ films for lower optical losses would benefit the overall performance of the amplifiers. Sputtering conditions such as deposition stage temperature, relative $Ar/O_2$ gas flow, target sputtering power, and stage bias could all be adjusted to further optimize the film losses. A stage temperature above 500 °C or subsequent heat treatment of the films were not studied for its overall impact on loss and morphology or dopant sites via TEM. It is recommended to deposit the films at a higher temperature for future study, and investigate the dispersion of rare-earth ions via TEM. Efficient energy transfer between $Er^{3+}$ and $Yb^{3+}$ is critical for amplifier performance and discovering the optimal doping concentrations for efficient pumping and energy conversion is recommended for further study. This would require a variety of dopant ratios and characterization of spectroscopic details such as lifetime, quenching, and conversion efficiencies, followed by subsequent gain measurements. A spectroscopically parameterized amplifier model is also recommended for development in order to properly optimize designs through simulations of the gain. For $Al_2O_3:Er^{3+}:Yb^{3+}$ ridge waveguide amplifiers to demonstrate net fiber-fiber gain, a large barrier for performance remains fiber

to chip coupling. Strategies such as inverse tapering are not as applicable to the ridge geometry, and therefore methods such as hybrid waveguide designs, or vertical coupling approaches to other materials should be investigated for future study with shallow-etched ridge waveguides. The wet etching of films to fabricate waveguides produced smooth surfaces with reliable etch rates, however certain drawbacks exist practically as well as theoretically. Etching was performed with a relatively large volume of $H_3PO_4$ (250 mL) per run of ~4, 3-inch wafers. This was to ensure homogenous concentration and excess reactants for the chemical process. After 4 wafers, etch rates were observed to be not constant, as the additional water and reflux of the acid at 60 °C changes the acid concentration. It is recommended to better assess the volume of acid needed for the wet etch, and to discover or use a calibrated addition of more acid to supply the reaction with in-situ chemical measurements. All of these recommendations would enable lower loss films and waveguides, with more controllable fabrication and the realization of longer devices such as spirals for higher net-gain.

The sensors demonstrated could be optimized by a variety of changes to the design, and materials involved as well as benefitted from additional measurement techniques and biological study. In general, the optimization of Bragg waveguide designs is recommended for future work on Si sensors hybridized with rare-earth compatible oxides coated in biologically functionalized polymers. The grating design was compared for 2 different structures, sidewall and multi-piece, with little variations to aspects such as grating strength and cavity length. Future study is recommended in varying features to both designs to realize the trade-off between grating, oxide, and analyte optical overlap of TE and TM modes. Variations to the multi-piece design are suggested in order to

increase sensitivity by increasing overlap with the sensing medium, as they were shown to outperform the sidewall devices due to high grating overlap. Moving forward it is recommended to dope the PMMA/$TeO_2$:Si during deposition with elements like $Er^{3+}$ and $Tm^{3+}$ to then realize laser-based sensors in DBR and DFB resonators. To do so, it is also recommended for laser stability and chip functionality to be stabilized and secured in a microfluidic setup to avoid degradation of the laser signal through PDMS channels. A fully integrated demonstration is then recommended which implements electrical readout and a PCB mounted chip. Biological sensors also benefit from access to the visible spectrum, which is why $Si_3N_4$ is recommended for further study using the PMMA/$TeO_2$:$Si_3N_4$ sensing platform. Here, pre-defined Bragg grating waveguides are also available from foundry, which could provide a low-loss platform for the post deposition of $TeO_2$ and subsequent coating in functionalized PMMA. Future study should also be directed at $Al_2O_3$ as a hybrid cladding as well as a standalone waveguide sensor with functionalized PMMA. The larger mode areas possible with ridge $Al_2O_3$ waveguides compliments the need for high overlap in the top layer for sensing. In general, the surface and interfacial chemistry and functionalization of PMMA for biological adsorption is a study also worthy of future investigation. Comparisons to known biological measurement techniques are recommended to optimize functionalization strategies and surface treatments. Sensing measurements that involve varying concentrations of proteins in buffer are needed to better characterize the sensors and investigate factors such as up-take and modification steps to the PMMA layer. These investigations and studies should aim towards realizing a monolithically integrated laser sensor capable of protein and single virus detection.